A 3D multiscale synthetic model of biological tissue for virtual imaging

Zexian Wang

N°d'ordre NNT : 2022ISAL0114

THESE de DOCTORAT DE L'INSA LYON,
membre de l'Université de Lyon

Ecole Doctorale N° EDA 162 MEGA
(MÉCANIQUE, ÉNERGÉTIQUE,
GÉNIE CIVIL, ACOUSTIQUE)

Spécialité/ discipline de doctorat :
Acoustique / Traitement du Signal et de l'Image

Soutenue publiquement 12/12/2022, par :
Zexian WANG

A 3D multiscale synthetic model of biological tissue for virtual imaging

---

Devant le jury composé de :

RAMALLI Alessandro	Associate Professor, Université de Florence	Rapporteur
ZULUAGA Maria A.	Maître de Conférence HDR, EURECOM	Rapporteure
KACHENOURA Nadjia	Directrice de Recherche, Sorbonne Université	Examinatrice
MERIAUDEAU Fabrice	Professeur des Universités, Université de Bourgogne	Examinateur
CLARYSSE Patrick	Directeur de Recherche, INSA-Lyon	Examinateur
VARRAY François	Maître de Conférences HDR, Université Lyon 1	Directeur de thèse
MAGNIN Isabelle	Directeur de Recherche, INSERM	Invitée

Département FEDORA – INSA Lyon - Ecoles Doctorales

SIGLE	ECOLE DOCTORALE	NOM ET COORDONNEES DU RESPONSABLE
CHIMIE	**CHIMIE DE LYON** **https://www.edchimie-lyon.fr** Sec. : Renée EL MELHEM Bât. Blaise PASCAL, 3e étage secretariat@edchimie-lyon.fr	**M. Stéphane DANIELE** C2P2-CPE LYON-UMR 5265 Bâtiment F308, BP 2077 43 Boulevard du 11 novembre 1918 69616 Villeurbanne **directeur@edchimie-lyon.fr**
E.E.A.	**ÉLECTRONIQUE, ÉLECTROTECHNIQUE, AUTOMATIQUE** **https://edeea.universite-lyon.fr** Sec. : Stéphanie CAUVIN Bâtiment Direction INSA Lyon Tél : 04.72.43.71.70 secretariat.edeea@insa-lyon.fr	**M. Philippe DELACHARTRE** INSA LYON Laboratoire CREATIS Bâtiment Blaise Pascal, 7 avenue Jean Capelle 69621 Villeurbanne CEDEX Tél : 04.72.43.88.63 **philippe.delachartre@insa-lyon.fr**
E2M2	**ÉVOLUTION, ÉCOSYSTÈME, MICROBIOLOGIE, MODÉLISATION** **http://e2m2.universite-lyon.fr** Sec. : Bénédicte LANZA Bât. Atrium, UCB Lyon 1 Tél : 04.72.44.83.62 secretariat.e2m2@univ-lyon1.fr	**Mme Sandrine CHARLES** Université Claude Bernard Lyon 1 UFR Biosciences Bâtiment Mendel 43, boulevard du 11 Novembre 1918 69622 Villeurbanne CEDEX **sandrine.charles@univ-lyon1.fr**
EDISS	**INTERDISCIPLINAIRE SCIENCES-SANTÉ** **http://ediss.universite-lyon.fr** Sec. : Bénédicte LANZA Bât. Atrium, UCB Lyon 1 Tél : 04.72.44.83.62 secretariat.ediss@univ-lyon1.fr	**Mme Sylvie RICARD-BLUM** Institut de Chimie et Biochimie Moléculaires et Supramoléculaires (ICBMS) - UMR 5246 CNRS - Université Lyon 1 Bâtiment Raulin - 2ème étage Nord 43 Boulevard du 11 novembre 1918 69622 Villeurbanne Cedex Tél : +33(0)4 72 44 82 32 **sylvie.ricard-blum@univ-lyon1.fr**
INFOMATHS	**INFORMATIQUE ET MATHÉMATIQUES** **http://edinfomaths.universite-lyon.fr** Sec. : Renée EL MELHEM Bât. Blaise PASCAL, 3e étage Tél : 04.72.43.80.46 infomaths@univ-lyon1.fr	**M. Hamamache KHEDDOUCI** Université Claude Bernard Lyon 1 Bât. Nautibus 43, Boulevard du 11 novembre 1918 69 622 Villeurbanne Cedex France Tél : 04.72.44.83.69 **hamamache.kheddouci@univ-lyon1.fr**
Matériaux	**MATÉRIAUX DE LYON** **http://ed34.universite-lyon.fr** Sec. : Yann DE ORDENANA Tél : 04.72.18.62.44 yann.de-ordenana@ec-lyon.fr	**M. Stéphane BENAYOUN** Ecole Centrale de Lyon Laboratoire LTDS 36 avenue Guy de Collongue 69134 Ecully CEDEX Tél : 04.72.18.64.37 **stephane.benayoun@ec-lyon.fr**
MEGA	**MÉCANIQUE, ÉNERGÉTIQUE, GÉNIE CIVIL, ACOUSTIQUE** **http://edmega.universite-lyon.fr** Sec. : Stéphanie CAUVIN Tél : 04.72.43.71.70 Bâtiment Direction INSA Lyon mega@insa-lyon.fr	**M. Jocelyn BONJOUR** INSA Lyon Laboratoire CETHIL Bâtiment Sadi-Carnot 9, rue de la Physique 69621 Villeurbanne CEDEX **jocelyn.bonjour@insa-lyon.fr**
ScSo	**ScSo*** **https://edsciencessociales.universite-lyon.fr** Sec. : Mélina FAVETON INSA : J.Y. TOUSSAINT Tél : 04.78.69.77.79 melina.faveton@univ-lyon2.fr	**M. Bruno MILLY** Université Lumière Lyon 2 86 Rue Pasteur 69365 Lyon CEDEX 07 **bruno.milly@univ-lyon2.fr**

*ScSo : Histoire, Géographie, Aménagement, Urbanisme, Archéologie, Science politique, Sociologie, Anthropologie

ACKNOWLEDGEMENT

First and foremost, I would like to express my deepest appreciation to my supervisors, Prof. François VARRAY and Prof. Isabelle MAGNIN, for their precious guidance and advice throughout my PhD. They can always give me the direction of the research with their valuable help and instruction in patience. Their knowledge and insight motivate me all the time to move on in academic research.

Besides, I want to give my sincere gratitude to the defence committee members: Prof. RAMALLI Alessandro, Prof. ZULUAGA Maria, Prof. KACHENOURA Nadjia, Prof. MERIAUDEAU Fabrice and Prof. CLARYSSE Patrick, for their attendance of my defence and their plentiful expertise.

My gratitude extends to the China Scholarship Council for its financial support during my PhD.

I also want to express thanks to the colleagues and staff in CREATIS. Special thanks go to Júlia Puig, Ludmilla Peñarrubia, Charles Jabour, Florian Vixège, Nicolas Loiseau, Nicolas Raoul Pinon, and Théo Leuliet, for their being not only colleagues who work in the same office but also reliable friends, for their French language help and multicultural exchange, and for the unforgettable game and food nights. I also want to thank my Chinese colleagues: Jiqing Huang, Yunyun Sun, Yuhan Jing,

Bingqing Xie, Pei Niu Yunlong He, Ruifen Zhang, Jingfeng Lu, Zinan Liu and Zhiyuan Li, for their help and accompanying during those nostalgic times.

Thanks also should go to my dear friends: Yao Tang, Robert Shearing, Robin Manganiello, Xuejun Zhao, Meng Liang, Rongrong Zhang, Xiaoting Zhang, Chenting Wang and Xiaoci Zhang, for our precious friendship and the joyful time we spent together.

At last but not least, my great thanks go to my beloved parents who gave me unconditional love and support and my grandmother whose philosophy of life I deeply benefit from.

Merci beaucoup d'avoir toujours été avec moi !

- Zexian WANG

Contents

List of Figures

List of Tables

List of Symbols and Abbreviations

Abbreviations

μ-CT	Micro-CT
2D	Two Dimensional
3D	Three Dimensional
CE	Cellular Matrix
CVD	Cardiovascular Diseases
DT-MRI	Diffusion Tensor Magnetic Resonance Imaging
ECM	Extra-Cellular Matrix
ESRF	European Synchrotron Radiation Facility
FDK	Feldkamp-David-Kress
FEM	Finite Element Method
FFD	Free-Form Deformation
IGA	IsoGeometric Analysis
LA	Left Atrium
LV	Left Ventricle
MLE	Maximum Local Error

MM Meshless Method

PLI Polarized Light Imaging

RA Right Atrium

RMSE Root Mean Square Error

ROI Region Of Interest

RTK Reconstruction ToolKit

RV Right Ventricle

SDD Source to Detector Distance

SEM Scanning Electron Microscopy

SID Source to Isocenter Distance

SNR Signal-to-Noise Ratio

SR-PCT Synchrotron Radiation Phase micro-Computed Tomography

SVD Singular Value Decomposition

TEM Transmission Electron Microscopy

US UltraSound

Symbols

$(\vec{S}, \vec{T}, \vec{U})$ Base vectors of local coordinate system

(s, t, u) Local coordinates of a point

$\boldsymbol{D}_{DB}$ The domain of the probability distributions in the calculation of D_B

$\hat{y}$ The mean value of the sample to be evaluated when calculating RMSE

$\mathbf{B}$ Transformation matrix in FFD

$\mathbf{B}^{\dagger}$ Moore-Penrose inverse matrix of $\mathbf{B}$

$\mathbf{D}$ Matrix saving the coordinates of data during FFD

$\mathbf{O_L}$ The origin of the local coordinates system

$\mathbf{P}^*$ The coordinates of displaced control point

$\mathbf{P}$ Matrix saving the coordinates of control points

$\mathbf{U}$ Left orthogonal matrix in SVD

$\mathbf{V}$ Left orthogonal matrix in SVD

$\mathbf{W}$ Singular value matrix in SVD

$\mathbf{X}_*$ Matrix saving the coordinates of virtual volume simulating $\mathbf{X_D}$

$\mathbf{X}$ Matrix saving the coordinates of a volume during FFD

ε_1, ε_2 First and second exponent parameter in superellipsoid

$\vec{d}$ Coordinates of a data point during FFD

a_1, a_2, a_3 Radius of an superellipsoid along the x, y and z axis

$A_{rotation}$ An arbitrary angle varied between two consecutive layers

A_z Rotation degree

D_B Bhattacharyya Distance

$G(\mu,\sigma)$ Gaussian noise with mean value μ and standard deviation σ

L_b, R_b Height and radius of the cylinder for simulating the basic shape of a bundle of cardiomyocytes

L_{mc} Length of the virtual cardiomyocyte

L_{te} Length of the truncated ellipsoid simulating cardiomyocyte bundle

$p(x)$, $q(x)$ The two probability distributions in the calculation of D_B

p_G Probability density function of Gaussian noise

q_x, q_y Weighting coefficient of deformation from cylinder to truncated twisted ellipsoid along x and y direction

R_l, R_s Semi-major and semi-minor axis of an ellipse

R_x, R_y, R_z Radius of the superellipsoid for simulating the objective shape of a bundle of cardiomyocytes along the x, y and z axis

t_x, t_y, t_z Translation distance of a superellipsoid along the x, y and z axis

V_{EX} Extrinsic feature vector of an object

V_{FN} Functional feature vector of an object

V_{IN} Intrinsic feature vector of an object

V_{Object} Feature vector of an object

V_{PH} Physical feature vector of an object

y_i The i^{th} element of the sample to be evaluated when calculating RMSE

Synthèse en Francais

Introduction générale

Compte tenu du contexte actuel des maladies cardiovasculaires, la nécessité d'améliorer le diagnostic de ces maladies est primordiale. Les progrès des techniques d'imagerie sont d'importance cruciale dans le diagnostic clinique. Elles fournissent une meilleure connaissance de la structure 3D du cœur qui peut être utilisée pour construire des modèles cardiaques dans le but d'étudier la relation entre les structures du cœur et leurs fonctionnalités.

Ainsi, l'objectif de ma thèse consiste à construire un modèle déformable multi-échelle 3D pour décrire la structure 3D de base ainsi que la forme géométrique et les caractéristiques des principaux éléments du cœur. Ce modèle sera utilisé pour étudier la structure 3D du cœur et leur interaction, en particulier grâce à la génération de volumes virtuels pour l'imagerie ou d'autres applications fonctionnelles. Le modèle 3D multi-échelle proposé démarrera du niveau global (macro-échelle) jusqu'au niveau tissulaire (micro-échelle) en intégrant divers constituants du cœur. Ainsi, une brève introduction sera proposée pour décrire la structure cardiaque, en particulier la structure des quatre chambres, la structure laminaire du myocarde, l'architecture des fibres et les cardiomyocytes.

Sur la base de cette introduction, le modèle multi-échelle 3D sera détaillé. Dans le chapitre 2, l'élaboration globale du modèle multi-échelle sera introduit avec sa structure de graphe hiérarchique et les relations entre ses éléments. En outre, la méthode de modélisation orientée objet et la propriété voxel de mon modèle multi-échelle seront soulignées. Enfin, la méthode de déformation libre (Free Form Deformation FFD) utilisée

dans mon modèle géométrique au différent niveau du modèle sera également présentée. Dans le chapitre 3, la partie basse résolution du modèle multi-échelle sera illustrée. Elle utilise le modèle super-ellipsoïde comme méthode d'ajustement des données grossières (basse résolution) et la FFD comme méthode d'ajustement au données haute résolution. De même, la déformation et la correspondance des surfaces et des volumes dans le modèle basse résolution est également démontrée. Le chapitre 4 se concentre sur l'aspect haute résolution du modèle multi-échelle. Les premiers objets élémentaires synthétiques seront présentés ainsi que leurs déformations à l'échelle tissulaire, impliquant en particulier les cardiomyocytes (matrice cellulaire), les groupes de cardiomyocytes et les plans de clivage (matrice extracellulaire). Dans le chapitre 5, l'imagerie virtuelle du modèle sera conduite. Pour cela, différentes valeurs réalistes seront extraites de la littérature et de données expérimentales 3D préalablement acquise afin de simuler au mieux les structures laminaires parallèles dans les feuillets lamellaires de cardiomyocytes. Différentes comparaisons seront réalisées entre les volumes initiaux et ceux obtenus par imagerie virtuelle. Enfin, une conclusion et des perspectives terminent ce manuscrit.

Chapitre 1: Structure cardiaque et modélisation

Ce chapitre expose principalement les motivations de cette thèse, notamment le contexte des maladies cardiovasculaires (MCV), l'importance des modalités d'imagerie médicale et la nécessité de construire des modèles cardiaques tridimensionnels (3D). De même, pour enrichir ces développements initiaux, plusieurs sujets connexes sont énoncés, y compris la structure cardiaque, l'état de l'art des modèles cardiaques et les modalités d'imagerie de nos jours.

Le cœur est l'organe principal du système cardiovasculaire et permet la circulation du sang dans tout le corps. C'est aussi un organe très complexe composé de plusieurs éléments évoluant à différentes échelles. Ces structures élémentaires se connectent et s'assemblent anatomiquement pour permettre au cœur de fonctionner normalement. De nombreuses maladies provoquent des remodelages structurels cardiaques, tels que la déformation de la géométrie ventriculaire et le changement d'orientation des fibres. La connaissance anatomique des éléments du cœur est donc capitale. La connaissance anatomique

du muscle cardiaque comprend entre autres, les quatre cavités du cœur, dont les chambres supérieures appelées oreillette gauche (LA) et oreillette droite (RA) et les chambres inférieures appelées ventricule gauche (LV) et ventricule droit (RV), l'épicarde, l'endocarde, sa structure laminaire (feuillets lamellaires de cardiomyocytes et plan de clivage), et l'architecture des fibres (groupe de cardiomyocytes et les cardiomyocytes).

La géométrie cardiaque est une caractéristique essentielle, représentée par divers modèles cardiaques 3D avec précision et réalisme. Les modèles de structure cardiaque ont évolué ces dernières années. Des modèles géométriques 3D de diverses sections du cœur ont été proposés pour des applications diverses mais uniques. De plus, la plupart d'entre eux sont proposés à une échelle spécifique. Les modèles 3D ont d'abord été étudiés à partir d'observations anatomiques pour décrire la structure du cœur. Puis, avec le développement des techniques d'imagerie, des modèles basés sur l'image ont été développés. Des modèles de conception assistée par ordinateur ont également été définis pour construire des modèles cardiaques 3D sans données en entrée. Après une meilleure connaissance de la structure de base, à l'inverse, certains modèles 3D ont également été proposés pour aider à la reconstruction des images 3D du tissu et à la modélisation du mouvement cardiaque 3D. De même, pour prendre en compte les recherches conjointes sur la structure et le mouvement du cœur, des modèles fonctionnels ont été proposés pour comprendre le rôle de chaque partie du cœur. Enfin, avec l'émergence des technologies d'imagerie cardiaque in vivo et la demande croissante de traitements médicaux personnalisés, certains modèles 3D sont mis en œuvre dans les domaines de la médecine personnalisée et en routines cliniques.

La structure du cœur est complexe et composée d'une série d'objets élémentaires fonctionnant conjointement à travers les différentes échelles. L'intégration des données à travers les échelles spatiales et fonctionnelles fait l'objet d'efforts de recherche importants, car la simulation d'un cœur totalement fonctionnel est l'un des problèmes les plus difficiles à résoudre. A une échelle donnée, le myocarde peut être étudié du niveau moléculaire au niveau du corps entier, que le myocarde soit sain ou malade. La modélisation multi-échelle convient bien aux tissus biologiques car le but final est de générer un modèle avec des objets évoluant à différents niveaux tout en décrivant comment ils sont disposés et fonctionnent ensemble. Initialement, divers modèles multi-échelles ont

été proposés pour étudier les relations structurelles dans le cœur. Outre les objectifs structurels, certaines recherches ont également porté sur les parties fonctionnelles telles que l'électrophysiologie cardiaque, l'hémodynamique et la fonction mécanique du cœur. Ensuite, ces modèles se concentrent également sur la clinique.

Le cœur est un organe cinétique élastique dont les formes de ses éléments constitutifs sont toutes irrégulières. Ainsi, les modèles déformables sont généralement appliqués au suivi du mouvement cardiaque, au recalage des images cardiaques et à la segmentation des images cardiaques. Les modèles déformables sont utilisés pour décrire les limites d'une région avec des courbes ou des surfaces paramétriques fermées, qui se déforment sous l'effet de forces internes et externes.

La modélisation 3D du tissu cardiaque est influencée dans une large mesure par la qualité des techniques d'imagerie, car la plupart des informations anatomiques sont évaluées à partir de l'observation ou du calcul sur des images médicales. Les données d'images médicales ont été les moteurs de la modélisation informatique cardiaque car elles peuvent capturer des informations anatomiques pour effectuer des simulations, elles peuvent fournir des informations fonctionnelles utilisées pour construire, ajuster et valider des modèles ou encore être utilisées pour estimer les paramètres des modèles. Bien que plusieurs modalités d'imagerie à haute résolution puissent aider à comprendre l'anatomie du tissu cardiaque, la modélisation cardiaque est également limitée par leurs résolutions. La microscopie électronique à transmission (MET) offre une haute résolution de $0,2$ nm tandis que la microscopie électronique à balayage (MEB) est autour de 50 nm. Cependant, la taille de leur échantillon est limitée au environ de 60 μm. La microscopie confocale offre une résolution de reconstruction élevée de $0,4$ μm mais est aussi limitée par la taille du volume de 35 μm. Outre la limitation en taille de l'échantillon, la plupart des études sont souvent limitées par l'anisotropie et/ou la faible résolution des données, ce qui les empêche de fournir des détails sur la structure. L'imagerie par tenseur de diffusion (difussion magnetic ressonance imaging dMRI) fournit l'arrangements des cardiomyocytes à une résolution de $1,3 \times 1,3 \times 1,3$ mm^3. En utilisant l'imagerie par lumière polarisée (PLI), la résolution peut être améliorée à $90 \times 90 \times 500$ μm^3 en raison de la biréfringence positive uniaxiale cristalline de la myosine. La dernière, l'IRM à haute résolution, fournit une résolution encore plus fine de $50 \times 50 \times 50$ μm^3. Au cours de la

dernière décennie, une technique d'imagerie Micro-CT (μ-CT) a été développée et a fournit une analyse des fibres dans la section des oreillettes des cœurs de chiens avec une haute résolution de $36 \times 36 \times 36$ μm^3.

Les travaux récents de notre groupe ont permis d'obtenir des données de 3D par rayons X à contraste de phase (μ-CT) à une résolution spatiale isotrope de $3,5 \times 3,5 \times 3,5$ μm^3. Cette résolution amène des connaissances quantitatives sur l'arrangement 3D de la matrice cellulaire et de la matrice extracellulaire dans des échantillons de cœur humain post-mortem. Les échantillons de cœur ont été imagés à l'aide du rayonnement synchrotron dans le cadre de l'imagerie synchrotron par tomographie à contraste de phase (SR-PCT) à l'European Synchrotron Radiation Facility (ESRF) qui est un accélérateur de particules situé à Grenoble, France. 2499 projections ont été obtenues sur chaque échantillon et des algorithmes spécifiques de reconstruction utilisant la phase sont utilisées pour reconstruire le volume 3D final.

Chapitre 2: Modèle déformable multi-échelle

Le cœur est un organe complexe composé de plusieurs éléments à différentes échelles. Ces éléments qui se connectent et se rejoignent anatomiquement permettent au cœur de fonctionner normalement. Il est donc essentiel de concentrer les études sur plusieurs éléments et échelles lors de la recherche sur la structure et les fonctions du cœur, comme la connectivité entre les différents éléments ou la façon dont le cœur se remodèle au cours du cycle cardiaque. Par conséquent, un modèle de cœur multi-échelle composé d'éléments à différentes échelles est nécessaire et d'intérêt pour la recherche sur le cœur.

En ce qui concerne la structure de base du cœur, j'ai proposé un modèle multi-échelle contenant les principales structures anatomiques élémentaires du cœur à cinq niveaux différents, allant de la macro- (cm) à la micro-échelle (μm). Il comprend les cavités (ventricules, oreillettes), la matrice cellulaire (feuillet lamellaires de cardiomyocytes, groupes de cardiomyocytes et cardiomyocytes individuels) et la matrice extracellulaire (plans de clivage, endocarde, épicarde et périmysium).

Ce chapitre présente la structure et les propriétés du modèle déformable multi-échelle proposé. Il s'agit d'un modèle hiérarchique, basé sur les voxels et orienté objet. De même,

la technique de déformation est également introduite dans le modèle.

L'ensemble du modèle est divisé en cinq niveaux. À chaque niveau d'échelle, il existe plusieurs structures élémentaires. Chaque élément du cœur est considéré comme un objet. La structure topologique du modèle est présentée dans la Fig. 2.1 ainsi que la relation entre ces objets et les niveaux. Dans cette structure, les objets sont comme les nœuds d'un réseau qui peuvent être connectés (même échelle) ou imbriqués les uns dans les autres (plus grande échelle). Chacun d'eux est composé d'un modèle géométrique (forme imitant l'anatomie) auquel est attaché un vecteur de caractéristiques pour stocker ses paramètres. Des volumes 3D peuvent être générés selon le modèle géométrique tandis que chaque voxel à l'intérieur reçoit une étiquette de l'objet auquel il appartient.

Les approches orientées objet sont mises en œuvre sur notre modèle multi-échelle en raison de leur capacité à représenter des objets connectés ou reliés sous une forme compacte et cohérente. Elle permet une décomposition hiérarchique du cœur par héritage dans la programmation, ce qui est la base d'une réutilisation efficace et correcte des caractéristiques de chaque niveau. Avec cette méthode, chaque objet possède sa classe de propriétés qui est codée séparément, mais à travers différents niveaux, les classes sont mutuellement liées et ont une relation d'héritage. Une classe stocke les informations et l'état d'un objet puis diverses procédures sont exploitées soit sur l'objet et soit peut en générer un nouveau.

Les voxels sont utilisés comme unités de base dans notre modèle. En effet, les modèles basés sur les voxels sont bien adaptés pour représenter les structures complexes de l'anatomie humaine car ils sont conçus à partir de l'anatomie réelle. De plus, ils sont flexibles et peuvent être mis à l'échelle pour correspondre à toute dimension ou déformation requise.

Le premier objectif de notre modèle est de décrire la forme géométrique constituant les objets du cœur. Cependant, le cœur est un organe élastique fonctionnel, où la déformation et les réarrangements subtils du tissu se produisent constamment durant les cycles cardiaques. Ainsi, les déformations doivent être prises en compte dans nos modèles géométriques pour chaque objet élémentaire. Parmi les différentes approches possibles, la technique de la déformation libre (FFD) a été choisie. La FFD est introduite à chaque niveau du modèle.

Chapitre 3: Modèle basse résolution

Comme notre modèle va du niveau macro- à microscopique, je divise l'ensemble du modèle en deux parties : (i) le modèle basse résolution, $L1$, qui est à une résolution d'environ 1000 µm, et (ii) le modèle haute résolution, $L2$ à $L4$, avec des résolutions de 100 µm. Dans ce chapitre, je présente comment construire le modèle basse résolution en me concentrant sur l'épicarde et l'endocarde du ventricule gauche. Pour des raisons de compatibilité avec la résolution de $L1$, j'utilise les données cardiaques PLI dont la résolution est de $90 \times 90 \times 500$ µm^3 comme données d'entrée afin de simuler les formes géométriques des deux objets : épicarde partiel et l'endocarde du ventricule gauche (VG). Anatomiquement, l'épicarde est la couche protectrice la plus externe du cœur et l'endocarde est la couche la plus interne tapissant les cavités cardiaques Ainsi, cela signifie que pendant le cycle cardiaque, ils sont tous deux remodelés. Un modèle de surface avec des propriétés de déformation est alors nécessaire lors de la construction de cette forme géométrique. J'ai adapté la méthode proposée dans [Bardinet et al., 1998] pour construire un modèle de surface déformable afin de simuler les formes de l'épicarde partiel et de l'endocarde du VG.

Le modèle de superquadrique est l'un des modèles déformables paramétriques ayant la capacité de représenter des formes proches du cœur avec un petit nombre de paramètres. Parmi tous les modèles de superquadriques, le superellipsoïde est utilisé comme forme initiale car c'est la seule qui définit une surface fermée. Cependant, le modèle superellipsoïde est hautement symétrique, ce qui est insuffisant pour imiter les formes complexes de l'épicarde et de l'endocarde du ventricule gauche. Ainsi, après un ajustement grossier sur la surface cible, la déformation par FFD est effectuée pour affiner le modèle sur les données d'entrée. Par conséquent, en combinant les 8 paramètres du superellipsoïde p_8 et un ensemble de points de contrôle $\mathbf{P}^*$, la forme finale basée sur le modèle basse résolution est décrite.

L'imagerie par lumière polarisée (PLI) est une technique de rehaussement du contraste qui améliore la qualité de l'image obtenue avec des matériaux biréfringents. Comme la résolution des données PLI est proche de celle du modèle à basse résolution proposé et qu'elles contiennent les informations d'orientation des tissus, les données PLI sont adop-

tées comme source de données dans les simulations du modèle à basse résolution.

À l'aide du modèle de surface à faible résolution, des simulations d'un épicarde partiel et de l'endocarde du VG sont effectuées à l'aide des données PLI. Entre l'épicarde, la couche la plus externe, et l'endocarde, la couche la plus interne, le modèle volumique à faible résolution a été construit, et le myocarde ventriculaire virtuel a été généré. Les résultats montrent que le modèle basse résolution a la capacité de simuler raisonnablement les structures choisie (l'épicarde partiel et l'endocarde) avec des erreurs acceptables.

Grâce à la FFD, la déformation bidirectionnelle des formes géométriques des données et du volume du modèle peut être opérée. De plus, en utilisant la procédure inverse, du recalage de volume est effectué, en transférant les informations des données réelles dans un volume modèle d'entrée fixe qui décrit qualitativement les données. Ce recalage entre le volume des angles d'azimut et d'élévation dans les données PLI vers le volume modèle a été effectué. Cependant, ce recalage direct entre les volumes génère des formes en escalier dans certaines zones du modèle et c'est pourquoi une méthode couche par couche est utilisée pour réaliser l'appariement. Les résultats montrent que le modèle cible peut être enrichis par les informations sur les angles d'azimut et d'élévation à partir des données PLI. Par conséquent, les comparaisons des informations myocardiques de différents individus pourraient être effectuées sur ce volume cible.

Chapitre 4: Modèle haute résolution

Après avoir construit le modèle basse résolution L1, le modèle géométrique haute résolution est proposé pour les objets élémentaires aux niveaux L2, L3 et L4. La relation entre les différents objets élémentaires du cœur dépend de la structure multi-échelle, comme le montre la Fig. fig: modelstructure. Parallèlement, les formes et les tailles des objets sont inspirées par l'observation des données du tissu cardiaque humain. Dans mon modèle de tissu cardiaque multi-échelle, le cardiomyocyte est considéré comme l'objet fonctionnel de base. La forme de chaque cardiomyocyte est représentée par un cylindre. Grâce aux études histologiques et à l'observation des données synchrotron, nous savons que, dans le myocarde, plusieurs cardiomyocytes sont organisés en un "groupe de cardiomyocytes" contenant un nombre limité de cardiomyocytes avec une couche de périmysium

qui le contraint et un capillaire au centre. Je définis le "groupe de cardiomyocytes" comme un objet géométrique contenant une série limitée de cardiomyocytes alors que sa forme générale est aussi proche de celle d'un cylindre. Par la suite, je définie la notion de feuillet lamellaires de cardiomyocytes qui correspond à un arrangement de plusieurs plans de clivage et des groupes de cardiomyocytes entre ces plans.

Dans ce chapitre, les formes géométriques de base sont simulées dans le module cardiomyocyte, le module groupe de cardiomyocytes et le module feuillet lamellaires de cardiomyocytes. Dans le module du groupes de cardiomyocytes et pour plus de réalisme, la forme de base est déformée à l'aide de la FFD pour simuler des structures ayant subis des torsions. De même, il est possible de faire subir une variation de forme pour simuler l'effet du cycle cardiaque. Dans le module des feuillets lamellaires de cardiomyocytes, la forme de base est également déformée pour simuler des structures incurvées, plus proche des formes observées sur les images synchrotrons.

La simulation a commencé par l'unité fonctionnelle de base du cœur, le module cardiomyocyte, au niveau L4. Un module cardiomyocyte est composé d'un cardiomyocyte, d'un endomysium qui l'entoure et d'un disque intercalaire reliant les cardiomyocytes bout à bout selon leur direction la plus longue. Selon les observations histologiques, la forme du cardiomyocyte est simulée comme un long cylindre avec une section d'ellipse, tandis que la forme de l'endomysium est simulée comme la surface latérale du cylindre et la forme du disque intercalaire est simulée comme sa surface inférieure. À l'intérieur d'un module cardiomyocyte, chaque partie peut être traitée séparément et combinée ensuite pour composer une unité fonctionnelle complète de base.

Un module de groupe de cardiomyocytes a ensuite été construit. Il comprenant six cardiomyocytes, un capillaire et une couche de périmysium autour d'eux. La forme de l'ensemble du module est également simulée comme un cylindre, le capillaire étant un petit cylindre au centre avec les cardiomyocytes autour. La simulation nécessite de concevoir la disposition compacte du capillaire et des six cardiomyocytes dans la section du groupe de cardiomyocytes, étape réalisée grâce à la ligne de partage des eaux. Après avoir construit la forme de base du module du groupe de cardiomyocytes, j'utilise la FFD pour affiner la forme d'un cylindre à un ellipsoïde tronqué, bruité et tordu pour simuler une forme plus réaliste des tissus biologiques. Pour simuler les différents états du cy-

cle cardiaque, j'ai généré des séquences dynamiques d'un groupe de cardiomyocytes. Inspiré de [Ferreira et al., 2015] et [Wojciech et al., 2016], une courbe de variation de l'épaisseur du myocarde, du rayon, de la longueur et du volume sont définis puis les objets sont générés. Ce type de simulations d'un groupe de cardiomyocytes sont exploitées pour montrer une variation qualitative de la forme à neuf états du cycle cardiaque.

Ensuite, un module de feuillet lamellaires de cardiomyocytes est construit pour simuler la structure laminaire du tissu cardiaque. Le module de feuillet lamellaires de cardiomyocytes est composé de trois plans de clivage parallèles et de deux groupes de cardiomyocytes entre eux. Les groupes de cardiomyocytes entre la même paire de plans de clivage ont une orientation unique tandis qu'elle peut changer entre les plans de clivage. De façon similaire et pour plus de réalisme, la FFD permet de déformer la forme du module de feuillet lamellaires de cardiomyocytes en une forme incurvée. Pour montrer l'intérêt de l'approche multi-échelle, plusieurs cardiomyocytes ont été généré à l'intérieur de chaque groupe de cardiomyocytes. Les feuillets lamellaires de cardiomyocytes virtuels dynamiques ont également été générés en fonction de la courbe de variation de l'épaisseur du myocarde.

Les simulations des formes valident que notre modèle haute résolution peut générer des données virtuelles aux niveaux L2, L3 et L4. De même, en utilisant la FFD, les données virtuelles peuvent simuler le tissu réel et les différents états pendant le cycle cardiaque.

Chapitre 5: Simulation d'imagerie virtuelle à partir de données réelles

Après avoir construit les modèles basse et haute résolution, il a été validé que notre modèle multi-échelle avait la capacité de générer des formes virtuelles de base des objets du cœur à différentes échelles. Il est donc nécessaire de s'appuyer sur des données réelles et d'utiliser leurs informations pour générer des volumes virtuels.

Les données synchrotron obtenues à l'ESRF ont été utilisées comme données réelles dans ce chapitre en raison de leur résolution de reconstruction élevée par rapport aux autres modalités d'imagerie courantes. Deux ensembles de données synchrotron sont

présentés pour illustrer les structures laminaires parallèles et ramifiées des différentes portions du tissu myocardique. Des évaluations des données synchrotron avec la structure de type parallèle ont été effectuées pour obtenir les paramètres géométriques, y compris l'épaisseur des plans de clivage, la distance entre les plans de clivage, ainsi que les orientations des plans de clivage et des groupes de cardiomyocytes. Des simulations ont été effectuées pour générer des volumes virtuels 3D avec des structures parallèles et ramifiées, basées sur les données obtenues à l'ESRF. Un volume virtuel idéal avec une structure parallèle a été généré selon les évaluations des données réelles du synchrotron 1. Un autre volume virtuel a été généré pour simuler quantitativement la structure laminaire ramifiée.

Pour évaluer les volumes virtuels générés, une simulation d'imagerie virtuelle par rayons X est mise en œuvre sur les volumes virtuels générés avec une structure de type parallèle. Nous présentons brièvement le Reconstruction ToolKit (RTK) pour l'imagerie virtuelle par rayon X, puis la géométrie de projection de notre simulation. Grâce à des comparaisons visuelles des résultats, il est validé que, après l'imagerie virtuelle, la structure générale et les écarts entre les tissus demeurent. Pour obtenir une évaluation plus rigoureuse, l'imagerie virtuelle a été réalisée sous diverses niveaux de bruits. Des évaluations quantitatives ont été effectuées sur les volumes virtuels et les volumes reconstruits à partir de ceux-ci. Les résultats ont montré que les effets de la reconstruction diminuaient avec l'augmentation du niveau de bruit, ce qui était conforme aux attentes.

La simulation d'imagerie ultrasonore est également mise en œuvre à l'aide du logiciel FieldII. Les résultats sont également évalués en calculant les orientations des tissus à l'intérieur pour une validation plus robuste du modèle.

Tous les résultats de ce chapitre ont permis de valider le fait que les volumes virtuels générés par le modèle proposé étaient proches visuellement plus que quantitativement.

Conclusion générale

L'objectif de cette thèse est de construire un modèle déformable multi-échelle en 3D pour générer un cœur virtuel synthétique pouvant être utilisé dans la recherche et l'imagerie virtuelle.

Le modèle a été proposé avec cinq niveaux et une structure hiérarchique à chaque échelle, de la macro- à la micro-échelle. Le modèle proposé comporte deux parties : le modèle à basse résolution et le modèle à haute résolution. Il s'agit d'un modèle basé sur les voxels parce que les voxels sont les unités de base de notre modèle et que le modèle basé sur les voxels est plus flexible en termes de taille et de déformation. Il possède une description orientée objet, conçue pour décrire chaque objet à différentes échelles ainsi que les liens aux autres niveaux. Pour chaque objet du modèle, un modèle géométrique a été construit pour décrire la forme en observant les images de tissus réalistes, tandis qu'un vecteur de caractéristiques est conçu pour enregistrer les paramètres de description des caractéristiques de l'objet. J'ai introduit la technique FFD et la procédure de déformation de chaque objet pour améliorer la similarité entre le modèle et le tissu réaliste, ainsi que pour pouvoir imiter la déformation du cœur le long d'un cycle cardiaque.

Dans le modèle à basse résolution, sur la base des données PLI, des modèles de surface de l'épicarde et de l'endocarde ont été construits en utilisant le superellipsoïde comme ajustement grossier des données et la FFD comme ajustement fin des données. Les résultats ont montré que le modèle à basse résolution est capable de simuler raisonnablement les surfaces, l'épicarde partiel, l'endocarde du VG, le volume, et le myocarde ventriculaire au niveau L1, avec des erreurs acceptables. Grâce à la procédure inverse de FFD, des recalages de volumes sont possibles, en transférant les informations des données réelles vers un volume modèle prédéfini qui décrit qualitativement les données. Les résultats montrent que le modèle de référence peut décrire quantitativement les informations d'angle d'azimut et d'élévation des données PLI. Par conséquent, les comparaisons des informations myocardiques de divers individus peuvent être réalisées sur ce volume uniforme.

Dans le modèle haute résolution, sur la base des données synchrotron, le module virtuel de cardiomyocyte au niveau L4, le module virtuel de groupe de cardiomyocytes au niveau L3 et le module virtuel de feuillet lamellaires de cardiomyocytes au niveau L2 ont été générés. La formes de ces objets de base générés par notre modèle et les formes après FFD a été démontrées. Ainsi, le FFD est encore adapté à notre modèle multi-échelle afin de le rendre plus réaliste. Inspirées par certaines références au cycle cardiaque, des séquences dynamiques d'un groupe de cardiomyocytes et de feuillet lamellaires de car-

diomyocytes ont été générées pour simuler qualitativement le changement de forme au cours du cycle cardiaque.

Selon les données synchrotron, les volumes virtuels avec des structures laminaires parallèles et ramifiées ont été générés en utilisant la FFD, ce qui montre la capacité du modèle proposé à générer des structures de forme spécifique dans le cœur. Enfin, l'imagerie virtuelle CT et US sur les volumes de type parallèle générés par notre modèle a été réalisée sous différents niveaux de bruit et les résultats ont été évalués visuellement et quantitativement. Les tendances de ces évaluations étaient conformes à nos attentes, ce qui confirme que les volumes générés par notre modèle ont un effet similaire à celui du tissu réaliste pendant l'imagerie.

À l'avenir, des efforts supplémentaires seront consacrés à des simulations plus précises du tissu, à la simulation du tissu dynamique pendant le cycle cardiaque, ou encore à de nouvelles modalités d'imagerie (dMRI, optique…). De plus, une réflexion sera à menée pour enrichir le modèle de considération fonctionnelles.

General Introduction

Cardiovascular diseases (CVD) remain the leading cause of death and disability in developed countries and a fast-developing issue in low- and middle-income countries [Mendis et al., 2011]. Advanced and innovative cardiac imaging techniques are capable of revealing both the structural and functional information of the heart to enhance clinical diagnosis accuracy. Furthermore, a better knowledge of the three-dimensional (3D) arrangement of the structures present in the heart could help to understand the function of the heart and research on the CVDs [Torrent-Guasp et al., 2005]. Therefore, developing 3D models of the heart using anatomical knowledge can be a way to contribute to the research on the heart.

The heart being a complex, dynamic and deformable functional system, it is valuable and necessary to build a multiscale heart model with the ability to describe the structure of the heart and the relationship among different elements at various scales.

On the basis of the background mentioned above and the advantages of the image-based models, this thesis proposed a 3D multiscale deformable model in my thesis. The model describes the basic 3D structure along with the geometric shape and features of major elements of the heart, crossing the scales from the global level (macro-scale) to the tissue level (micro-scale). The model can be utilised to investigate the 3D structure of the heart and its elements, generate synthetic volumes for virtual imaging and achieve other functional applications such as cardiac remodelling or water diffusion inside the cardiomyocytes, etc. In this thesis, the structure of the multiscale model and the way to build it is illustrated as well as the validation of it using the virtual imaging technique.

The thesis is organised as follows. In chapter 1, a brief introduction to the cardiac structure is given, as well as the structure and function of each elementary part, in order

to help to understand the relationships among them. Then, the development of 3D cardiac models, multiscale models and deformable models are elaborated. At the end of this chapter, imaging modalities contributing to cardiac modelling are depicted.

In Chapter 2, the multiscale deformable model is proposed. The overall elaboration of the proposed multiscale model is given with its hierarchical graph structure of 5 levels and the relationships between its elements. Besides, the objected-oriented modelling method and voxel-based property of the multiscale model are introduced. The deformation technology, Free-Form Deformation (FFD), used in my geometric model at each scale is also introduced.

In Chapter 3, the low-resolution part of the multiscale model at Level 1 is illustrated. Polarized Light Imaging (PLI) data is utilized as the data source. The low-resolution uses the superellipsoid model as the coarse data-fitting method and FFD as the fine data-fitting method. Surface and volume data fitting in the low-resolution model is also demonstrated as well as the volume registration.

In Chapter 4, the high-resolution part of the multiscale model at Levels 2, 3 and 4 is illustrated. The first synthetic elementary objects and their deformation at the tissue scale are given involving cardiomyocytes (cellular matrix), the cardiomyocyte bundles and cleavage planes (extracellular matrix). The dynamic simulations of sheetlets and cleavage planes are presented based on a qualitative curve of the myocardium thickness and some simple assumptions.

In Chapter 5, real 3D synchrotron data with parallel-like and branching laminar structures are presented. Then, morphological features are extracted from the synchrotron data with parallel-like structures which are used to generate virtual volumes with laminar structures. After that, synthetic X-ray projections of this simple virtual tissue model are computed and comparisons between the reconstructed virtual volume and experimental data are displayed. Virtual ultrasound imaging is also operated.

At last, a conclusion and perspectives end this PhD manuscript.

Chapter 1

Cardiac structure and modelling

Contents

1.1 Introduction

Cardiovascular diseases (CVD) deprive annually the lives of over 17 million people all over the world, which accounts for one-third of people's death toll and almost half of the people's death toll related to non-communicable diseases [Mendis et al., 2011]. CVDs have a wide range of kinds, and most of them do not have symptoms in the early stage. Thus, early detection and diagnosis can be beneficial. Nevertheless, there is no unified technique which can diagnose all the diseases [Ebrahimi Nejad et al., 2017].

Advanced and innovative cardiac imaging techniques play significant roles in the diagnosis of CVDs due to their ability to enhance clinical diagnosis accuracy. Moreover, structure and function are inalienable in both healthy and diseased organs [Torrent-Guasp et al., 2005]. These medical imaging modalities are capable of revealing both the structural and functional information of the heart. Furthermore, a better knowledge of the three-dimensional (3D) arrangement of the structures present in the heart could help to understand the function of the heart and to research the CVDs [Torrent-Guasp et al., 2005].

Thus, developing 3D models of the heart using anatomical knowledge can be a way to contribute to the understanding of the relationships between the mechanical and hemodynamical functions as well as the structural changes due to normal and pathological cardiac remodelling. Meanwhile, the resolutions of medical images are compatible with most of the scales relevant to cardiac modelling, which makes medical imaging and modelling increasingly linked [Lamata et al., 2014].

In this chapter, a brief introduction to the cardiac structures is given, as well as the structure and function of each elementary part.

1.2 Cardiac structure

The heart is the main organ of one's cardiovascular system that pumps blood throughout the whole body. It is also a highly complex organ composed of several elements at various scales. These elements, anatomically connected and joined together, enable the heart to work normally. There are many diseases that cause structural cardiac remodelling,

such as ventricular geometry deformation and fibre orientation change, so anatomical knowledge of the heart's elements is of vital importance [Goblot et al., 2016]. In this section, the cardiac structure will be introduced from the macro-scale to the micro-scale, starting from the four chambers to the laminar structure of the myocardium, then the fibre architecture, and at last the basic functional unit, the cardiomyocyte.

1.2.1 Four chambers

The heart has four chambers. The upper chambers are called the left atrium (LA) and right atrium (RA), and the lower chambers are called the left ventricle (LV) and right ventricle (RV). A schematic diagram of four chambers is presented in Fig. 1.1.

1.2.1.1 Atria

The atria are the two upper chambers in the heart separated by the septum. They receive blood from outside the heart. The LA receives the oxygen-rich blood from the lungs and pumps it into the LV. The RA receives deoxygenated blood from the veins throughout the body and pumps it over to the RV. The atria are connected via multiple interatrial bridges embedded in the septum. Both sides of the septum are covered with conductive myocardium [Dössel et al., 2012]. The free portion of the RA appendage is usually triangular, while the LA appendage is generally tubular [Ho et al., 2002].

1.2.1.2 Ventricles

The ventricles are the two lower chambers, bigger than the atria. They expel blood received from the atria. The LV receives blood from the LA and pumps it to the aorta. The RV receives blood from the RA and pumps it to the main pulmonary artery. The shape of the LV can roughly be approximated to a cone with the RV hugging it [Ho, 2009]. The ventricular walls are more muscled than the atria, especially the LV one, because blood is pumped out of the ventricles at greater pressure compared to the atria [Anderson et al., 2004,Peate, 2021]. In recent years, the LV has received a strong focus due to its importance for the general pumping performance of the heart [Lorenz and von Berg, 2006].

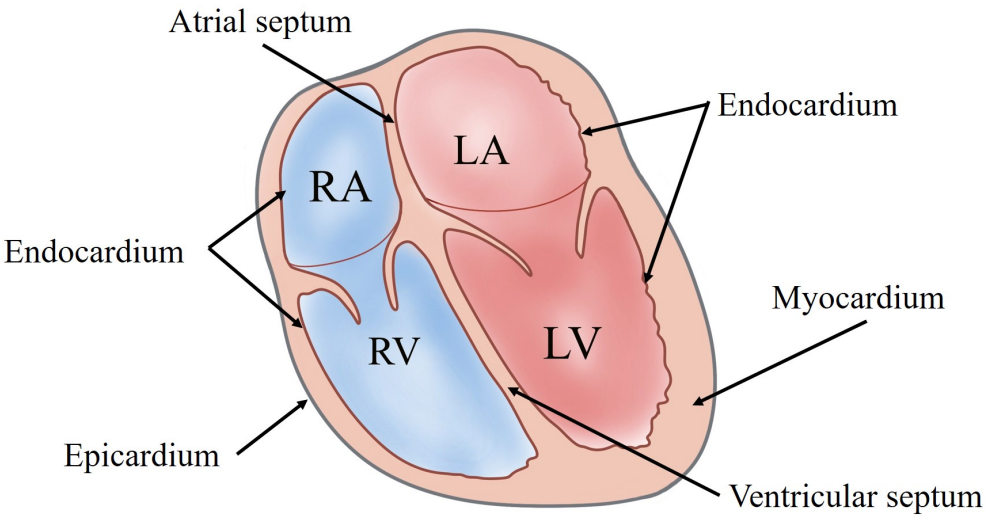

Figure 1.1: *Schematic diagram of four chambers with epicardium and endocardium.*

1.2.1.3 Endocardium

The endocardium is the innermost lining of the heart, which exists in all four chambers. It is of vital importance in heart development, such as the formation of trabecular myocardium [Brutsaert, 1989]. The atrial endocardium is smoother than the ventricular one because the ventricular endocardium is more complex due to the existence of papillary muscles, which play important roles in the functioning of the valves [Vedula et al., 2016, Rich and Khan, 2021]. The LV endocardium is highly corrugated, with surface protrusions extending into the LV cavity [Vedula et al., 2016]

1.2.1.4 Epicardium

The epicardium is the outermost protective layer of the heart surrounding the two atria and two ventricles, the roots of the coronary vessels and connecting the myocardium [Männer et al., 2001]. The epicardium exhibits extensive developmental plasticity and plays a vital role in wall-thickening and wall-motion [Lorenz and von Berg, 2006, Simões and Riley, 2018].

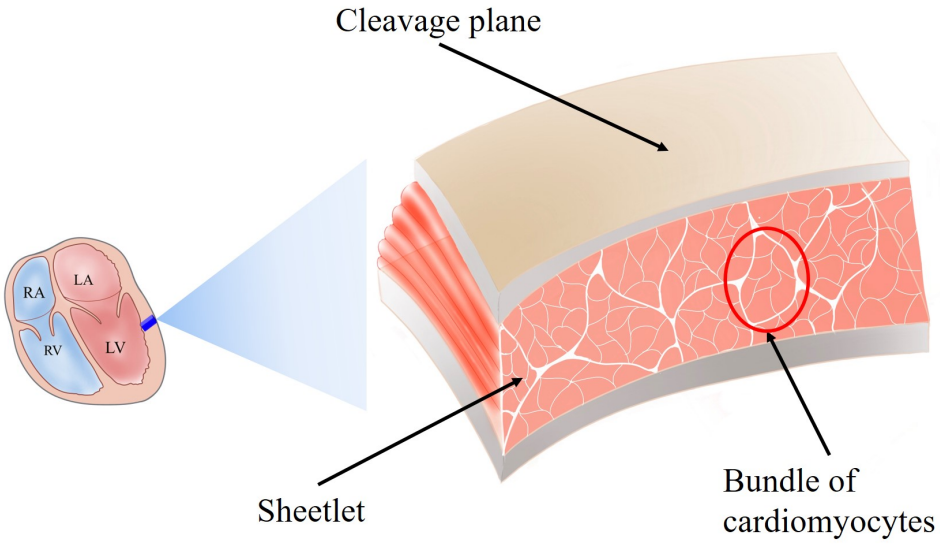

Figure 1.2: *Schematic diagram of the laminar structure in the myocardium.*

1.2.2 Laminar structure of the myocardium

1.2.2.1 Sheetlet

The 3D arrangement of the ventricular muscle cells, the associated extracellular matrix (ECM) and the laminar structures are complex [Hort, 1957a]. Laminar sheets are groups of cells organized in layers, which are surrounded by the perimysium ECM and have a three to four-cell thickness [LeGrice et al., 1995b, LeGrice et al., 2005, Pope et al., 2008], as shown in Fig. 1.2. Mathematical models have been proposed to describe the organisation of the myocardium, in which there are ordered laminar structures, separated by ECM, running radially from the endocardium to the epicardium [LeGrice et al., 2001, Mirea, 2017]. Reorientation of the sheetlet during LV thickening has been proposed as the predominantly associated mechanism [Nielles-Vallespin et al., 2017].

1.2.2.2 Cleavage plane

Cleavage planes are terms used to describe the perimysium ECM. Cleavage planes separate the sheetlets and provide looser connections and potential spaces for relative slippage between adjacent sheetlets [Wang et al., 2019].

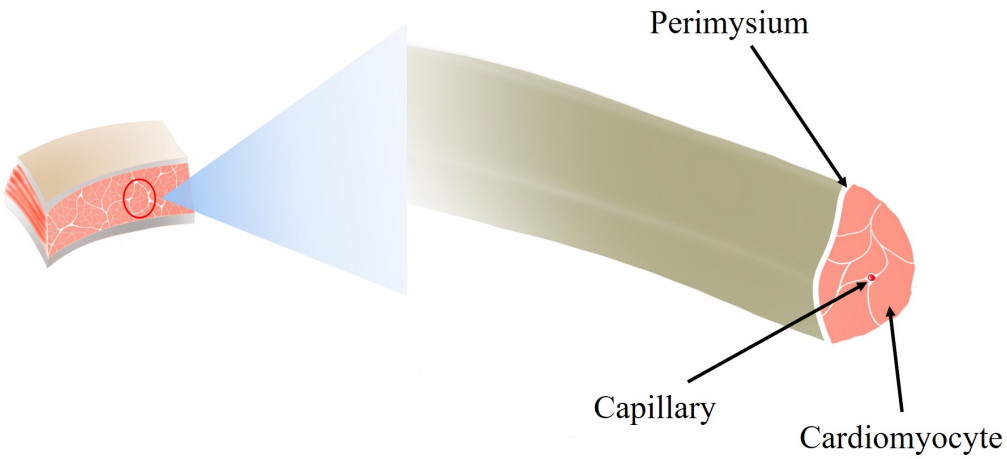

Figure 1.3: *Schematic diagram of a cardiomyocyte bundle.*

1.2.3 Fibre architecture

Similar to skeletal muscles, the myocardium has a fibre architecture [Fernandez-Teran and Hurle, 1982]. The fibre orientation predominantly determines the electrical activation pattern of the myocardium because the electrical signal propagates faster in the longitudinal axis than in the thorganisedrsal one. Meanwhile, the myocardial contraction is characterised by shrinkages of cardiomyocytes along the longitudinal axis [Lopez-Perez et al., 2015].

In previous research, the terminology of the fibre architectures in the heart is complex, and the definitions of terms, such as the term *myofibre* or *fibre*, are confusing [Streeter Jr, 2005, Anderson et al., 2005, Fernandez-Teran and Hurle, 1982, Gilbert et al., 2007]. Thus, in my thesis, I avoid using these terms but use the term *cardiomyocyte bundles* instead to describe the fibre architecture.

1.2.3.1 Cardiomyocyte bundle

Cardiomyocytes are elongated, aligned, and grouped into bundles around capillaries, which is called *cardiomyocyte bundles* in my thesis [Xiao et al., 2014], as shown in Fig. 1.3. Cardiomyocyte bundles are embedded in the sheetlets or appear alone inside the myocardium.

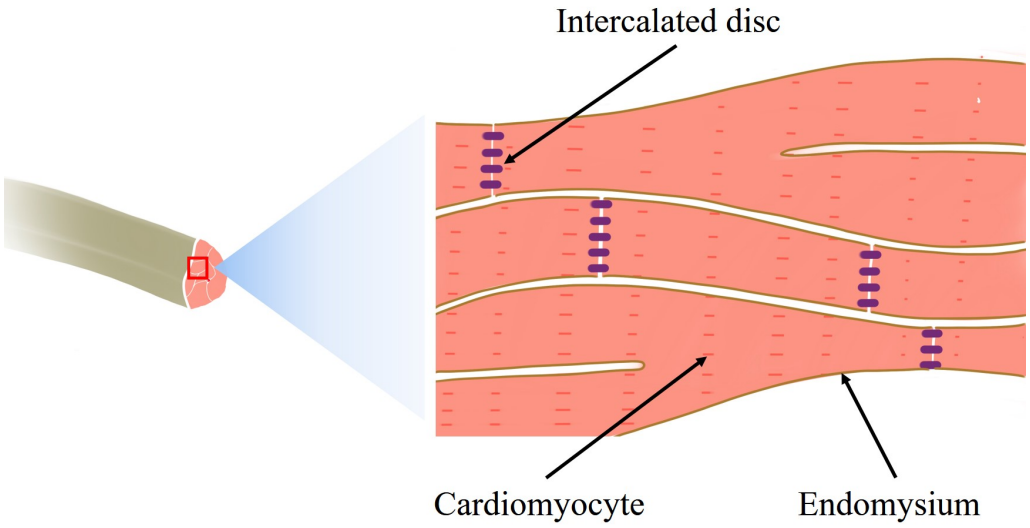

Figure 1.4: *Schematic diagram of cardiomyocytes.*

1.2.3.2 Perimysium

Perimysium is used to describe the extensive meshwork of connective tissue that surrounds cardiomyocyte bundles. It bears the shearing forces between bundles and its lateral strands prevent misalignment between bundles [Ho, 2009].

1.2.4 Cardiomyocyte

The ventricular cardiomyocytes are the main structural component of the myocardium, occupying around 70% of the ventricular wall volume under normal circumstances [Burton et al., 2006]. Cardiomyocytes resemble elongated ellipsoids with an elliptical section of about 10 by 20 μm and a length of 80 to 100 μm, as shown in Fig. 1.4. Cardiomyocytes are bunched and connected end to end by intercalated disks to form a 3D network of cells [Cheng et al., 2005, Dejea et al., 2017]. Each cardiomyocyte is surrounded by a layer of endomysium which contributes to its rigidity [Ho, 2009].

1.3 Cardiac Models

Cardiac geometry is a critical feature in the heart research, which can be represented by 3D cardiac models accurately and realistically. Cardiac structure models have evolved in

recent years. The cardiac muscle was considered as a helical pattern of tissue inside at first [Robb and Robb, 1942]. It was also regarded as a single helical band of muscle coiling around the aortic root and the pulmonary trunk [Torrent-Guasp, 1975]. Later, a doughnut model for the LV was proposed [Streeter Jr, 2005] and then extended to the RV as the pretzel model [Jouk et al., 2000]. Then, the myolaminae model has been proposed to delineate the myocardial laminar structure composed of layers of cardiomyocytes [Hort, 1957b, Caulfield and Borg, 1979, LeGrice et al., 1995b]. On the basis of these cardiac models, several 3D models of different elements of the heart have been developed. Besides that, multiscale models integrating different elements and functions have been proposed.

1.3.1 3D models

As aforementioned, a better knowledge of the 3D arrangement of the heart's structure can help to understand the function of the heart and to research CVDs. Developing 3D models of the heart also contributes to the understanding of the arrangement and remodelling of the heart.

In the past years, 3D geometric models of diverse sections of the heart have been proposed for various but one-fold applications. Moreover, most of them are proposed at a specific scale.

First, 3D shape models of the heart have been studied from anatomic observations to describe the structure of the heart, notably, the LV [Guccione et al., 1991, Nielsen et al., 1991, Ten Tusscher et al., 2007] accompanied by other parts such as the RV and the two atria [Fastl et al., 2018], then to the whole heart [Lorenz and von Berg, 2006, Burton et al., 2006]. The geometric shape models based on the LV and RV are first depicted as ellipsoids [Van den Broek and Van den Broek, 1980]. The architecture and models of the atria have also been investigated [Wang et al., 1995, Vigmond et al., 2001]. Nonetheless, some of the anatomical models lack details because of the poor quality of the data resources, such as histological slices [Vetter and McCulloch, 1998, Nielsen et al., 1991].

With the development of imaging techniques such as Magnetic Resonance Imaging (MRI) and Computed Tomography (CT), image-based models have been developed. They get information from medical images to investigate the heart structure and its de-

formation [Lötjönen et al., 2005, Helm et al., 2005, Deng et al., 2012]. Some parametric models have been proposed for analysing the deformation of the LV [Park et al., 1996] and tracking its surface in a sequence of 3D cardiac images [Bardinet et al., 1996]. Then, blended deformable models modelled the generic 3D shape of the heart and the LV with the RV inside, and they also analysed the cardiac movement and its deformation [Park et al., 2002]. To better investigate the heart's motion, some deformable models are built for describing irregular and unstructured shapes [Bardinet et al., 1998].

Computer-aided design models were proposed to build 3D cardiac models without data resources. Researchers can directly build the 3D cardiac models using the parameters from references [Harrild and Henriquez, 2000].

After having a better knowledge of the basic structure, some 3D models have also been proposed for assisting the reconstruction of the 3D images of the tissue, and 3D motion modelling [Yang et al., 2017].

Moreover, to take into account the research on the structure and movement of the heart, functional models have been proposed. Functional models can help to understand the role of each part of the heart in composing such a complex system, for example, to analyse the LV diastolic mechanics and consequences of drug-channel interactions in the human left-ventricular cardiomyocyte with computational models [Iyer et al., 2004, Palit et al., 2015]. Then, atrial anatomy modelling could provide a deeper understanding of the role that the cardiomyocyte architecture plays in normal and abnormal atrial electric functions [Zhao et al., 2012]. Functional models also allow cardiac mechanical, electrophysiological [Plotkowiak et al., 2008, Sermesant et al., 2007], hemodynamical analysis and water diffusion simulation [Herrling et al., 2017].

Furthermore, with the increasing demand for personalised medical treatment, 3D models are implemented in personalised and clinic areas [Yang et al., 2006, Niederer et al., 2009]. A personalised model has been proposed for integrating and interpreting how electrophysiology works in the development and progression of atrial fibrillation [Fastl et al., 2018]. How to translate 3D models to clinical care has also been discussed in recent years [Winslow et al., 2012, Bozkurt, 2019].

1.3.2 Multiscale models

The heart structure is complex and composed of a series of embedded multiscale elementary objects working together. Data integration across spatial and functional scales is the subject of significant research efforts since the simulation of a functional heart is one of the most intractable problems. Research at the onefold scale studies the myocardium both in healthy and diseased hearts, from the molecular to whole-body levels [Vadakkumpadan et al., 2010]. Multiscale modelling fits biological tissue because the ultimate goal of heart modelling is to generate a model with organs at different levels and the principles to describe how they are arranged and how they work together.

Initially, various multiscale models have been proposed to study the structural relationships in a heart. An automatic labelling approach of the left coronary tree in X-ray angiography on the basis of a 3D topological model has been proposed to overcome the shortcomings of medical diagnosis caused by inter- and intra-clinician variability [Chalopin et al., 2001]. Some multiscale models are used to quantitatively analyze structural substrates, such as wall thickness, myofiber orientation, and fibrosis [Zhao et al., 2017].

Besides structural purposes, some research also focused on the integration of functional parts such as cardiac electrophysiology, hemodynamics, and mechanical function of the heart. A finite element model integrating the electrical, mechanical and biochemical functions of the heart is proposed to link across spatial scales from subcellular protein pathways to integrated cell function and then to tissue and organ behaviour [Smith et al., 2004]. A model focused on the cardiovascular system describes heart cell contraction at a micro-scale and the cardiac pump at a macro-scale [Kosta et al., 2017].

Then these models involved the clinical treatement as well, for example, to model the eccentric and concentric cardiac growth at different scales with a computational model [Göktepe et al., 2010]. For a faster approximation of the behaviour of the heart, a multiscale 0D/3D model has been proposed [Molléro et al., 2016] by a novel coupling method between an original 3D model and a reduced lumped "0D" version of the same model. [Quarteroni et al., 2017] addressed the numerical modelling of many aspects of heart function including the ion-cell-muscle electrophysiological behaviour, the sub-cellular

activation mechanism, the deformation of the tissue, and the ventricular fluid mechanics.

1.3.3 Deformable models

The heart is an elastic kinetic organ. Thus, deformable models are usually applied in heart motion tracking, cardiac image registration and cardiac image segmentation. Deformable models are used for describing region boundaries with closed parametric curves or surfaces, which deform under the effect of internal and external forces [Jayadevappa et al., 2011].

Two dimensional (2D) deformable models were proposed at first to approximate the locations and shapes of object boundaries in images. 2D deformable models, snakes, were proposed as 2D active contours based on the reasonable assumption that boundaries are piece-wise continuous or smooth [Kass et al., 1988].

3D deformable surface models were first used in computer vision [Terzopoulos et al., 1987]. A "balloon" model was built to construct a polygonal approximation to a sphere and it was deformed to conform to the object surface in 3D CT data [Miller et al., 1991]. Then, the "balloon" model was improved using the finite element technique and high-order polynomials [Cohen and Cohen, 1993, McInerney and Terzopoulos, 1995]. The improved "balloon" model provides an analytic surface representation and fewer elements are required to represent an object accurately. A model using a Fourier parameterisation to decompose a surface into a weighted sum of sinusoidal basis functions is proposed to match to 3D medical image data [Staib and Duncan, 1992].

Another main kind of deformable model is the superquadric model. Superquadrics are solid models representing a large variety of standard geometric solids and smooth shapes with a simple parameterisation [with superquadrics: an overview, 1994]. A parametric deformable model using superquadric and FFD was proposed to fit unstructured 3D data [Bardinet et al., 1998]. The superquadric model was also used for representing an unorganised 3D data points set with a union of superellipsoids [Chevalier et al., 2003].

1.4 Image acquisition techniques

3D modelling of the cardiac tissue is influenced to a great extent by the quality of the imaging techniques because most of the anatomical information is evaluated from observations or calculations from medical images. Medical image data have been drivers of cardiac computational modelling because they can capture anatomical information to run simulations, can provide functional information used to build, adjust, and validate models and can be used to estimate model parameters [Lamata et al., 2014].

Although several high-resolution imaging modalities can help understand the anatomy of the cardiac tissue, cardiac modelling is also influenced by their limitations. Transmission Electron microscopy (TEM) provides a high resolution of 0.2 nm while Scanning Electron microscopy (SEM) exhibits a resolution around 50 nm. However, the size of their sample is limited to around 60 µm [Kanzaki et al., 2010]. Confocal microscopy delivers a high reconstruction resolution of 0.4 µm but is limited in the volume size of 35 µm.

Besides the limitation of sample size, most studies are often limited by the anisotropy and/or the low resolution of data, resulting in not able to provide structure details. Diffusion Tensor Imaging (DTI) can provide the arrangements of the cardiomyocytes at a resolution of $1.3 \times 1.3 \times 1.3$ mm^3 [Smerup et al., 2009]. Using Polarized Light Imaging (PLI), the resolution can be improved at $90 \times 90 \times 500$ µm^3 due to the crystalline uniaxial positive birefringence of myosin [Jouk et al., 2018]. Last high resolution MRI can provide an even finer resolution of $50 \times 50 \times 50$ µm^3 [Davidović et al., 2020]. In the last decade, the Micro-CT (µ-CT) imaging technique has been developed and can provide fibre analysis in the atrial section of canine hearts with a high resolution of $36 \times 36 \times 36$ µm^3 [Aslanidi et al., 2012].

1.4.1 Dissection and histology

Dissection and histology are the most primordial and widely used techniques. They are often used in cardiac structure research [Harrington et al., 2005]. In the laminar structure study, two populations of sheetlets were found through the quantitative histological analysis of the ventricles [Costa et al., 1999, LeGrice et al., 1995b]. The maximum resolution of the histological optical image is 0.3 µm.

1.4.2 Echocardiography

Echocardiography is the most used imaging technique in clinics because of its property of low cost, safety, quick evaluation and high portability. Echocardiographic images are useful in the study of tissue deformation [Mondillo et al., 2011]. In recent years, 3D echocardiography has been developed and is suitable for RV modelling and cardiac valve modelling [Lang et al., 2012].

1.4.3 Computed tomography

CT can provide remarkable spatial resolution, adequate temporal resolution, and relatively poor contrast resolution [Lin and Alessio, 2009]. But it has the defect of exposing patients to ionizing radiation. It is often adopted in cardiac morphological characteristics [Nerlekar et al., 2018], functional properties [Ko et al., 2019] and perfusion assessment [Peebles, 2013].

1.4.4 Magnetic resonance imaging

MRI is a non-invasive imaging technique which can be used for imaging the heart *in vivo*. MRI data can provide a wide range of information such as cardiac anatomy, mechanics and perfusion [Lamata et al., 2014]. A large number of cardiac models are based on MRI scans to depict the left and RVs [Lorenz and von Berg, 2006]. Diffusion Tensor MRI (DT-MRI) exploits the stronger diffusion of water molecules along the cardiomyocyte direction to obtain the cardiomyocyte orientations [Ferreira et al., 2014], and cardiac microstructure [Axel et al., 2014].

1.4.5 Polarized light imaging

PLI is a contrast-enhancing technique that improves the quality of the image obtained with birefringent materials [Carlton, 2011]. In heart imaging, it allows extracting the voxel principal orientation, which is the mean orientation of all cardiomyocytes contained in a voxel. The orientation information is expressed by two angles: the azimuth angle $[0°, 180°]$ and the elevation angle $[-90°, 90°]$ [Jouk et al., 2018].

1.4.6 Phase contrast micro-CT

The contrast in the image obtained by the X-ray μ-CT technique is proportional to the differences in absorption of the locally adjacent tissues that make up the sample. Nevertheless, due to the low absorption contrast in soft tissues such as heart samples, it is hard to obtain high-quality images. Therefore, phase contrast imaging is used to improve the μ-CT image quality [Cloetens et al., 1999].

The recent work of our group provides some 3D X-ray phase contrast μ-CT data at a micrometric isotropic spatial resolution of $3.5 \times 3.5 \times 3.5$ μm^3, which includes quantitative knowledge about the 3D arrangement of the cellular matrix (CM) and extracellular matrix within fresh human post-mortem heart samples [Mirea, 2017, Mirea et al., 2016, Varray et al., 2017]. The heart samples were imaged using the synchrotron light in Synchrotron Radiation Phase micro-Computed Tomography (SR-PCT) imaging at the European Synchrotron Radiation Facility (ESRF) which is a particle accelerator located in Grenoble, France. 2499 projections were obtained on each sample, and after phase retrieval [Paganin et al., 2002], reconstruction was done using filtered back projection.

1.5 Conclusion

The advancement of imaging techniques has a crucial role in clinical diagnosis. These medical imaging techniques provide a better knowledge of the 3D structure of the heart which can be employed to build cardiac models to investigate the relationship between structures and functions of the heart.

On the basis of this background, the objective of my thesis is to build a 3D multiscale deformable model to describe the basic 3D structure along with the geometric shape and features of major elements of the heart. The model can be used to investigate the 3D structure of the heart and its elements, generate virtual volumes for virtual imaging and achieve other functional applications.

The proposed 3D multiscale model crosses the scales from the global level (macro-scale) to the tissue level (micro-scale) integrating several elementary objects of the heart. Thus, a brief introduction to the cardiac structure has been elaborated, including the

structure of four chambers, the laminar structure of the myocardium, the fibre architecture and the cardiomyocytes.

To describe the structure and function of these cardiac elements, several 3D models have been introduced. Being a complex organ, the heart was investigated at several scales. Multiscale models were introduced, integrating the properties crossing spatial and functional scales. The heart is also elastic, so some deformable models have been stated.

Due to the influence of image acquisition techniques on cardiac modelling, the resolutions and limitations of different imaging modalities have been introduced.

Based on these introductions, the proposed 3D multiscale model is presented in the following chapters.

Chapter 2

Multiscale Deformable model

Contents

2.1 Introduction

As described in Chapter 1, the heart is a complex organ composed of several elements at various scales. These elements connected and joined together anatomically enable the heart to work normally. So it is essential to focus the studies on multiple elements and scales when researching the structure and functions of the heart, such as the connectivity among different elements or how the heart remodels during the cardiac cycle. Therefore, a multiscale heart model consisting of elements at various scales is necessary and valuable for research on the heart.

In terms of the basic structure of the heart, I proposed a multiscale model containing the main anatomical elementary structures of the heart at five levels from the macro- (cm) to the micro-scale (μm). It includes the cavities (ventricles, atria), the CE (sheetlets, cardiomyocyte bundles, and individual cardiomyocytes), and the ECM (cleavage planes, endocardium, epicardium, and perimysium).

This chapter introduces the structure and properties of the proposed multiscale deformable model. It is a hierarchical, voxel-based, and object-oriented model. Software structures for every object are built using Matlab MathWorks. Moreover, the deformation technique is also introduced into the model for attaching the elastic properties.

2.2 Hierarchical structure

According to anatomical and histological knowledge [Torrent-Guasp et al., 2005, Ho et al., 2002, Ho, 2009, Weinhaus and Roberts, 2005], the human heart is a four-chambered muscular organ with vessels, nerves, valves and other complex systems. Three layers of tissue constitute the heart wall. The outer layer of the heart wall is the epicardium, the middle layer is the myocardium, and the inner layer is the endocardium. The myocardium consists of cardiomyocytes arranged in overlapping spiral patterns along cleavage planes, which makes the myocardium have a laminar structure [Treuting et al., 2017, LeGrice et al., 1995a].

Therefore, the whole model is divided into five levels at various scales. At each level scale, there are several elementary structures. Each element of the heart is considered as

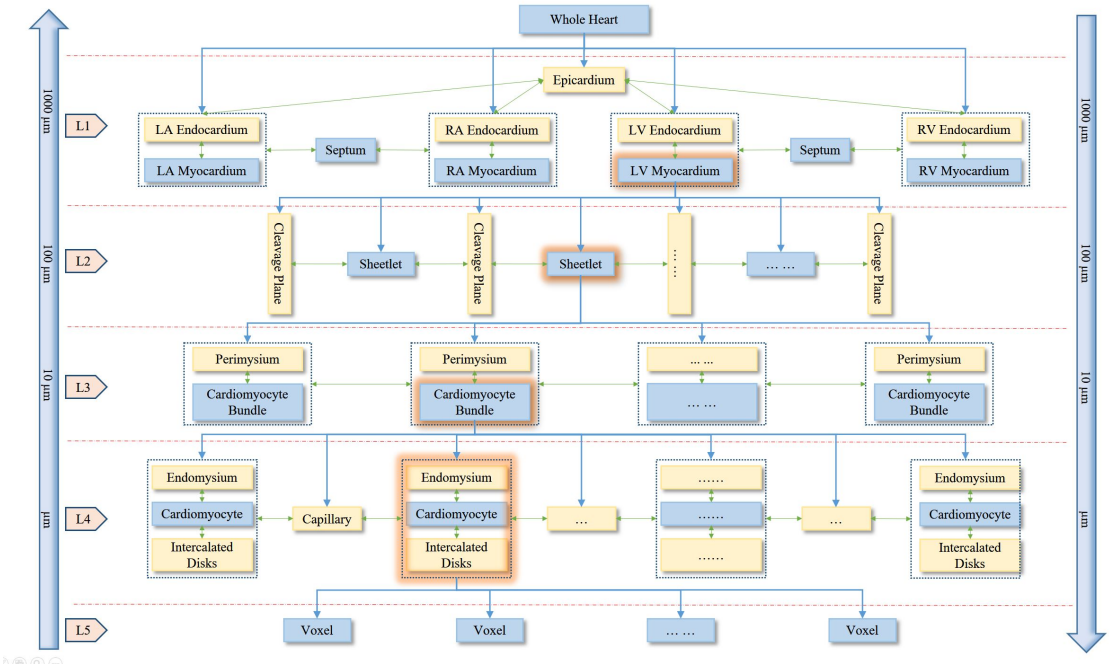

Figure 2.1: *Structure of the multiscale model. LA: Left Atrium. RA: Right Atrium. LV: Left Ventricle. RV: Right Ventricle. L1-L5: Levels corresponding to the scales of the model. Blue blocks: CE. Yellow blocks: ECM.*

an object. The topological structure of the model is presented in Fig. 2.1 as well as the relationship between these objects and the levels. In the structure, the objects are like nodes in a net that can be connected (same scale) or nested within another (larger scale). Each of them is composed of a geometric model (shape imitating the anatomy) to which a vector of characteristics is attached to store its parameters. 3D volumes can be generated according to the geometric model while each voxel inside is given a label of the object it belongs.

Along the vertical direction of Fig. 2.1, an object belonging to level N contains the objects of level $N+1$. Meanwhile, the spatial resolution varies from centimetre to micrometre. Along the horizontal direction, all objects belonging to the same level are mutually connected. This description generates a 3D hierarchical topological graph where the blue arrows indicate affiliations and the green ones indicate connectivities.

2.2.1 Level 1

This level is the root of the model comprising objects of the macroscopic scale. In terms of histological and functional information about the heart, the objects correspond to the heart's four chambers, i.e. two atria and two ventricles. They include anatomical features such as the epicardium, endocardium, and myocardium of each atrium and ventricle and the septum separating the four chambers [Sylva et al., 2014]. This level addresses functional issues such as global shape deformation or cavities volume changes along the cardiac cycle.

2.2.2 Level 2

This level focuses on the cardiac tissue, more specifically the cleavage planes belonging to ECM with the sheetlets. They are related to the laminar structures and the mechanical properties of the tissue.

2.2.3 Level 3

This level mainly deals with the cardiomyocyte bundles of CM embedded in the perimysium of the ECM. The local twist and sliding of the ECM and CM arising at levels 2 and 3 contribute to the global deformation of the myocardium.

2.2.4 Level 4

This level concerns the cellular level with individual cardiomyocytes as basic functional units in the heart. The objects at this level are parts of a cardiomyocyte module including the cardiomyocyte, the endomysium, and the intercalated disk. The cardiomyocyte modules along with the capillary compose a cardiomyocyte bundle.

2.2.5 Level 5

This level corresponds to the leaves of the graph model described by voxels at a microscopic scale. It is the basic unit of our multiscale model while its size affects the resolution

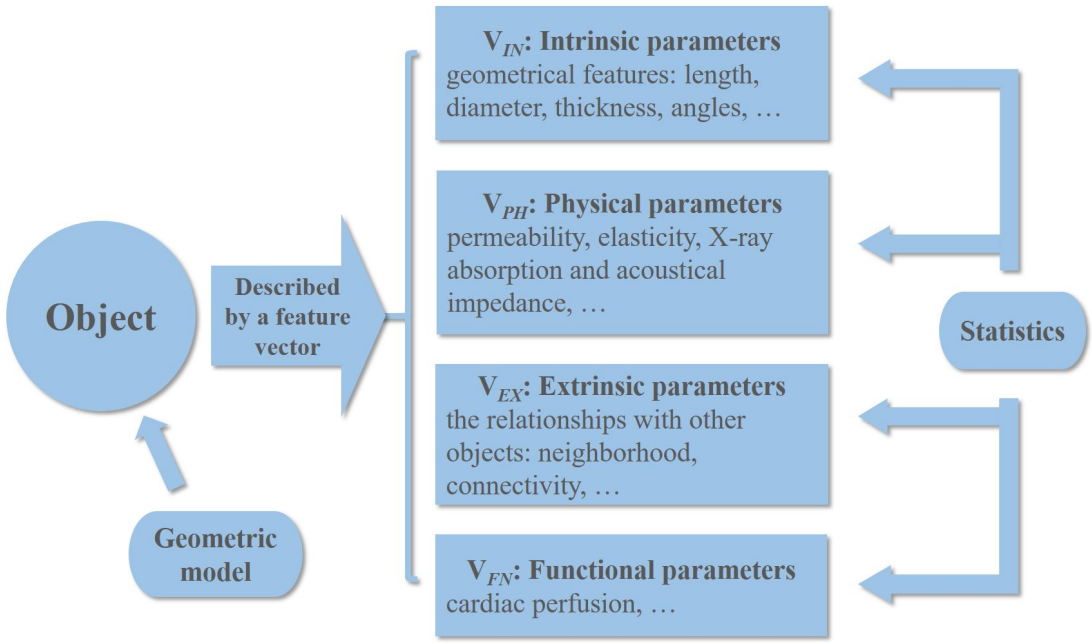

Figure 2.2: *Structure of each elementary object. Each object is given a geometric model and a feature vector.*

of the whole model. Each voxel is attached with a label indicating an affiliated object and also a parameter vector.

2.3 Voxel-based model and software structure

2.3.1 Object-oriented description

Object-oriented approaches are implemented on our multiscale model because of their capability of representing related and affiliated objects in a compact and coherent form. It allows a hierarchical decomposition of the heart by inheritance in programming which is the basis for effective, correct, and reuse of knowledge [Hakman and Groth, 1999]. With this approach, each object possesses its class of properties which is coded separately, but across different levels, the classes are mutually related and have an inheritance relationship. A class can store the information and status of one object. The procedure in the class can be operated on the object itself and can be used to generate a new object.

In our model, each level N contains a series of objects mainly described by a feature

vector V of parameters, while this vector is saved in classes as shown in Fig. 2.2. The feature vector stores parameters of intrinsic, physical, functional, and extrinsic fields, inspired by anatomical knowledge and statistical measurements. In Eq. (2.1), I give a genetic description of all objects including the four sides of parameters. Among these features, geometric information such as dimension and orientation is included as intrinsic parameters V_{IN} describing an object's configurations. The relationships such as connectivity and affiliation are included as extrinsic parameters V_{EX} describing the position in the hierarchical network. The physical information V_{PH} such as electrical or acoustical impedance is included as physical parameters which are involved in diverse imaging techniques. Some objects play roles in heart functions, so functional parameters V_{FN} should also take into account. Then, the feature vector could be considered as:

$$V_{Object} = \begin{bmatrix} V_{IN} & V_{PH} & V_{FN} & V_{EX} \end{bmatrix}^T \tag{2.1}$$

According to each specific object, the feature vector includes various content. Taking the cardiomyocyte bundle as an example, according to the description in Chapter 1.2, a detailed feature vector has the form:

$$\begin{cases} V_{IN} &= \begin{bmatrix} POS & R_x & R_y & R_z & V_{FFD} \end{bmatrix}^T \\ V_{PH} &= \begin{bmatrix} V_{Img} & V_{Mdl} \end{bmatrix}^T \\ V_{FN} &= \begin{bmatrix} \ ... \ \end{bmatrix}^T \\ V_{EX} &= \begin{bmatrix} V_{CM}^1 & V_{CM}^1 & ... & V_{CM}^N \end{bmatrix}^T \end{cases} \tag{2.2}$$

with

$$\begin{cases} V_{Img} &= \begin{bmatrix} V_{XRay} & V_{US} & V_{MRI} & ... \end{bmatrix}^T \\ V_{Mdl} &= \begin{bmatrix} V_{Dyn} & V_{Mch} & ... \end{bmatrix}^T \end{cases} \tag{2.3}$$

The intrinsic vector, V_{IN} is used to describe the geometric shape, where POS denotes the position of its centre, R_x, R_y and R_z is the axis of the initial cylinder along the x, y, and z axis, V_{FFD} describe the control points for deforming the initial cylinder (details in

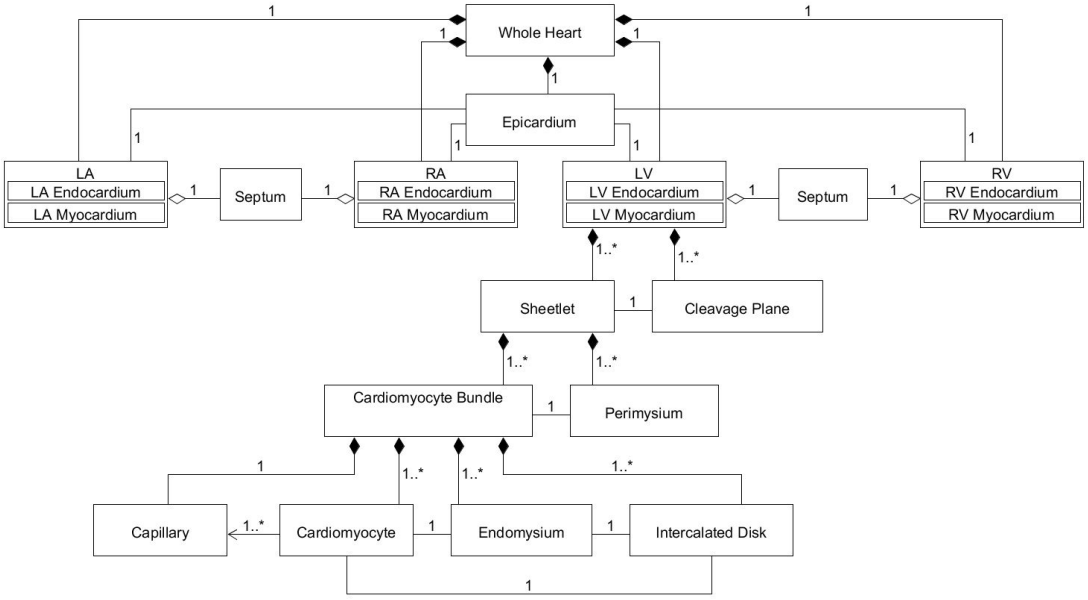

Figure 2.3: *General class diagram illustrating the relationships among classes for all the objects.*

Chapter 4). The physical vector, V_{PH} is divided into two parts: V_{Img} and V_{Mdl}, where V_{Img} consists of parameters for virtual imaging such as X-ray, Ultrasound, and MRI while V_{Mdl} consists of parameters of different models. The extrinsic vector, V_{EX}, is composed of the subordinated cardiomyocyte objects.

2.3.2 Software structure

Fig. 2.3 illustrates the class diagram showing the relationships among the objects of the whole multiscale model. I also give one example of the software structure for one object at each level, where Fig. 2.4 represents the "LV myocardium" at $L1$, Fig. 2.5 represents the "sheetlet" at $L2$, Fig. 2.6 represents the "cardiomyocyte bundle" at $L3$ and Fig. 2.7 represents the "cardiomyocyte" at $L4$ (the class diagrams of other objects in our model can be found in Appendix A). In each object, besides the attributes, functions can be called to achieve different purposes. Each object at level N inherits the attributes from its parents of level $N-1$ to achieve the object-oriented description.

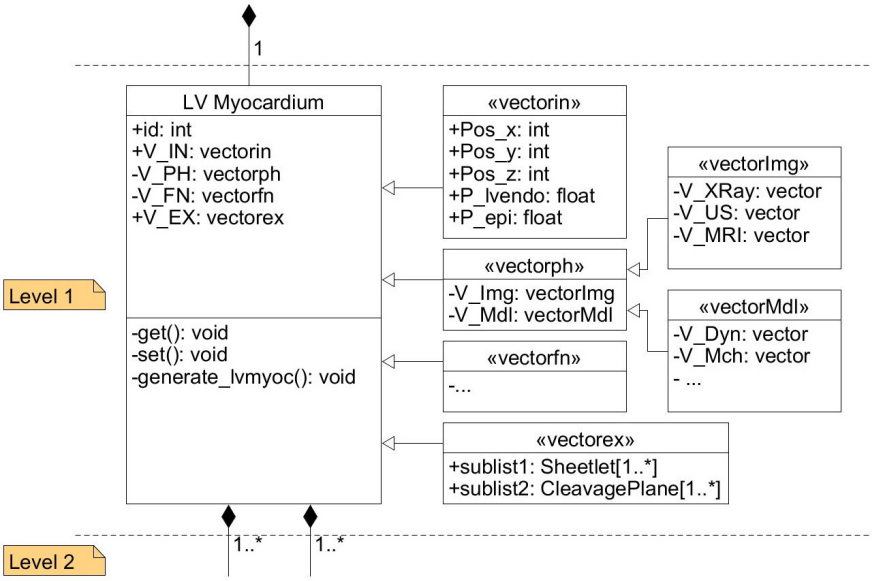

Figure 2.4: *Class diagram of object "LV myocardium".*

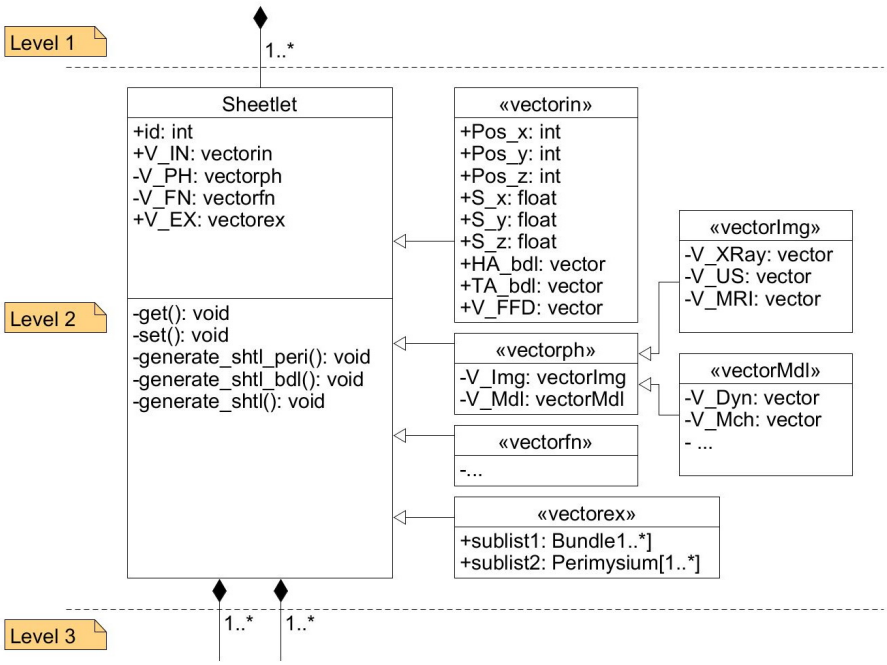

Figure 2.5: *Class diagram of object "sheetlet".*

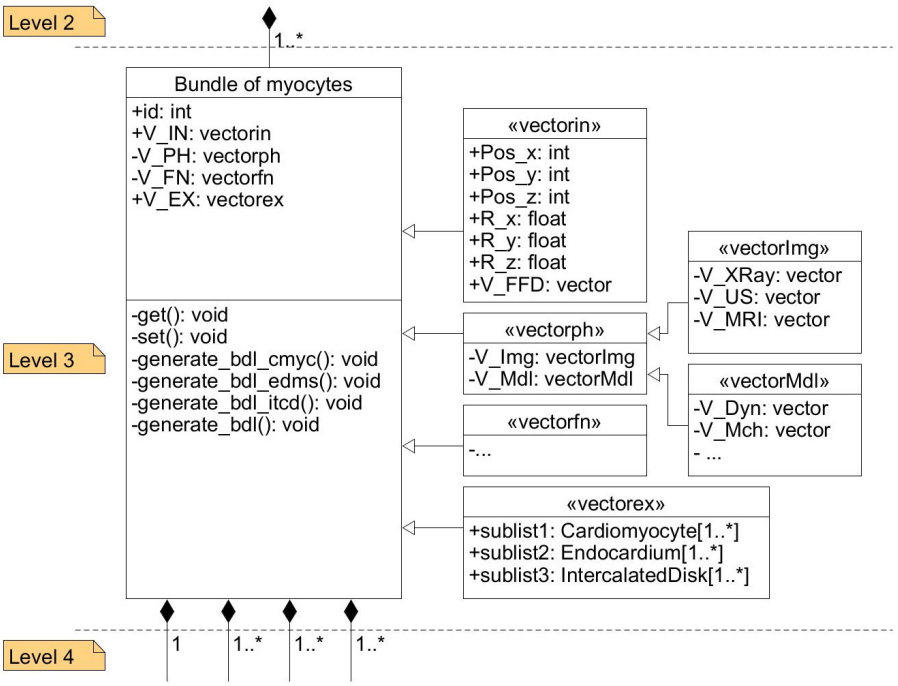

Figure 2.6: *Class diagram of object "cardiomyocyte bundle".*

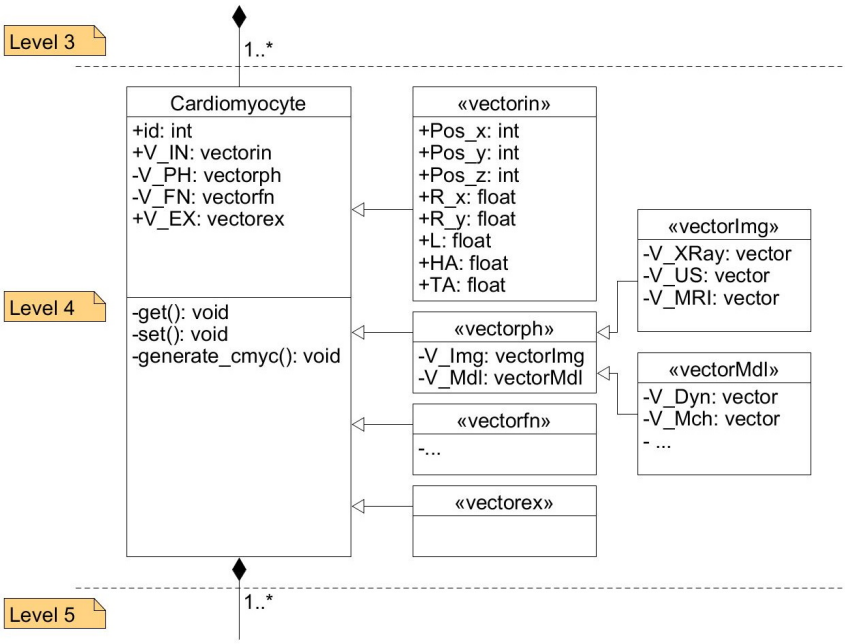

Figure 2.7: *Class diagram of object "cardiomyocyte".*

2.3.3 Voxel-based model

Voxels are used as basic units in our model. Indeed, voxel-based models are well adapted to represent the complex structures of the human anatomy as they are designed from real anatomy. Moreover, they are flexible and can be scaled in size to match any required dimension or deformation [Caon, 2004]. To set up voxel-based models, I first need to identify the boundaries between the objects contained in the model. Second, I need to label all of the voxels belonging to the same organ with a unique identification. Thus, each voxel is identified, distinguished and different from the others through labelling and indexing. Voxels of the same object belong to the same class. Since voxels are the basic units of our model, their resolution represents the lowest scale of the whole model. They are also the basic units for virtual imaging, so they are the main and actual carriers of the physical parameters.

2.4 Deformation property

The first goal of our model is to describe the geometric shape constituting the objects in the heart. However, the heart is a functional elastic organ, where the deformation and subtle rearrangements of the tissue constantly happen during the cardiac cycles. Thus, deformations must be taken into account in our geometric models for each elementary object. Therefore, after descriptions of the basic structures and properties of the objects, I introduce some deformation properties into the model.

Deformable models are capable of simulating diverse morphology for the same object at different moments and across different individuals. They are widely used for describing biological shapes because of their ability to segment, match, and track images of anatomic structures by exploiting constraints derived from the image data together with prior knowledge about the location, size, and shape of these structures [McInerney and Terzopoulos, 1996].

2.4.1 Deformation method - free-form deformation

To deform the objects, an appropriate deformation method is necessary. The deformation process is a kind of shape optimization problem. In recent years, several shape optimization techniques have been proposed and can be grouped into 3 classes: Finite Element Method (FEM) based methods, IsoGeometric Analysis (IGA) based methods, and Meshless Methods (MM) [Upadhyay et al., 2021]. FEM-based methods are a bunch of dominating methods such as extended FEM with level sets [Moës et al., 1999], fixed grid FEM/Eulerian approach [Suzuki and Kikuchi, 1991], interface enriched generalized FEM [Soghrati et al., 2012] and finite cell method [Parvizian et al., 2007]. IGA methods are strategies to mitigate issues related to inconsistent geometry description [Wall et al., 2008, Kostas et al., 2015, Shaaban et al., 2020]. MMs mainly contain parametric [Braibant et al., 1985] and free-form techniques [Chen et al., 2007].

Among the above various possible approaches, Free-Form Deformation (FFD) technique has been selected to deform the geometric shapes in our model. FFD is introduced at each level of the model.

FFD is a mature shape deformation technique originally proposed by Thomas W. Sederberg to deform solid geometric models [Sederberg and Parry, 1986]. FFD firstly re-defines the location of a geometric object in a local coordinate system and then defines a grid enveloping the object where the intersections of the grid are called control points. Next, FFD uses a set of equivalent dimensional Bernstein polynomials to build a reflection between the object and the control points. This reflection is represented by a tri-variate tensor product of polynomials which is an important notion in approximation theory and guarantees the smoothness in the deformation. When the locations of the control points shift, the coordinates of the object are transformed as well. Thus, the free-form movements of the control points result in the deformation of the shape.

FFD does not have restrictions on the types, shapes, or scales of the objects and it can be applied at any scale in our model. Moreover, the parametric objects remain parametric after FFD which is valuable during shape modelling. Besides that, it is possible to control the volume of the objects during the FFD process, which makes us able to control the volume of tissue during the deformation. Moreover, several FFDs can be operated piece-

wisely on the same object.

On the basis of these properties of FFD, and its suitability for our multiscale model, I use the FFD technique to fit the model to the real data such as the data-fitting of the membranes in the ECM, and deform the shapes of each elementary object composing the heart from the macro- to the micro-scale, such as the twisting of the cardiomyocyte bundle during the heart cycling, the curved and merged structures of objects and the simulations of different parts of the tissues using a universal template.

2.4.2 Principle

To implement FFD, a local coordinate system $(S,T,U) \in \mathbb{R}^3$ is first defined with the origin situated on one of the vertexes of the smallest rectangular box containing the data. The dimension of the domain is defined by the coordinate range (min-max) in the three directions. In this local coordinate system, the original coordinates of the data to be processed $\mathbf{X}$ within the domain can be expressed as:

$$\mathbf{X} = \mathbf{O_L} + s\vec{S} + t\vec{T} + u\vec{U} \tag{2.4}$$

where $\mathbf{O_L}$ states for the origin of the local coordinates system and the local coordinates (s,t,u) of any point inside the data can be calculated by:

$$(s,t,u) = \left(\frac{\vec{T} \times \vec{U} \cdot (\mathbf{X} - \mathbf{O_L})}{\vec{T} \times \vec{U} \cdot \vec{S}}, \frac{\vec{S} \times \vec{U} \cdot (\mathbf{X} - \mathbf{O_L})}{\vec{S} \times \vec{U} \cdot \vec{T}}, \frac{\vec{S} \times \vec{T} \cdot (\mathbf{X} - \mathbf{O_L})}{\vec{S} \times \vec{T} \cdot \vec{U}} \right) \tag{2.5}$$

with $s \in [0,1]$, $t \in [0,1]$, $u \in [0,1]$, where "$\times$" and "$\cdot$" denote the outer and inner products of vectors, respectively.

The second step is to immerse the unprocessed data into a 3D grid of control points $\mathbf{P}$ of size $(l+1) \times (m+1) \times (n+1)$. Then, the coordinates of each control point $\mathbf{P_{ijk}}$ are given by:

$$\mathbf{P_{ijk}} = \mathbf{O_L} + \frac{i}{l}\vec{S} + \frac{j}{m}\vec{T} + \frac{k}{n}\vec{U} \tag{2.6}$$

with i, j, k being the index of each control point along the $\vec{S}$, $\vec{T}$ and $\vec{U}$ directions in the local coordinates system, respectively.

The displacements of the control points result in the deformation of the object, while the trivariate tensor product Bernstein polynomial defines the deformation function between them:

$$X_{FFD} = \sum_{i=0}^{l}\sum_{j=0}^{m}\sum_{k=0}^{n} C_l^i (l-s)^{l-i} s^i C_m^j (l-t)^{m-j} t^j C_n^k (l-u)^{n-k} u^k \mathbf{P}^*_{\mathbf{ijk}} \tag{2.7}$$

with $\mathbf{P}^*_{\mathbf{ijk}}$ being the moving control points.

2.4.3 FFD on simple shapes

For a more intuitive illustration, I give some examples of FFD on some simple geometric shapes. To show the universality of FFD, I use 4 usual shapes to deform, including an ellipsoid, a cuboid, a cylinder, and a cube. As Fig. 2.8 shows, I design a $3 \times 3 \times 3$ grid of control points with homogeneous interval distances at each axis. By displacing the control point, after FFD, I get the deformed shapes. In the first experiment, the ellipsoid is increased by 1.5 times by amplifying the coordinates of control points. In the second one, the cuboid is shrunk to half of it using the same strategy. In the third experiment, I displaced the control points in different layers by different distances to create a curved structure. In the last experiment, the control points are moved at random lengths and directions to get a randomly deformed shape.

2.5 Conclusion

In this chapter, I propose a multiscale model of the heart. I design the hierarchical structure of the model with 5 levels to describe the heart from the macro- to the micro-scale. The model is object-oriented as it allows a hierarchical decomposition of the heart and better reuse of knowledge at each level. Then, I give examples of the software structures for a general fabric of the model and one object on each level. It is also a voxel-based model because voxels are the basic units of our model and the voxel-based model is more flexible to scale in size and deform. Moreover, virtual imaging usually depends on a voxel-based model. For a better description of the geometric shapes of the objects in the heart, I introduce the deformation process into our model. Among several deformation

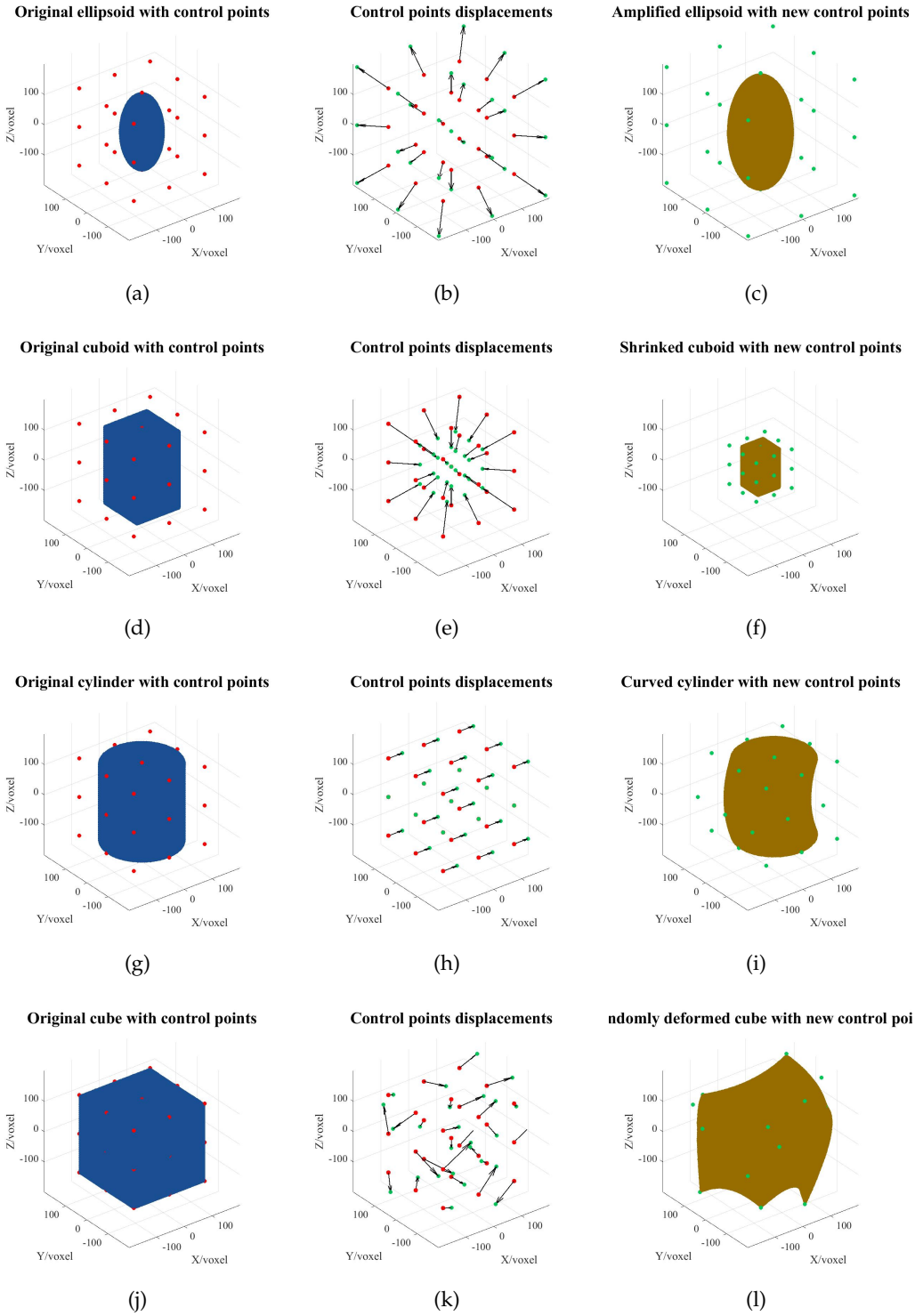

Figure 2.8: *FFD on simple geometric shapes. (a), (d), (g), and (j) are original shapes. (b), (e), (h), and (k) are the displacements of control points. Red points are the original control points while the green ones are the displaced ones. (c), (f), (i), and (l) are the deformed shapes.*

techniques, I selected FFD to deform the shapes of the objects because it does not have restrictions on shapes and it can be utilized at each level of our model. I introduce its principle of it and give some examples of deformation of some basic geometric shapes.

Chapter 3

Low-resolution model

Contents

3.1 Introduction

Since our model goes from macro- to micro-scale (see Fig. 2.1), I divide the whole model into two parts: (i) the low-resolution model, which is $L1$ at a resolution around 1000 µm, and (ii) the high-resolution model ($L2$, $L3$ and $L4$) with resolutions 100 µm. In this chapter, I introduce how to build the low-resolution model focusing on the LV epicardium and LV endocardium. For compatibility with the resolution of $L1$, I use the cardiac PLI data whose resolution is $90 \times 90 \times 500$ µm^3 as a data resource to simulate the geometric shapes of the two objects: partial epicardium and LV endocardium. According to the anatomical knowledge described in section 1.2, the epicardium is the outermost protective layer of the heart, and the endocardium is the innermost layer that lines the heart chambers, which means that during the heart cycle, they are both remodelled. A surface model with deformation properties is then necessary when building the geometric shape. Therefore, I adapt the method proposed in [Bardinet et al., 1998] to build a deformable surface model to simulate the shapes of the partial epicardium and LV endocardium.

3.2 Superquadric model with FFD

The superquadric model is one of the parametric deformable templates with the ability to represent a shape with a small number of parameters [Barr, 1981b]. It was first used to coarsely describe the shape of the LV [Chen et al., 1994, Barr, 1981a]. It was also applied with tapering and bending deformations to model the LV for shape analysis [Chen et al., 1995]. Then, superquadrics became a commonly basic surface model in cardiac modelling. A superquadric-based thorax phantom is used for simulations of CT [Zhu et al., 2005]. The superellipsoid model was used as the basic surface model for epicardium to perform the 4D segmentation of the LV [Tay et al., 2009]. Because of its ability to describe the surfaces in LV, a superquadric model is adopted as the primary model for my low-resolution model. Among all the superquadrics, the superellipsoid is used as the initial superquadric shape because it is the only one that defines a closed surface [Barr, 1987] and the shape of the LV resembles an ellipsoid as well. However, the superellipsoid model is highly symmetric, which is insufficient to mimic the complicated shapes

of the LV epicardium and endocardium. So, after a coarse data-fitting of the shape, deformation is usually considered in the model to refine the data-fitting [Terzopoulos et al., 1987, Jaklic et al., 2000, Štern et al., 2011, Ayari et al., 2017]. In this chapter, FFD is used as a deformation technique to accomplish fine data fitting.

3.2.1 Superellipsoid

A superellipsoid is usually defined by an implicit equation:

$$f(x,y,z) = \left(\left(\frac{x}{a_1} \right)^{\frac{2}{\varepsilon_1}} + \left(\frac{y}{a_2} \right)^{\frac{2}{\varepsilon_1}} \right)^{\frac{\varepsilon_2}{\varepsilon_1}} + \left(\frac{z}{a_3} \right)^{\frac{2}{\varepsilon_1}} \tag{3.1}$$

where (x,y,z) are the coordinates for each point, a_1, a_2, and a_3 are scaling factors along x, y, and z controlling the size of the ellipsoid, and ε_1, ε_2 are two constraint factors controlling the curvatures of the shape: ε_1 controls the squareness of the vertical planes along z direction and ε_2 controls the squareness of the planes parallel to $x-y$ plane. The impact of ε_1 and ε_2 on the shapes is highlighted in Fig. 3.1.

Using Eq. (3.1), the relative position between points and the superellipsoid can be determined by the valuence of $f(x,y,z)$. The rules are:

- $f(x,y,z) = 1$, when the point is exactly on the superellipsoid surface;
- $f(x,y,z) < 1$, when the point is inside the superellipsoid;
- $f(x,y,z) > 1$ when the point is outside the superellipsoid.

3.2.2 Coarse data-fitting using a superellipsoid model

According to the basic superellipsoid in Eq. (3.1), I adapt the proposed model and method presented in [Bardinet et al., 1998]. The initial superellipsoid model is:

$$g(x,y,z) = \left(\left(\frac{x-t_x}{a_1} \right)^{\frac{2}{\varepsilon_1}} + \left(\frac{y-t_y}{a_2} \right)^{\frac{2}{\varepsilon_1}} \right)^{\frac{\varepsilon_2}{\varepsilon_1}} + \left(\frac{z-t_z}{a_3} \right)^{\frac{2}{\varepsilon_1}} \tag{3.2}$$

where t_x, t_y and t_z are the translation of the center of the superellipsoid. In [Bardinet et al., 1998], the superellipsoid is determined by 11 parameters which include three more

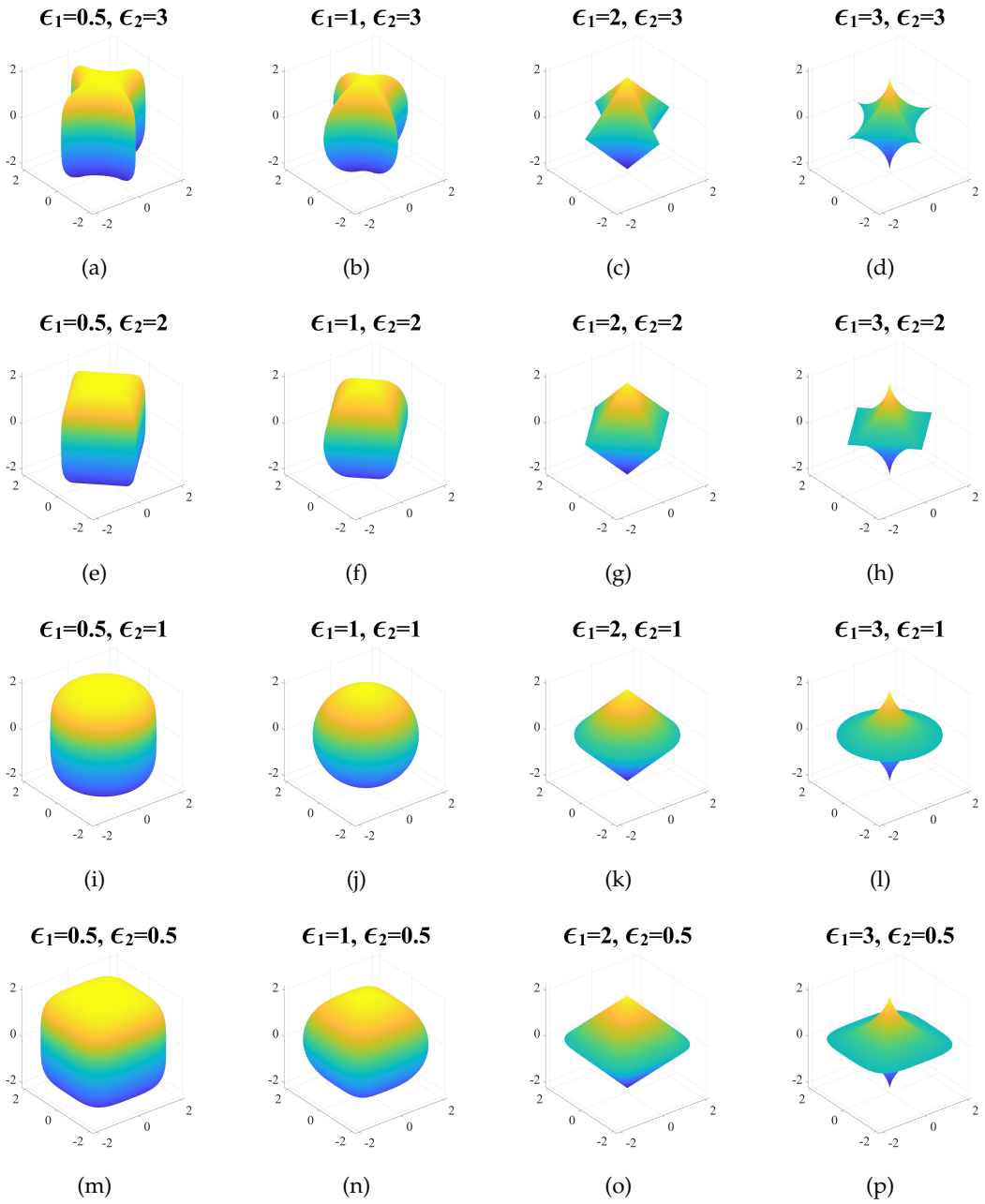

Figure 3.1: *Superellipsoid varies with its parameters ε_1 and ε_2. In each row, the squareness of the longitudinal plane changes along with ε_1. In each column, the squareness of the latitudinal plane changes along with ε_2.*

parameters to control the rotation of the object. However, the shapes of the epicardium and endocardium are closed surfaces without very distinct extremes. And in the next section, fine data-fitting, FFD is capable of fitting the model to the data well without rotating the superellipsoid. For these reasons, I eliminated the three rotation parameters reducing the 11 parameters into 8 parameters. Then, using a set of 8 parameters: $p_8 = (a_1, a_2, a_3, \varepsilon_1, \varepsilon_2, t_x, t_y, t_z)$, an ellipsoid which fits to the data can be determined.

Generally, it does not exist a p_8 vector making the superellipsoid perfectly fit the data because the real shapes are more irregular than the highly symmetric superellipsoid. Therefore, to fit the data, the problem is formulated and solved as a least-squares problem [Abdi et al., 2007]. Let $\mathbf{D} \in \mathbb{R}^{N_D \times 3}$ be the data matrix containing N_D coordinates $\vec{d} = (x_d, y_d, z_d)$. Then the problem is to find the best set of parameters by solving the minimization problem as:

$$\arg\min_{p_8 \in \mathbb{R}} \sum_{N}^{1} (1 - g(\mathbf{D}, p_8))^2. \tag{3.3}$$

From Fig. 3.1, it can be observed that even with the eight parameters, the shape of the superellipsoid is highly symmetric. Thus, the superellipsoid model alone is insufficient to describe the geometric shape of the objects in the heart since their shapes are usually irregular. It is then necessary to introduce a deformation technique to enable the superellipsoid to better fit real shapes. On the basis of the description in Section 2.4.1, FFD can deform the superellipsoid with only a small set of control points. Therefore, FFD is introduced into the superellipsoid model.

3.2.3 Fine data-fitting using FFD

According to the introduction in section 2.4.2, FFD can be used to fit the superellipsoid to the data finely. On the basis of Eq. (2.7), the relationship between $\mathbf{X}$ and $\mathbf{P}$ can be written as:

$$\mathbf{X} = \mathbf{B} \cdot \mathbf{P} \tag{3.4}$$

where $\mathbf{X} \in \mathbb{R}^{N_X \times 3}$ is the matrix of the coordinates of the N_X superellipsoid points, $\mathbf{P} \in \mathbb{R}^{\mathbf{N_P} \times \mathbf{3}}$ is the matrix of the coordinates of N_P control points generated according to $\mathbf{X}$, and $\mathbf{B} \in \mathbb{R}^{N_X \times N_P}$ is the transformation matrix.

Using the same transformation matrix $\mathbf{B}$, when the control points $\mathbf{P}$ are displaced, the position of the superellipsoid points will be moved, which means the shape of the superellipsoid is deformed. Thus, the goal is to find an ideal set of control points $\mathbf{P}^*$, by which the simulated shape $\mathbf{X}^*$ can be calculated.

Using the Singular Value Decomposition, the Moore-Penrose inverse matrix of $\mathbf{B}$ can be calculated, denoted by $\mathbf{B}^\dagger$ [Hartwig, 1976]. In an ideal situation, matched set of control points $\mathbf{P}^*$ can be calculated by:

$$\mathbf{P}^* = \mathbf{B}^\dagger \cdot \mathbf{D}. \tag{3.5}$$

However, the sizes of $\mathbf{D}$ and $\mathbf{X}$ are different, with considerable quantity (million level), making it usually impossible to calculate directly. Therefore the problem is transformed into a least-square minimization problem defined as:

$$\arg\min_{\mathbf{P}} \|\mathbf{D} - \mathbf{B} \cdot \mathbf{P}\|^2. \tag{3.6}$$

Finally, the procedure described in Algorithm 1 is used to calculate the relative ideal control points $\mathbf{P}^*$.

Algorithm 1 Data-fitting of the low-resolution model.

Input:
$\mathbf{D}$, $\mathbf{P}$, $\mathbf{B}$, $\mathbf{X}$, ϵ;
Output:
$\mathbf{P}^*$,$\mathbf{X}^*$;
$\mathbf{P}^{(0)} \leftarrow \mathbf{P}$;
$\mathbf{X}^{(0)} \leftarrow \mathbf{X}$;
$n \leftarrow 0$;
repeat
  Calculate $\mathbf{P}^{(n+1)}$ by solving the minimazation problem in Eq. (3.6)
  $\mathbf{X}^{(n+1)} = \mathbf{B} \cdot \mathbf{P}^{(n+1)}$
  $n = n + 1$
until $\left\|\mathbf{X}^{(n+1)} - \mathbf{X}^{(n)}\right\| < \epsilon$

In this procedure, the input matrix $\mathbf{X}$ is used to design matrix $\mathbf{P}$ and to calculate the FFD transformation matrix $\mathbf{B}$. They are used as the initialization of the iterators $\mathbf{X}^{(n)}$ and $\mathbf{P}^{(n)}$ which are updated at each iteration to get the ideal control points $\mathbf{P}^*$. Because the data has a huge amount of points, in each iteration, the KD-tree method [Vedaldi and Fulkerson, 2010] is adopted to calculate the matrix $\Delta_{\mathbf{X}}^{(n)}$ saving the distances between the superellipsoid points and the most adjacent data point. Then, using Eq. (3.5), the displacements $\Delta_{\mathbf{P}}^{(n)}$ can be calculated. With the displacements and Eq. (3.4), the new control points $\mathbf{P}^{(n+1)}$ can be obtained coupled with model points $\mathbf{X}^{(n+1)}$. The stopping criterion ϵ is set as the norm of the difference between $\mathbf{X}^{(n+1)}$ and $\mathbf{X}^{(n)}$. ϵ is selected empirically from the visual effect and it is depending on the applications. Finally, the output will be the relative ideal control points $\mathbf{P}^*$ and ideal model points $\mathbf{X}^*$.

For a better demonstration of the displacements of the control points and inferring quantitative information on the deformation, the Singular Value Decomposition (SVD) method [Van Loan, 1976, Bardinet et al., 1998] is introduced as a regularization into the FFD procedure because of its easiness of operation. When calculating the Moore-Penrose inverse matrix $\mathbf{B}^\dagger$, it is necessary to calculate the SVD of matrix $\mathbf{B}$ with:

$$\mathbf{B} = \mathbf{U} \cdot \mathbf{W} \cdot \mathbf{V}^T, \tag{3.7}$$

where $\mathbf{U}$ and $\mathbf{V}$ are orthogonal matrices, and $\mathbf{W}$ is diagonal with the diagonal elements being the singular value of $\mathbf{B}$. And then, $\mathbf{B}^\dagger$ is calculated by:

$$\mathbf{B}^\dagger = \mathbf{V} \cdot \mathbf{W}^{-1} \cdot \mathbf{U}^T. \tag{3.8}$$

By only using the largest singular value in $\mathbf{W}$, it is possible to control the norm of Eq. (3.6) to operate the regularization.

Therefore, by combining the 8 parameters of the superellipsoid p_8 and a set of control points $\mathbf{P}^*$, the shape in the low-resolution model can be described.

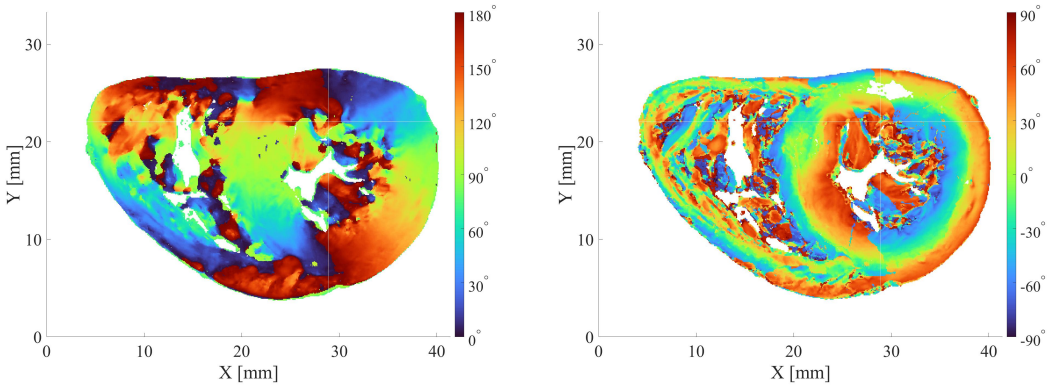

(a) (b)

Figure 3.2: *Sections of PLI data that show (a) azimuth angle and (b) elevation angle.*

3.3 Low-resolution surface model

3.3.1 Polarized light imaging data

Polarized Light Imaging (PLI) is a contrast-enhancing technique that improves the quality of the image obtained with birefringent materials [Carlton, 2011]. It allows extracting the voxel principal orientation, which is the mean orientation of all cardiomyocytes contained in a voxel with a resolution of $90 \times 90 \times 500$ µm. The orientation information is expressed by two angles: the azimuth angle $[0°, 180°]$ and the elevation angle $[-90°, 90°]$ [Jouk et al., 2018].

Because the resolution of PLI data approximates the resolution of the proposed low-resolution model and contains the orientation information of tissue, I adopt PLI data as the data source in the simulations of the low-resolution model. Benefitting from the work of Pierre-Simon Jouk, Gabrielle Michalowicz and Yves Usson(in Equipe DyCTim, Laboratoire TIMC-IMAG), I obtained a set of PLI data with a size of 42.3 mm $\times$ 28.6 mm $\times$ 17 mm. Fig. 3.2 shows one section of azimuth and elevation volumes in PLI data along the z axis [Jouk et al., 2018]. This dataset contains the two ventricles. The outside borders are the epicardium, and the inside ones are the endocardium of the ventricles.

3.3.2 Surface model data-fitting

The first step of the simulations consists of the extraction of the epicardium and the endocardium. Since the PLI data contains a part of the myocardium from the apex to the valvule position, the partial epicardium is the part surrounding the ventricles. I extract the borders of each layer of the PLI data to get the surface of the partial epicardium and the LV endocardium. Then, I elongate them along the z axis to have an isotropic resolution along each axis of 90 µm. The homogeneous partial epicardium and LV endocardium surface are shown in Fig. 3.3a and Fig. 3.4a, respectively.

Taking the partial epicardium as the first set of shapes, using the previously described method in section 3.2.2, I build the superellipsoid models and get the p_8 for them, summarized in Tab. 3.1.

Since the epicardium in the PLI data is partial with an open surface, the top part of the superellipsoid is removed. A $5 \times 5 \times 5$ grid of control points is defined and used with the procedure described in Algorithm 1 that operates the FFD. The stopping standard for iteration, ϵ, is set as 10 here. The superellipsoid model with the data points of partial epicardium is displayed in Fig. 3.3c. Fig. 3.3d contrasts the partial epicardium surface data points and the resulting model points. It shows that most of the points are highly fitted, which validates that the proposed methodology can simulate the shape of the partial epicardium. As shown in Fig. 3.3e, I calculate the distances between the data points and their corresponding result model points. It shows that, only at the apex part, a few points have not been well fitted to the data. In most parts of the volume, the errors are near 0 µm. The maximum and minimum values of the errors are summarised in Table. 3.2.

Similarly, the LV endocardium results are shown in Fig. 3.4. The results are close to the partial epicardium, while the distances in Fig. 3.4e show the model has fitted to the data in most of the areas, except that around the apex part which has a relatively high shift. The maximum and minimum values of the errors are summarised in Table. 3.2.

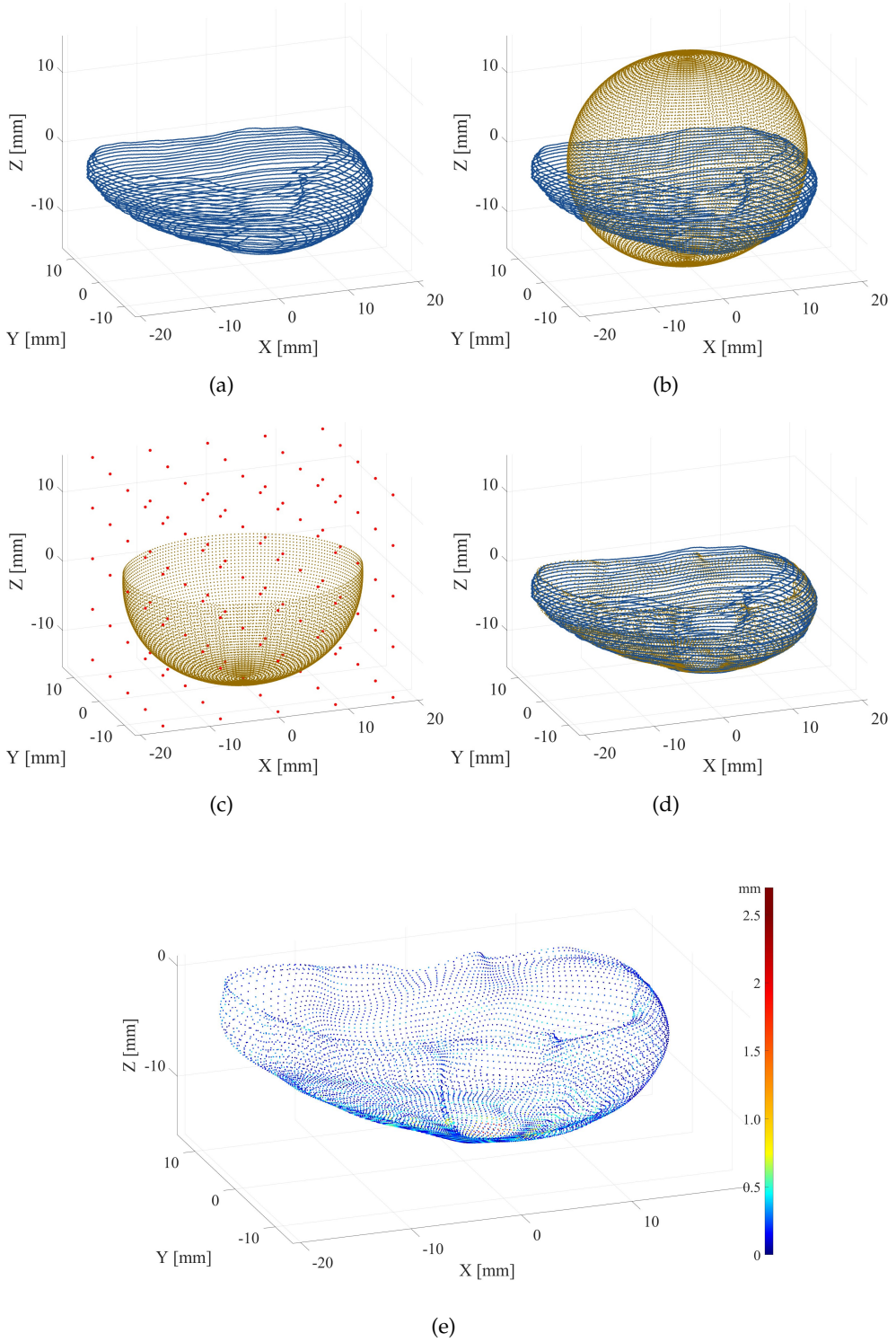

Figure 3.3: *Simulation of the partial epicardium. (a) Partial epicardium surface. (b) Superellipsoid. (c) Truncated superellipsoid with control points. (d) Contrast between the partial epicardium surface (blue points) and the simulation (brown points). (e) Error between each pair of data points and model points.*

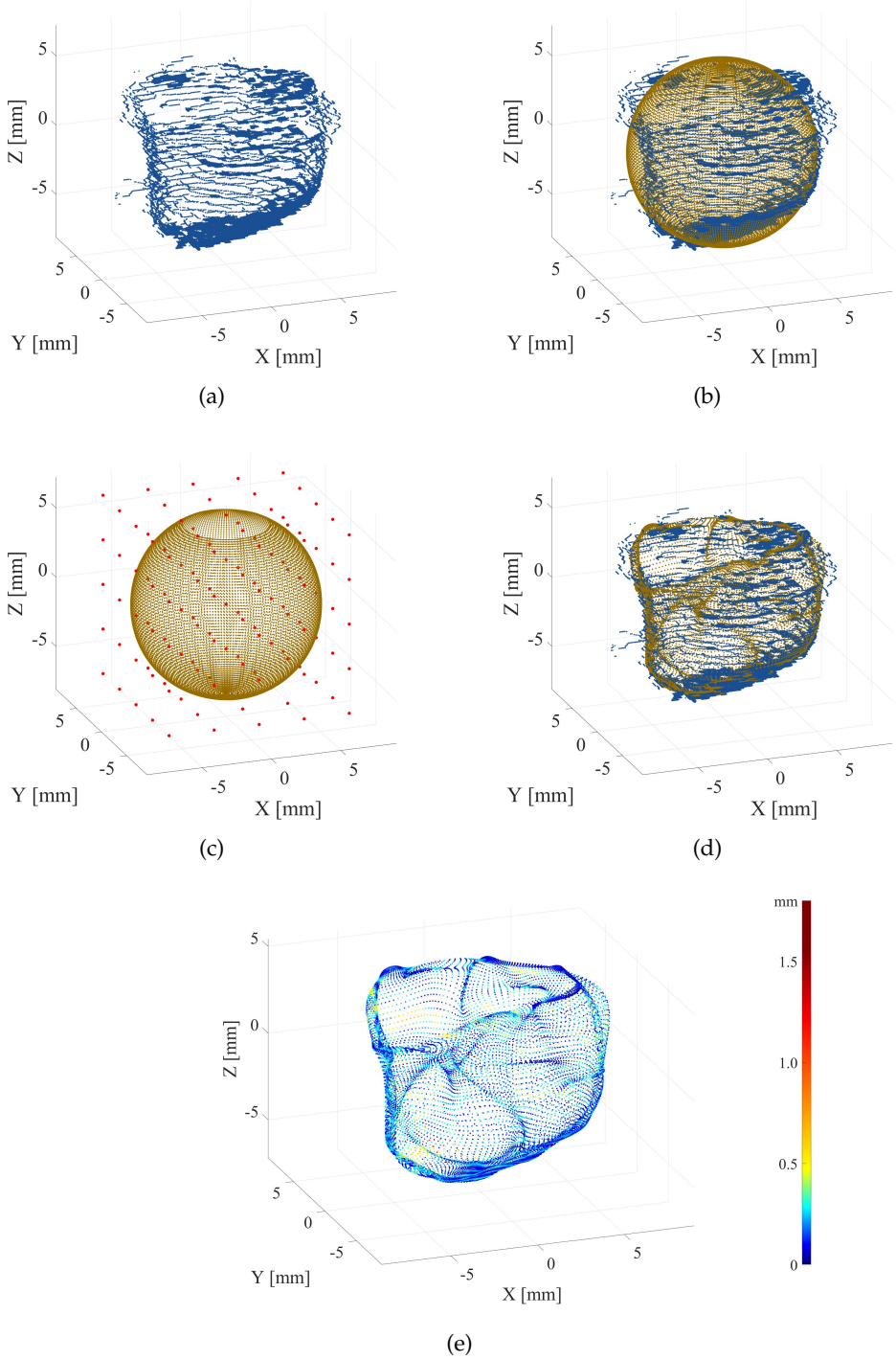

Figure 3.4: *Simulation of the LV endocardium. (a) LV endocardium surface. (b) Superellipsoid. (c) Truncated superellipsoid with control points. (d) Contrast between the LV endocardium surface (blue points) and the simulation (brown points). (e) Error between each pair of data points and model points.*

Table 3.1: *p_8 of the superellipsoid models*

p_8	a_1	a_2	a_3	ε_1	ε_2	t_x	t_y	t_z
Partial Epicardium	184.22	154.72	162.40	0.96	1.02	248.67	188.01	165.07
LV Endocardium	72.23	72.79	71.55	0.98	1.03	320.76	192.10	84.44

Table 3.2: *Errors of the superellipsoid models*

	Max Error (mm)	Mean Error (mm)
Partial Epicardium	2.51	0.24
LV Endocardium	1.58	0.17

3.4 Low-resolution volume model

The myocardium is situated between the epicardium, the outermost protective layer of the heart, and the endocardium, the innermost layer lining the chambers. Provided that I have got the geometric model for the partial epicardium and LV endocardium and the PLI data are volumetric data, the same strategy stated in section 3.2 can be utilized in building the geometric model on the myocardium. Besides that, volume registration can also be operated using a reverse procedure.

3.4.1 Volume model data-fitting

As the procedure of building the surface model, I start with an initial volumetric shape. Since the p_8 of the partial epicardium and LV endocardium are known, the initial myocardium shape of the ventricles can be generated by using the two superellipsoids as borders. According to several references about the anatomy of the heart [Torrent-Guasp et al., 2005, Kocica et al., 2006, Ho, 2009, Whiteman et al., 2021] and sections of PLI data in Fig. 3.2, a schematic section of two ventricles can be an ellipse with the septum inside curing to the RV side, as shown in Fig. 3.5.

I adopt the elevation angle volume in the PLI data as a data resource with only the shape of the data being used, as shown in Fig. 3.6a. Fig. 3.6b shows the initial model volume whose section is shown in Fig. 3.6c. The red outer line of the section is generated using the p_8 of the partial epicardium in Tab. 3.1 while the red inner line is generated

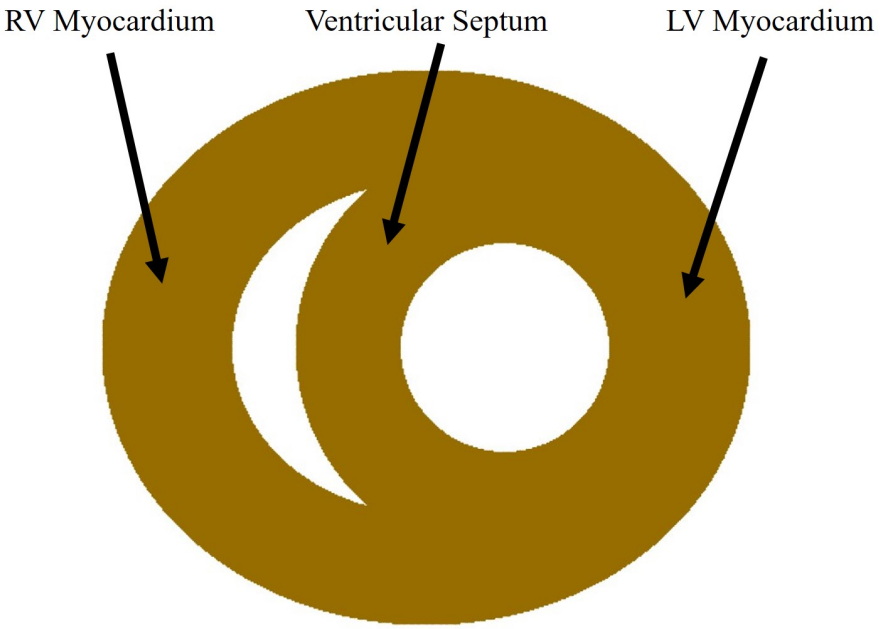

Figure 3.5: *Schematic section of the two ventricles.*

using the p_8 of the LV endocardium. The free wall of the myocardium is generated by shrinking the outer line and the septum is generated by enlarging the inner line. Then, taking the same method in Algorithm. 1, FFD ca be performed on the initial model volume to fit the data. The result shown in Fig. 3.6d can schematically describe the ventricular myocardium.

3.4.2 Volume registration

During FFD, the same transformation matrix is used for deformations of the volumes by the displacements of the control points. It is possible to deform the model volume to the data which means that by displacing back the control points it is possible to deform the data to the model volume. Then, different sets of data can be deformed to the same model volume, which is a registration.

Since it is possible to operate this bidirectional deformation on the geometric shapes of the data and the model volume, the information in the data, such as the azimuth angle and elevation angles of each point, can be transferred into the model volume as well. Therefore, a uniform model volume can be used to build this relationship between it and

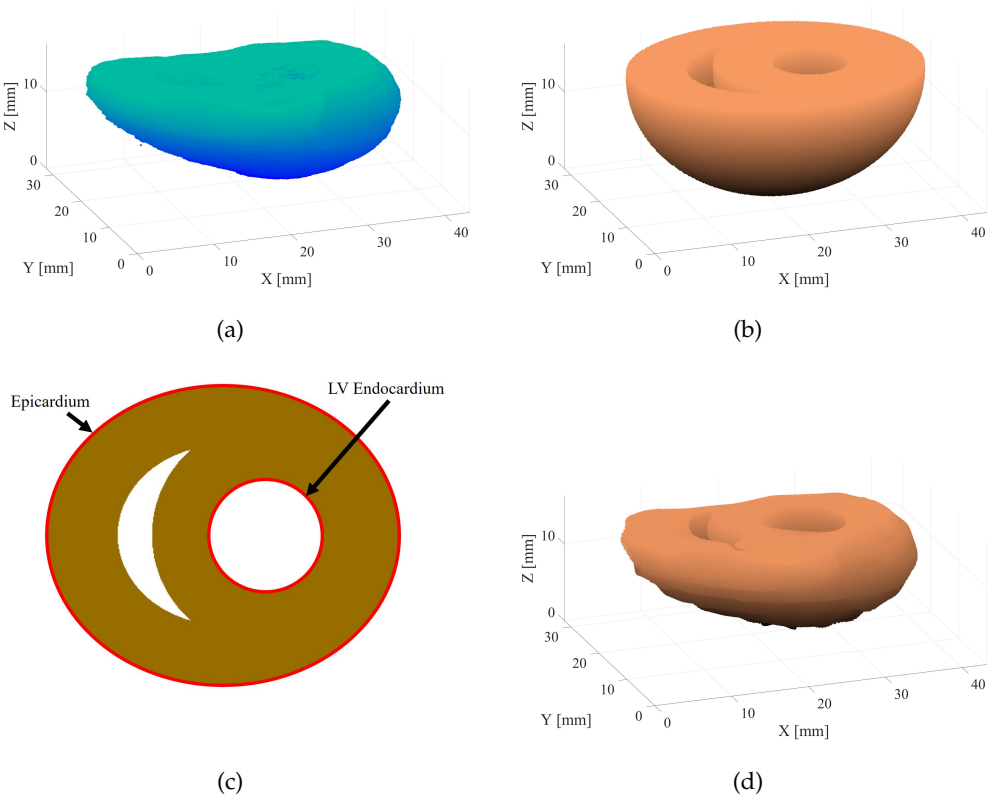

Figure 3.6: *Low-resolution volume model data-fitting. (a) Ventricular myocardium from PLI data. (b) Model volume. (c) A section of the model volume. (d) Virtual ventricular myocardium after FFD.*

various datasets, which means individual medical information about the myocardium can be compared on the same uniform model volume.

Fig. 3.7a and Fig. 3.7b show the azimuth angle and elevation angle in the PLI data, respectively. Using the method in section 3.4.1, and the backwards procedure stated above, I generated the model volume as in Fig. 3.7c and Fig. 3.7d and transferred the angles into the model volume. From the results, there are similarities between the PLI data and the uniform model volume.

For more detailed comparisons, I extracted sections of the PLI azimuth and elevation volume along the longitudinal axis and the sections in the model volumes at top, middle and bottom part the ventricular myocardium, as shown in Fig. 3.8c and Fig. 3.8d, Fig. 3.9c and Fig. 3.9d, and Fig. 3.10c and Fig. 3.10d, respectively. There are some similarities between each pair of them, but it exists some "stairstep" shape in some areas, as shown in the red ROI, because the centre of each layer of PLI data along the z axis is not situated on the same vertical line. This causes a shift between the centre of the data and the centre of the uniform model at each layer, which leads to a data loss in the uniform volume.

To fix that problem, a layer-by-layer way is employed along the z axis to operate the FFD. On each layer of the data along the z axis, the centre of the data is calculated and shifted to the centre of the uniform model in order to eliminate the "stairstep" shapes. The sections extracted from the PLI data and the registered results are shown in Fig. 3.8e and Fig. 3.8f, Fig. 3.9e and Fig. 3.9f, and Fig. 3.10e and Fig. 3.10f, which are situated at the top, middle and bottom parts of the ventricular myocardium, respectively. There are some radial stripes at the border which is normal because of the difference in the amount of points between the data and the uniform model. However, since the centres of the PLI data and the uniform volume have registered at each layer, the data points are better conserved than the way of direct volume registration.

3.5 Conclusion

This chapter introduces the low-resolution of my multiscale model. The low-resolution model focus on Level 1 in Fig. 2.1 including mainly the myocardium and related surfaces. It is based on a superellipsoid model coupled with FFD to adjust it to a real shape. The

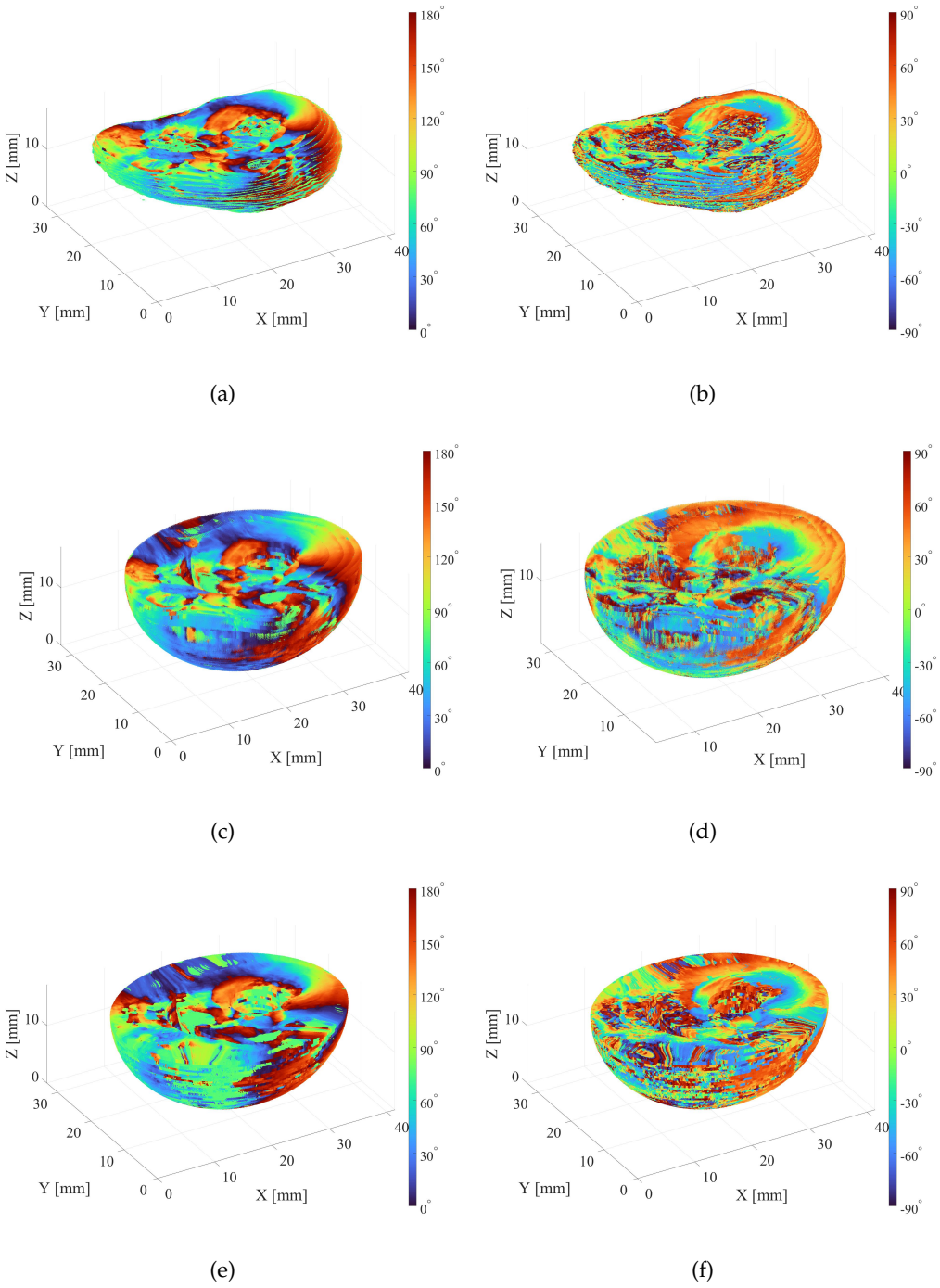

Figure 3.7: *Volume registration. (a) Azimuth and (b) elevation angle volume in PLI data. uniform model volume carrying the (c) azimuth and (d) elevation angle. Uniform model volume carrying the (e) azimuth and (f) elevation angle using a layer-by-layer method.*

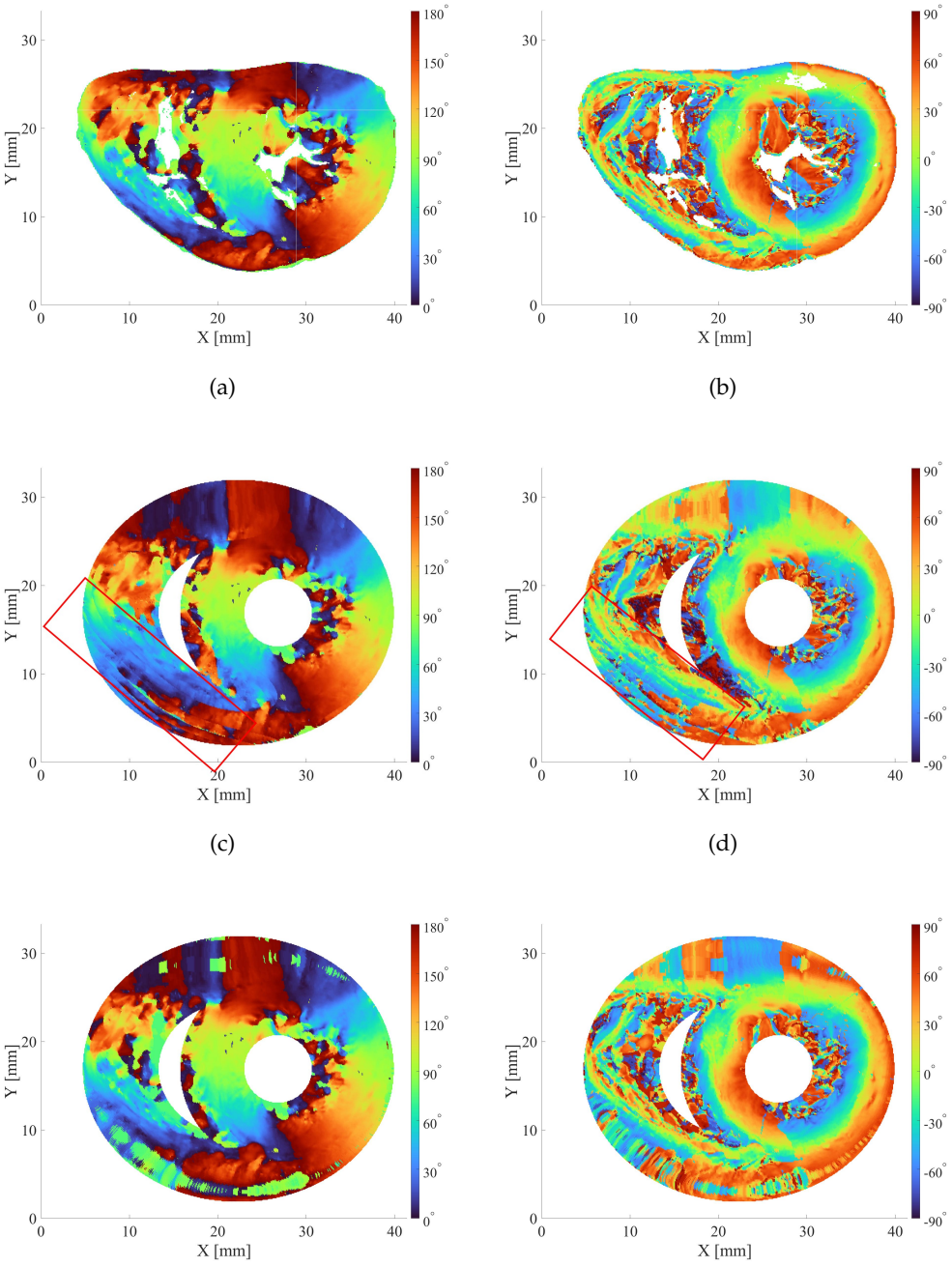

Figure 3.8: *Sections at the top part of the ventricular myocardium in the PLI data and the registration volumes. Sections of (a) azimuth angle volume and (b) elevation angle volume in PLI data. Sections of (c) azimuth angle volume and (d) elevation angle volume in uniform model with the "stairstep" shapes. Sections of (c) azimuth angle volume and (d) elevation angle volume in uniform model using a the layer-by-layer method.*

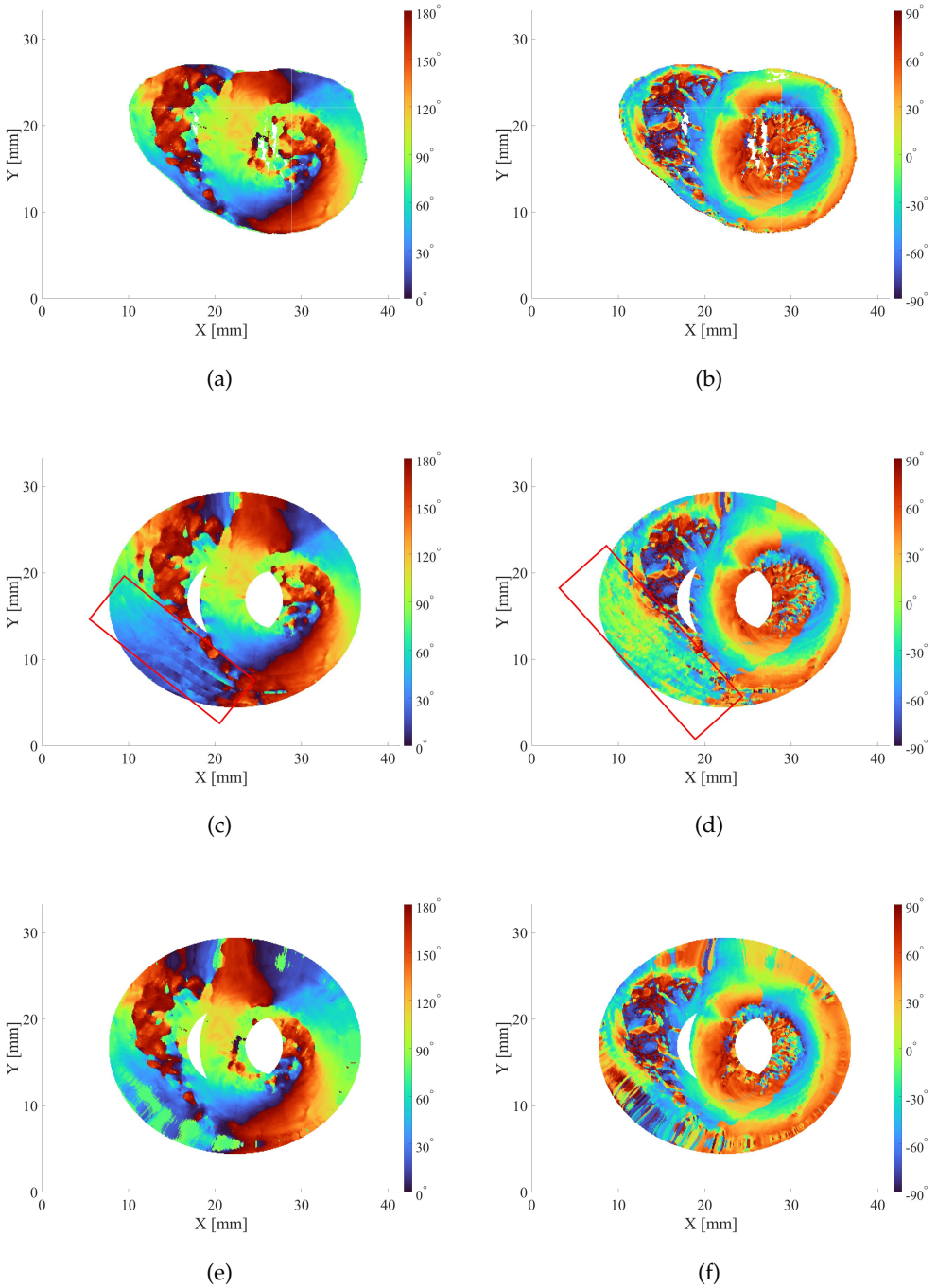

Figure 3.9: *Sections at the middle part of the ventricular myocardium in the PLI data and the registration volumes. Sections of (a) azimuth angle volume and (b) elevation angle volume in PLI data. Sections of (c) azimuth angle volume and (d) elevation angle volume in uniform model with the "stairstep" shapes. Sections of (c) azimuth angle volume and (d) elevation angle volume in uniform model using a the layer-by-layer method.*

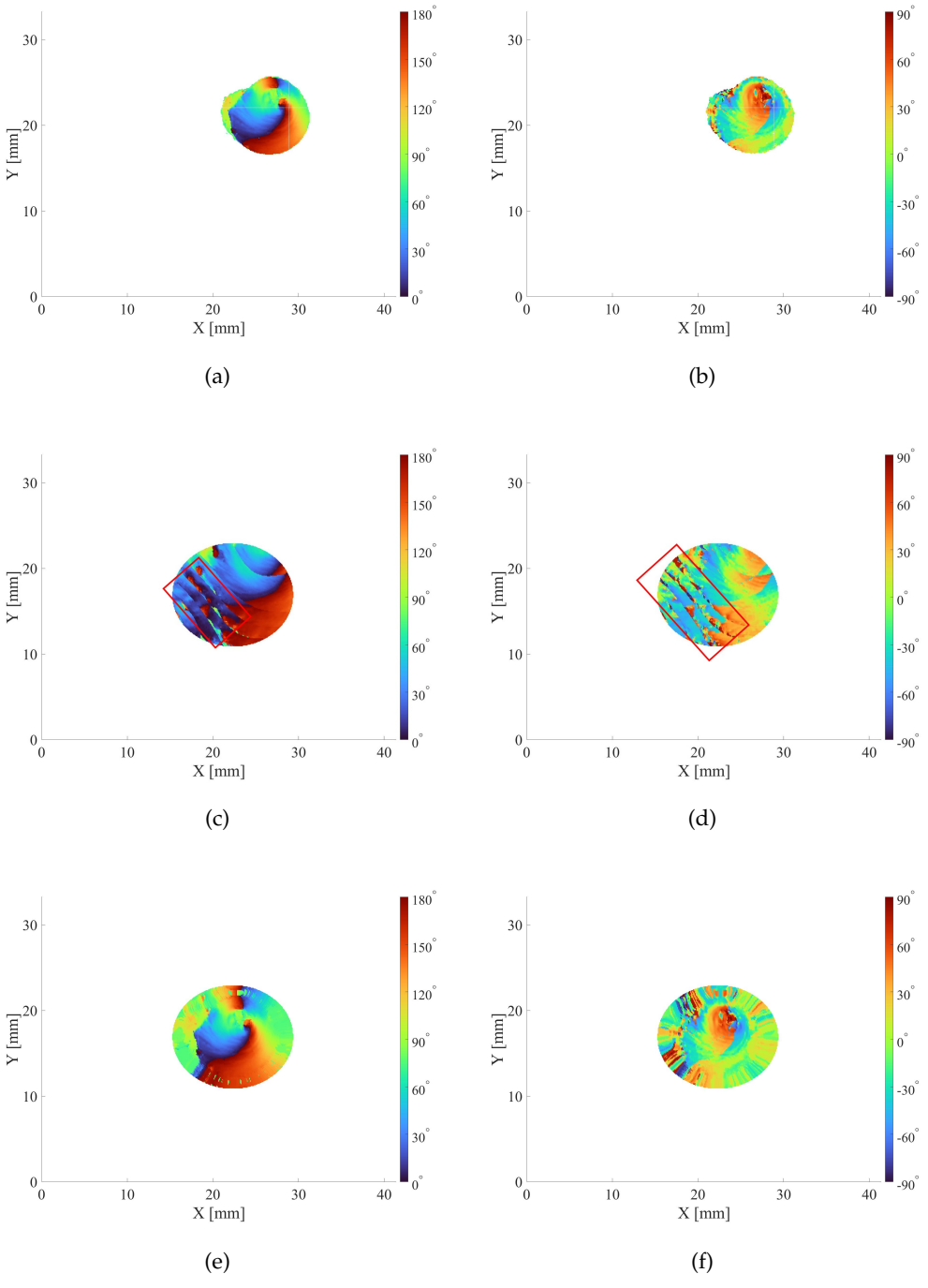

Figure 3.10: *Sections at the middle part of the ventricular myocardium in the PLI data and the registration volumes. Sections of (a) azimuth angle volume and (b) elevation angle volume in PLI data. Sections of (c) azimuth angle volume and (d) elevation angle volume in uniform model with the "stairstep" shapes. Sections of (c) azimuth angle volume and (d) elevation angle volume in uniform model using a the layer-by-layer method.*

superellipsoid model is used in the coarse data-fitting part in which I got eight parameters p_8 for building this model, including three radii of the superellipsoid along x, y, and z axis, two exponent parameters controlling squareness of the longitudinal and latitudinal plane, and three translation parameters. Then, FFD is used in the fine data-fitting part to refine the effect in which I get a grid of control points that deform the superellipsoid into an ideal result surface. Therefore, my low-resolution model is composed of a set of 8 parameters p_8 and a grid of control points $\mathbf{P}^*$ which is used to simulate the geometric shapes of myocardial surfaces.

By means of the low-resolution surface model, simulations of a partial epicardium and LV endocardium are operated using the PLI data because the PLI data has a similar resolution to our low-resolution model. Between the epicardium, the outermost layer, and the endocardium, the innermost layer, the low-resolution volume model has been built, and the virtual ventricular myocardium is generated. The results show that my low-resolution model has the ability to reasonably simulate the surfaces, the partial epicardium and LV endocardium and the volume, ventricular myocardium at Level 1, with acceptable low errors.

Through FFD, the bidirectional deformation of the geometric shapes of the data and the model volume can be operated. Thus, using the inverse procedure, volume registrations are carried out, transferring the information of real data into a uniform model volume that qualitatively describes the data. The volume registration between the azimuth and elevation angle volume in PLI data and the uniform model volume has been performed. However, direct registration between the volumes will generate "stairstep" shapes in some areas of the model, so a layer-by-layer way is employed to fulfil the registration. The results show that the uniform model can quantitatively describe the azimuth and elevation angle information from the PLI data. Therefore, comparisons of myocardial information from various individuals can be accomplished on this uniform volume.

Chapter 4

High-resolution model

Contents

4.1 Introduction

After building the low-resolution model at Level 1, I continue to generate the high-resolution geometric model of elementary objects at Levels 2, 3, and 4. The relationship among the various elementary objects in the heart depends on the multiscale structure as shown in Fig. 2.1. Meanwhile, the shapes and sizes of the objects are inspired by the observation of human cardiac tissue data, as stated above in Chapter 1. In my multi-scale cardiac tissue model, the cardiomyocyte is considered the basic functional object. The shape of each cardiomyocyte is represented by a cylinder. From histological studies [LeGrice et al., 2001] and synchrotron data observation [Mirea, 2017, Varray et al., 2017, Wang et al., 2019] it is known that, in the myocardium, several cardiomyocytes are organised in a "bundle" containing a limited number of cardiomyocytes with a layer of perimysium constraining it and a capillary in the centre. I define the "bundle" as a geometric object containing a limited series of cardiomyocytes while its general shape is also a cylinder. From the definition of the sheetlet in section 1.2.2.1, generally, the sheetlet module contains several cleavage planes and cardiomyocyte bundles between them.

In this chapter, I simulate the basic geometric shapes of the cardiomyocyte module, the cardiomyocyte bundle module and the sheetlet module. In the cardiomyocyte bundle module, using FFD, I deform the basic shape to simulate the twisting structure of the real shape and the shape variation during the cardiac cycle. In the sheetlet module, the basic shape is also deformed to simulate the real curved structure.

4.2 Cardiomyocyte module

The high-resolution model starts with the cardiomyocyte at Level 4, as it is the basic functional tissue unit in my multiscale model. As shown in Fig. 4.1, the cardiomyocyte is not isolated. It always exists with an endomysium surrounding it and an intercalated disc for connections between cardiomyocytes. Thus, a cardiomyocyte module including these three parts is simulated at Level 4. When describing the geometric shapes, a static cardiomyocyte is considered simply as a cylinder with a section of an ellipse, while the endomysium is considered as the side surface of the cylinder, and the intercalated disc is

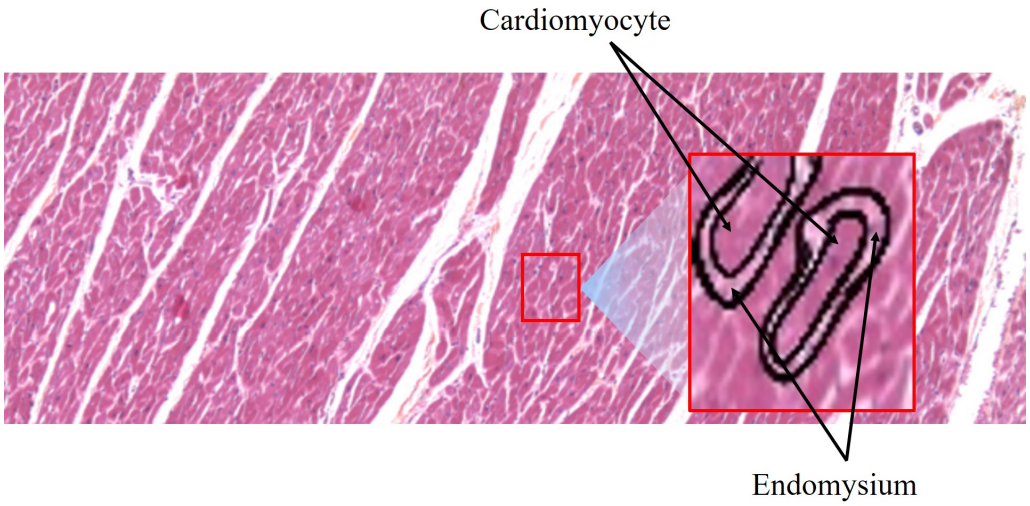

Figure 4.1: *Histological image of cardiac tissue with a Region Of Interest (ROI) of cardiomyocytes and endomysium.*

considered as an elliptic disc for end-to-end cardiomyocytes' connection along their long side.

In the simulation of a static cardiomyocyte, the geometric parameters of the cylinder are defined according to [Dejea et al., 2017]. The length of the cylinder is set to $L_{mc} = 100$ µm. The semi-major axis of the elliptic section, R_x, is set to 18 µm and the semi-minor axis, R_y, is set to 9 µm. I create a 3D voxel-based model for cardiomyocytes with a resolution of 0.25 µm/voxel. Inside a cardiomyocyte module, each part can be processed separately and combined afterwards to compose a complete basic functional unit. The generated shapes of them are shown in Fig. 4.2.

4.3 Cardiomyocyte bundle module

4.3.1 Basic shape

Several cardiomyocytes usually unite around a capillary with the perimysium surrounding them to make a cardiomyocyte bundle, as shown in Fig. 4.3. In its simulation, the geometric shape of a cardiomyocyte bundle module is also regarded as a cylinder composed of a bundle with six cardiomyocytes, one capillary inside, and the perimysium around the bundle.

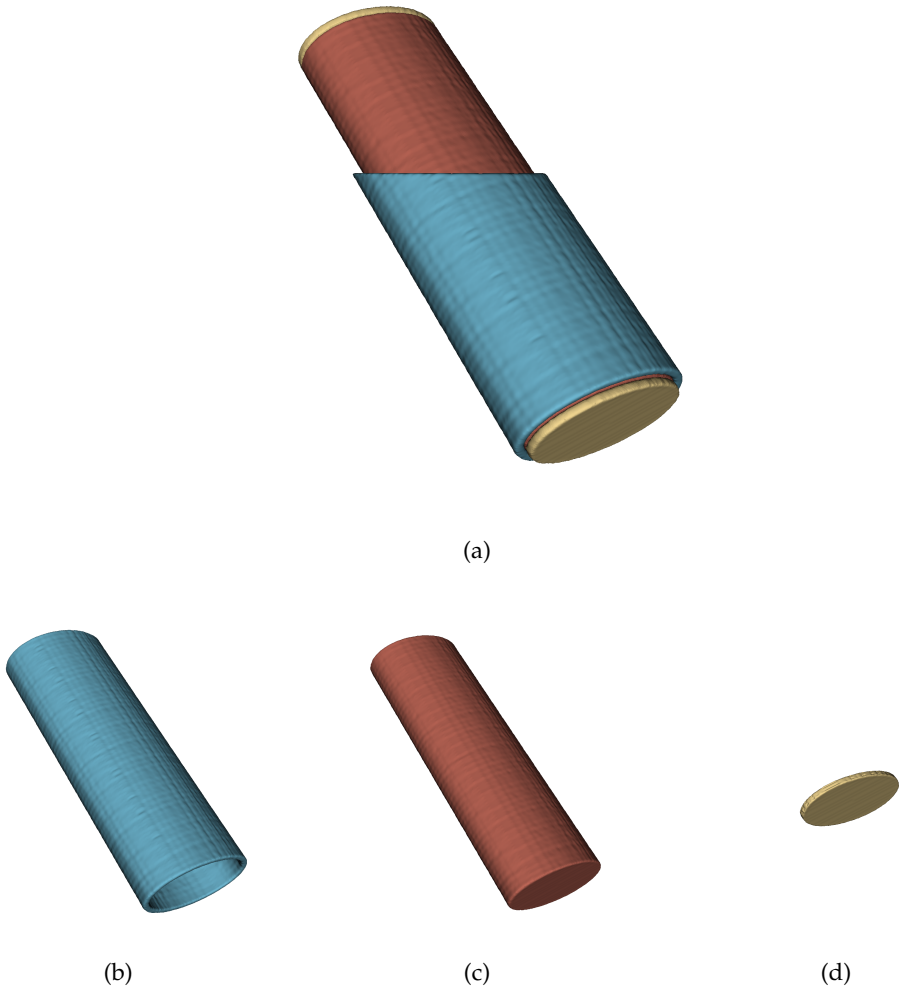

(a)

(b) (c) (d)

Figure 4.2: *Virtual cardiomyocyte in the ECM: (a) Cardiomyocyte module. (b) Endomysium. (c) Cardiomyocyte. (d) Intercalated disc.*

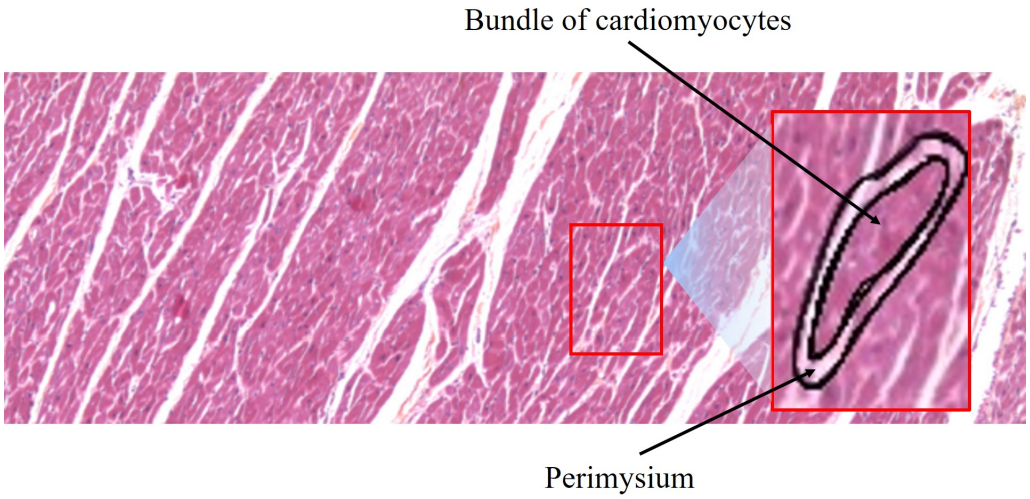

Figure 4.3: *Histological image of cardiac tissue with ROI of a cardiomyocyte bundle.*

I adopt the idea of distance transform [Breu et al., 1995] and the watershed algorithm [Bieniek and Moga, 2000] to design the compact arrangement of the cardiomyocytes and the capillary on the section of the bundle. As shown in Fig. 4.4a, six points representing the six cardiomyocytes' centres and one point representing the capillary centre are first generated. For compact arrangement, they are situated at the vertex and the centre of a hexagon. Then, a distance transform is operated to calculate the distance between each pixel and its nearest centre, as shown in Fig. 4.4b. After that, I employed the watershed algorithm to segment the seven areas, as shown in Fig. 4.4c. Last, an erosion with a disc structure element is used to get a compact arrangement of the six cardiomyocytes and the capillary, as shown in Fig. 4.4d.

Using the section in Fig. 4.4d, I generated a 3D image with a resolution of 0.25 µm/pixel in each direction and a basic shape of a cardiomyocyte bundle module inside, which is a cylinder. The radius of this cylinder, R_b, is set to 30 µm and its length, L_b, is set to 180 µm. The results are shown in Fig. 4.5.

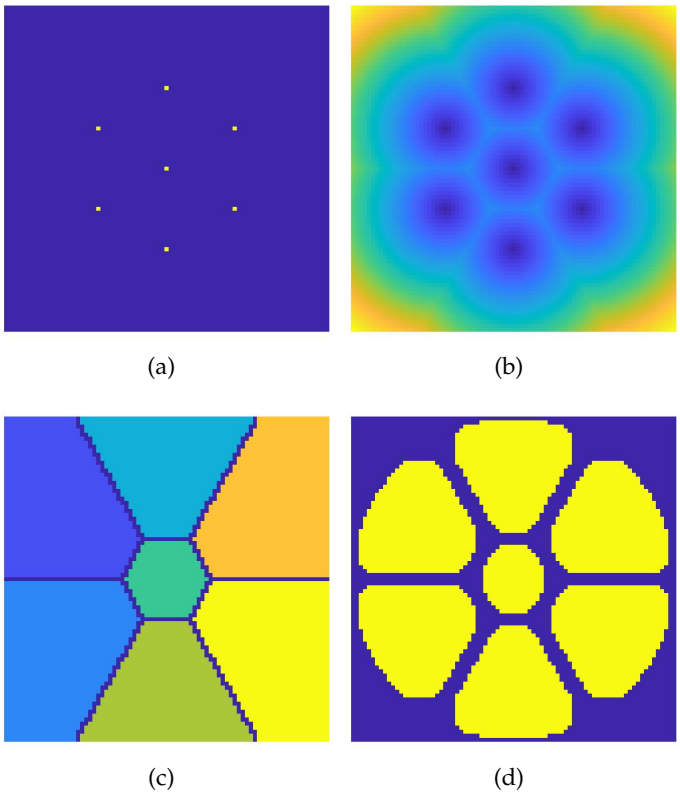

Figure 4.4: *Section generation of a virtual cardiomyocyte bundle. (a) Centres of the six cardiomyocytes and a capillary. (b) Distance field generated according to (a). (c) Area division by watershed algorithm. (d) Final section.*

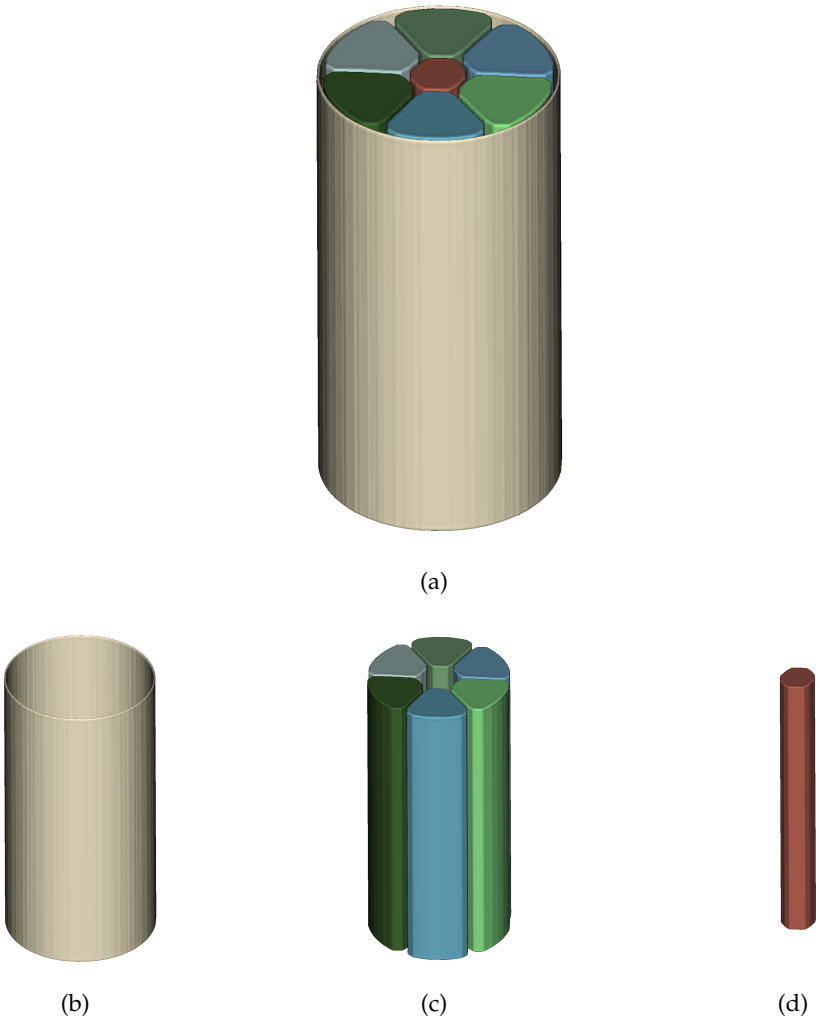

(a) (b) (c) (d)

Figure 4.5: *Virtual cardiomyocyte bundle in the ECM. (a) cardiomyocyte bundle module. (b) Perimysium. (c) 6 cardiomyocytes. (d) Capillary.*

4.3.2 FFD on the cardiomyocyte bundle

4.3.2.1 Refinement of the basic shape of the cardiomyocyte bundle

The shape of a cardiomyocyte bundle in a biological tissue could be compared to a "rugby" ball truncated with a thinner section at its extremities. To build such a real cardiomyocyte bundle, I use the cylinder in Fig. 4.5a as an initial shape and define a morphing transform to go from this initial shape to the final objective ellipsoidal shape [Wang et al., 2020].

The initial shape to simulate an object of the cardiomyocyte bundle which is a cylinder in Fig. 4.5a with a radius of $R_b > 0$ and length of $L_b > 0$, is defined by:

$$\frac{x^2}{R_b^2} + \frac{y^2}{R_b^2} < 1, \quad |z| < \frac{L_b}{2}. \tag{4.1}$$

From a histological view, the objective shape of a cardiomyocyte bundle is supposed to be a truncated ellipsoid, where the original equation of the ellipsoid is defined by:

$$\frac{x^2}{\left(R_x\right)^2} + \frac{y^2}{\left(R_y\right)^2} + \frac{z^2}{\left(R_z\right)^2} < 1 \tag{4.2}$$

with the circular section of the cylinder lying parallel to the (x,y) plane and the height in the z direction, where $R_x > 0$, $R_y > 0$, and $R_z > 0$ are the radius along x, y, and z directions, respectively. Given this structure, I decide to deform the initial cylinder layer by layer along the z direction. This strategy allows precise control of the parameters of the output truncated ellipsoid. Therefore, the deformation of one layer of height z can be defined as from a circle with a radius of R_b towards an ellipse of an equation:

$$\frac{x^2}{R_x^2} + \frac{y^2}{R_y^2} = 1 - \frac{z^2}{R_z^2}. \tag{4.3}$$

this equation can be rewritten as:

$$\frac{x^2}{\left(R_x c\right)^2} + \frac{y^2}{\left(R_y c\right)^2} = 1 \tag{4.4}$$

where $c = \sqrt{1 - z^2/R_z^2}$ is the weighting coefficient of the radius along the x and y direc-

tions. It means that the radius of the layer of height z is c times the radius of the layer of height 0. Thus, the deformation weighting parameters q_x and q_y, which are used to modify the original radius of the circle as well as the coordinates of the control points along the x and y direction, can be calculated by:

$$q_x = \frac{R_x c}{R_b}, \quad q_y = \frac{R_y c}{R_b}. \tag{4.5}$$

In a real situation, besides the outline of the cardiomyocyte bundle being a truncated ellipsoid, the cardiomyocytes inside are shaped as twisted cylinders instead of simply paralleled cylinders. Thus, the shape of a cardiomyocyte bundle approximates a twisted noisy truncated ellipsoid for the compressional deformation during the cardiac cycle. I adapt my model to simulate this shape. Retaining a layer-by-layer process, I define a rotation on the control points to rotate each layer. The rotation degree, A_z, is a function of z and is defined as:

$$A_z = A_{rotation} \times z \tag{4.6}$$

where $A_{rotation}$ is an arbitrary angle varied between two consecutive layers.

I define a Gaussian noise model with the mean of (μ_x, μ_y) and standard deviation of (σ_x, σ_y) to perturb the location of each control point belonging to the layer $(x,y)_{cp}$. The noisy locations of the control point $(x,y)_{cpn}$ are given by:

$$(x,y)_{cpn} = (x,y)_{cp} + (G_x(\mu_x, \sigma_x), G_y(\mu_y, \sigma_y)) \tag{4.7}$$

where $G_x(\mu_x, \sigma_x)$ and $G_y(\mu_y, \sigma_y)$ are two independent Gaussian noise with mean value μ_x and μ_y, and standard deviation σ_x and σ_y, whose probability density function p_G is given by

$$p_G(s) = \frac{1}{\sigma\sqrt{2\pi}} e^{-\frac{1}{2}\left(\frac{s-\mu}{\sigma}\right)^2}. \tag{4.8}$$

Through the pipeline of FFD, as described above, a layer-by-layer strategy is imposed to deform the cylinder along the z direction. At each layer of the cylinder, I impose a grid of 7×7 control points and calculate the local coordinates of the control points. I

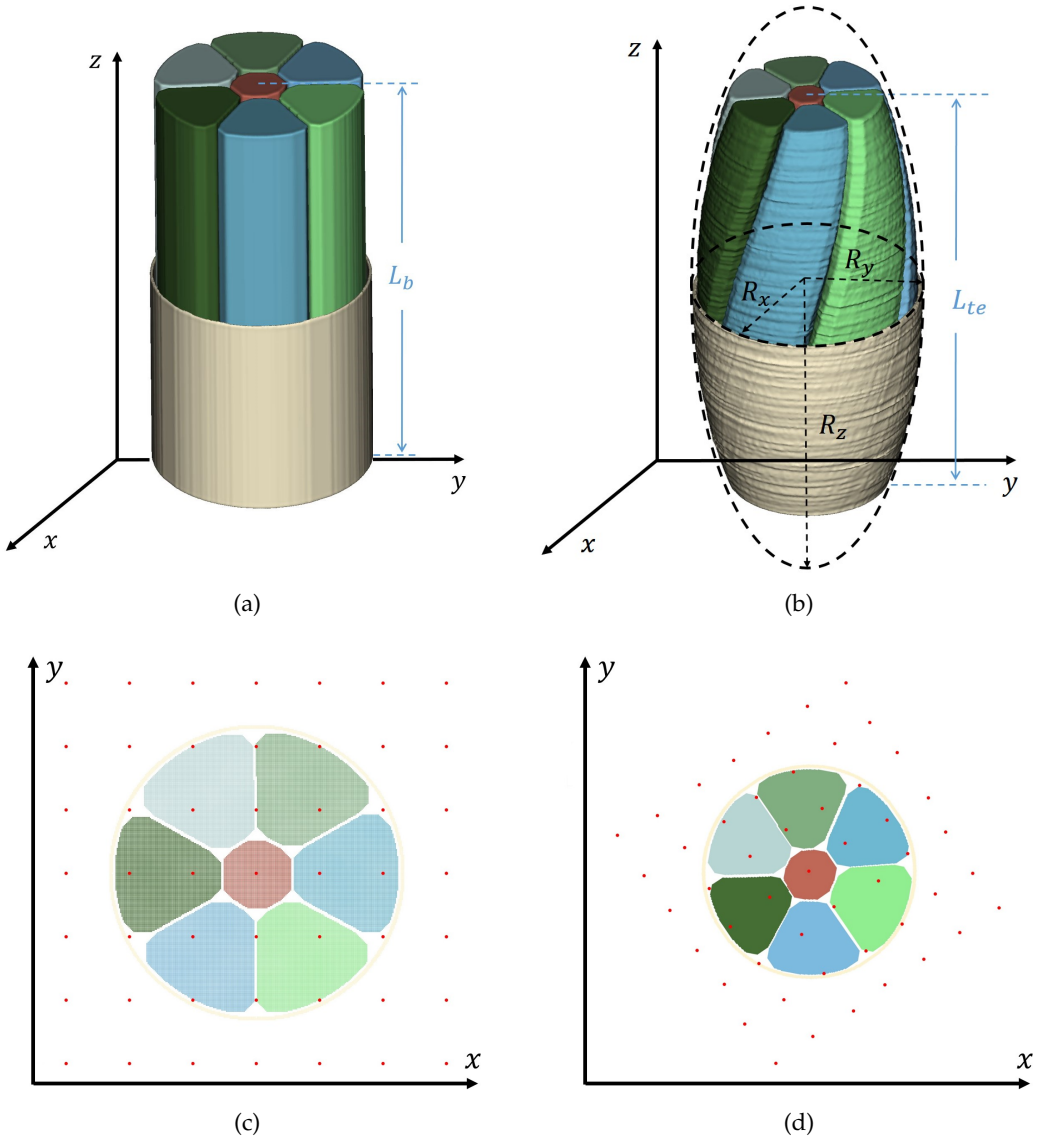

Figure 4.6: *Deformation from a bundle to a twisted truncated ellipsoid with noise. (a) Original bundle with 6 cardiomyocytes and 1 capillary. (b) Result of the deformation which is a twisted truncated ellipsoid with noise. (c) Initial 40th layer of the cylinder with the 7×7 control points. (d) Deformed 40th layer with the moved, rotated, and noisy control points.*

use the shape presented in Fig. 4.5a, as the initial shape with the same parameters. The objective shape, as explained above, is a truncated ellipsoid with a length of L_{te} radius of $R_x = R_y = 30$ µm, and $R_z = 87$ µm along x, y, and z direction, respectively. And after the truncation, the length of the objective shape along the z direction is $L_{te} = 168$ µm. I also add a rotation according to Eq. (4.6) and a Gaussian noise according to Eq. (4.8) on each layer of the bundle with $A_{rotation} = 0.15°/\mu m$, $\mu_x = 0$ µm, $\mu_y = 0$ µm, $\sigma_x = 3$ µm, and $\sigma_y = 3$ µm.

The results are shown in Fig. 4.6 which shows the contrast between the initial and final volume. From Fig. 4.6a and Fig. 4.6b, it is obvious that the bundle is deformed from a cylinder to an ellipsoid, and meanwhile, twisted and truncated at its two extremities. Fig. 4.6c and Fig. 4.6d show how the section at each layer is transformed and rotated to achieve the twist and ellipsoid shape in the 3D view. The control points in Fig. 4.6d are not on a regular grid because of the Gaussian noise I impose on the control points. the deformed volume has the expected shape and the FFD keeps the gaps that separate the cardiomyocytes and the capillary.

4.3.2.2 Dynamic cardiomyocyte bundle during the cardiac cycle

The tissue in the myocardium rearranges and deforms during the cardiac cycle. For simulating various states in the cardiac cycle, I generated dynamic sequences of a cardiomyocyte bundle. Before the simulation, I draw a qualitative curve of myocardial thickness variation inspired by [Ferreira et al., 2015], which is shown in Fig. 4.7a, which shows that the thickness of the myocardial wall increases during the systole and decreases during the diastole and a whole cardiac cycle is around 1000 ms. During the systole, the wall thickness increases by the range 35% to 40% and the lengths of cardiomyocytes decrease by about 15% [Wojciech et al., 2016]. I assumed that the radius of a bundle qualitatively varies according to the myocardial thickness. For simulation, I selected 9 time points during the cycle (t_1 to t_9 at around 0 ms, 62.5 ms, 125 ms, 187.5 ms, 250 ms, 313 ms, 375 ms, 485 ms, and 1000 ms, respectively). During the systole, the five time points (t_1 to t_5) divide the systole evenly. During the diastole, at the four time points (t_6 to t_9), the radius of a bundle (wall thickness) is equal to those from t_4 to t_1. I assumed that at the time points

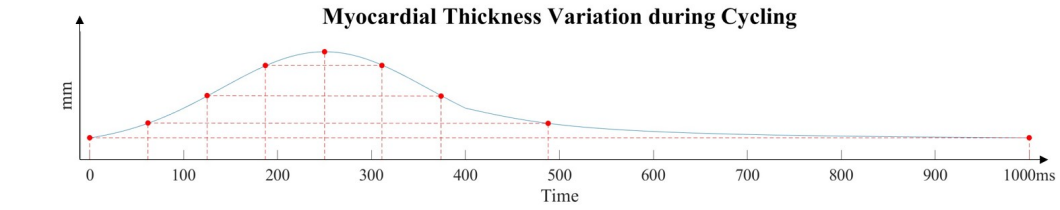

(a)

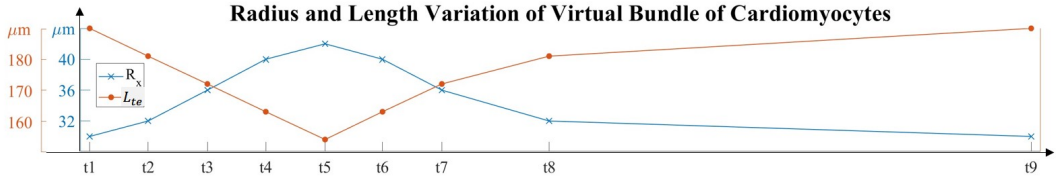

(b)

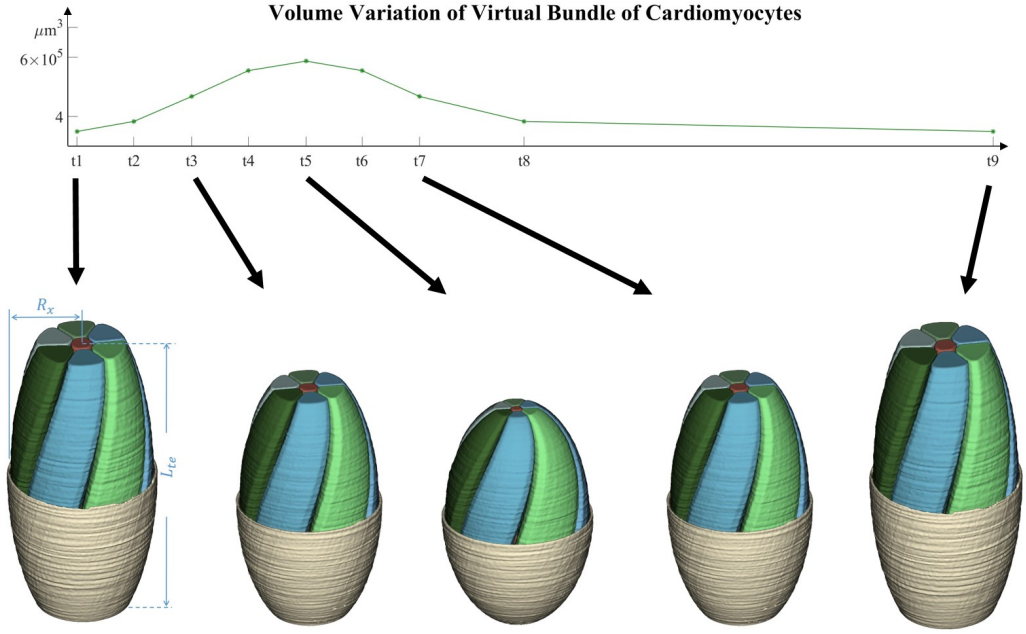

(c)

Figure 4.7: *Dynamic sequences of a cardiomyocyte bundle during the cardiac cycle. (a) Variation of the myocardial wall thickness inspired from [Ferreira et al., 2015]. (b) Variation of the radius and length of the bundle. (c) Variation of the total volume of the bundle and corresponding 3D rendering.*

with the same radius, the cardiomyocyte bundle has the same volume, which is accomplished by the volume control method in [Sederberg and Parry, 1986] and the length of the cardiomyocyte bundle varies linearly as shown in Fig. 4.7b and Fig. 4.7c. Therefore, I generated a cardiomyocyte bundle at these nine time points of the cardiac cycle. The radius of the equator plane R_x increases from 30 µm to 42 µm during systole and increases back to 32 µm during diastole and the length decreases from 180 µm to 153 µm during systole and increases back to 180 µm during diastole. Fig. 4.7c shows the simulations of cardiomyocyte bundle at selected time points t_1, t_3, t_5, t_7 and t_9. The results show that the volume change and the dimension of a bundle can be controlled during the cardiac cycle by FFD. In future research, given more quantitative geometric parameters of a bundle, such as the precise variation of the diameter, length and volume, the simulations during the cardiac cycle can be more accurate.

4.4 Sheetlet module

4.4.1 Basic shape

The myocardium is a complex structural hierarchy [LeGrice et al., 1997]. Laminar structures play essential roles in heart mechanics. As Fig. 4.8 shows, several adjacent cardiomyocytes organize together into layers (sheetlets) [Caulfield and Borg, 1979, Robinson et al., 1988]. At the same time, cleavage planes connect the sheetlets and enable the slippages of them. Thus, for simulations of the laminar structures, I simulate the sheetlet module composed of three layers of cleavage planes and two groups of cardiomyocyte bundles in between. I started by simulating cleavage planes as some parallel planes with thickness and then interposed several bundles between them, as shown in Fig. 4.9a. Between each pair of cleavage planes, each group of cardiomyocyte bundles has the same orientation.

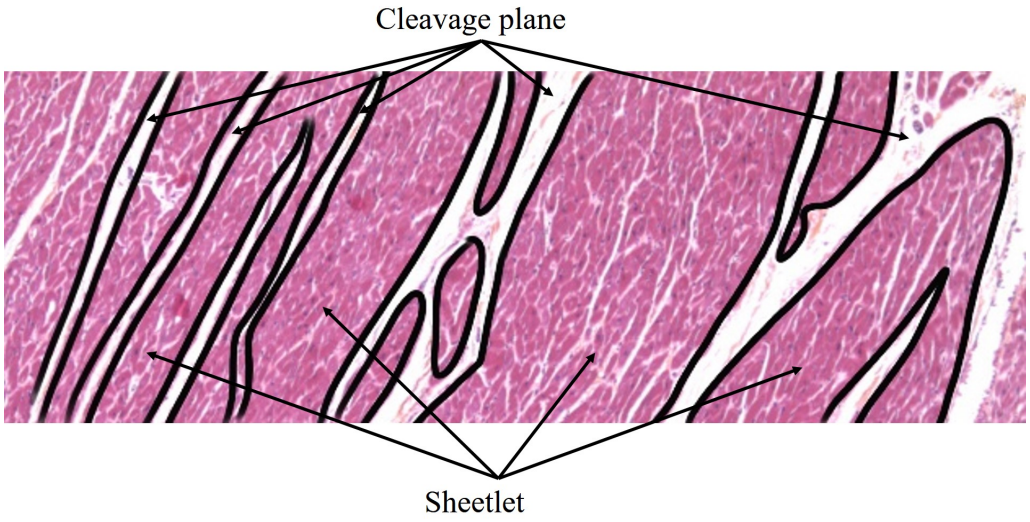

Figure 4.8: *Histological image of cardiac tissue with ROI of sheetlets and cleavage planes.*

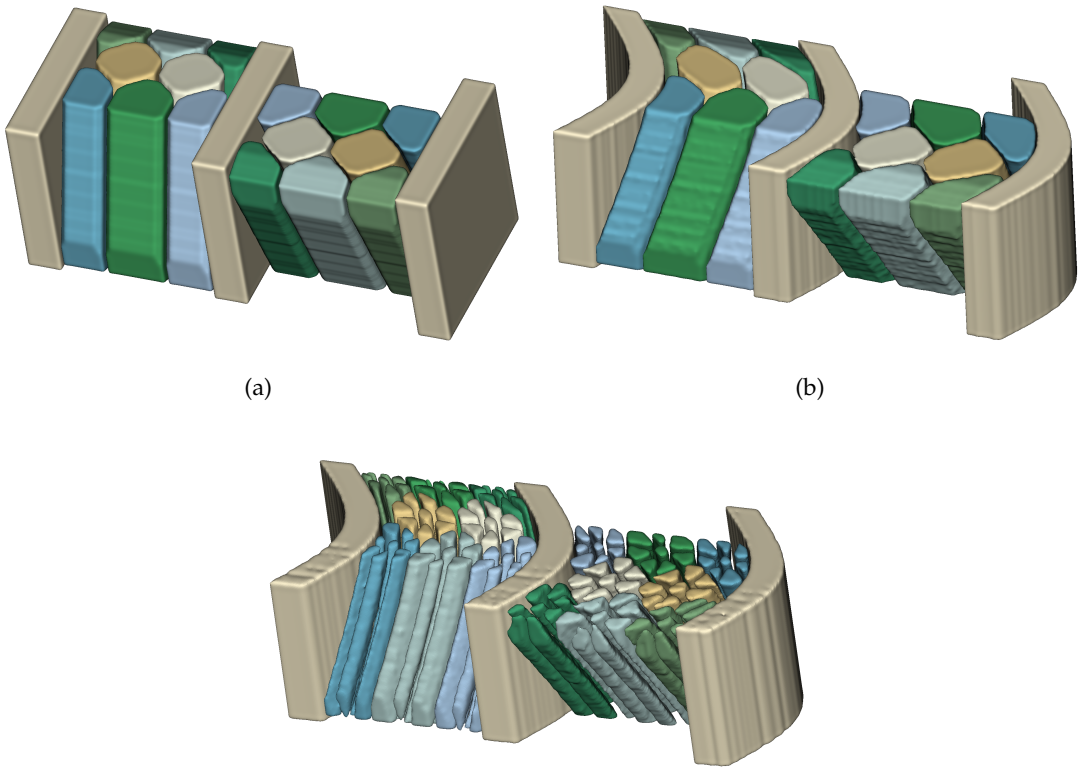

Figure 4.9: *Sheetlets and deformation: (a) original sheetlets with parallel laminar structure, (b) deformed sheetlets with curved laminar structure, and (c) deformed sheetlets embedded with cardiomyocytes.*

4.4.2 FFD on the sheetlet

4.4.2.1 Refinement of the basic shape of the sheetlet

I also used FFD to deform the sheetlets to imitate the real tissue in the myocardium, as shown in Fig. 4.9. Through FFD, the cleavage planes are curved as well as the bundles between them while keeping the gaps among different parts like in Fig. 4.9b. For more convincing evidence and demonstration of the interest in our object-oriented multiscale model, I embedded several cardiomyocytes inside each bundle between cleavage planes as in Fig. 4.9c. It shows that after FFD, the gaps among the cardiomyocytes also remain. From these preliminary results, we confirmed that the FFD is a suitable technique for our model which is capable of effectively deforming the cleavage planes and manipulating such complex biological shapes.

4.4.2.2 Dynamic sheetlet during the cardiac cycle

As aforementioned in section 4.3.2.2, the cardiomyocyte bundles in the myocardium rearrange during the cardiac cycle. Meanwhile, the cleavage planes in ECM also deform along with the cardiomyocyte bundles to help the slippages among the tissues in CM and ECM. Nevertheless, it is not quantitatively clear how the cleavage planes deform during the cardiac cycle. Thus, in this section, I generated two sequences of dynamic sheetlets on the basis of the qualitative curve of myocardial thickness variation inspired from [Ferreira et al., 2015], the dynamic sequence in Fig 4.7 and two very simple assumptions.

In the first dynamic sheetlets sequence, it is simply assumed that the thickness of the cleavage planes varies according to the qualitative curve of myocardial thickness variation as in Fig 4.10 (a). As in Fig 4.10 (b), the thickness of cleavage planes from time points t_1 to t_9 (the same time points of Fig 4.7) are assumed to be 20 µm, 21 µm, 24 µm, 27 µm, 28 µm, 27 µm, 24 µm, 21 µm and 20 µm, respectively. The volume variation of the cleavage planes is presented in Fig 4.10 (c), as well as the generated virtual sheetlets.

In the second sequence, it is assumed that the thickness of the cleavage planes decreases as in Fig 4.11 (b), because according to the references [Wojciech et al., 2016, Barros, 2019, LeGrice et al., 1995b, Ashikaga et al., 2008], the wall thickness mainly accounts for the thickening and the re-orientation of the cardiomyocytes while the ECM gets thinner.

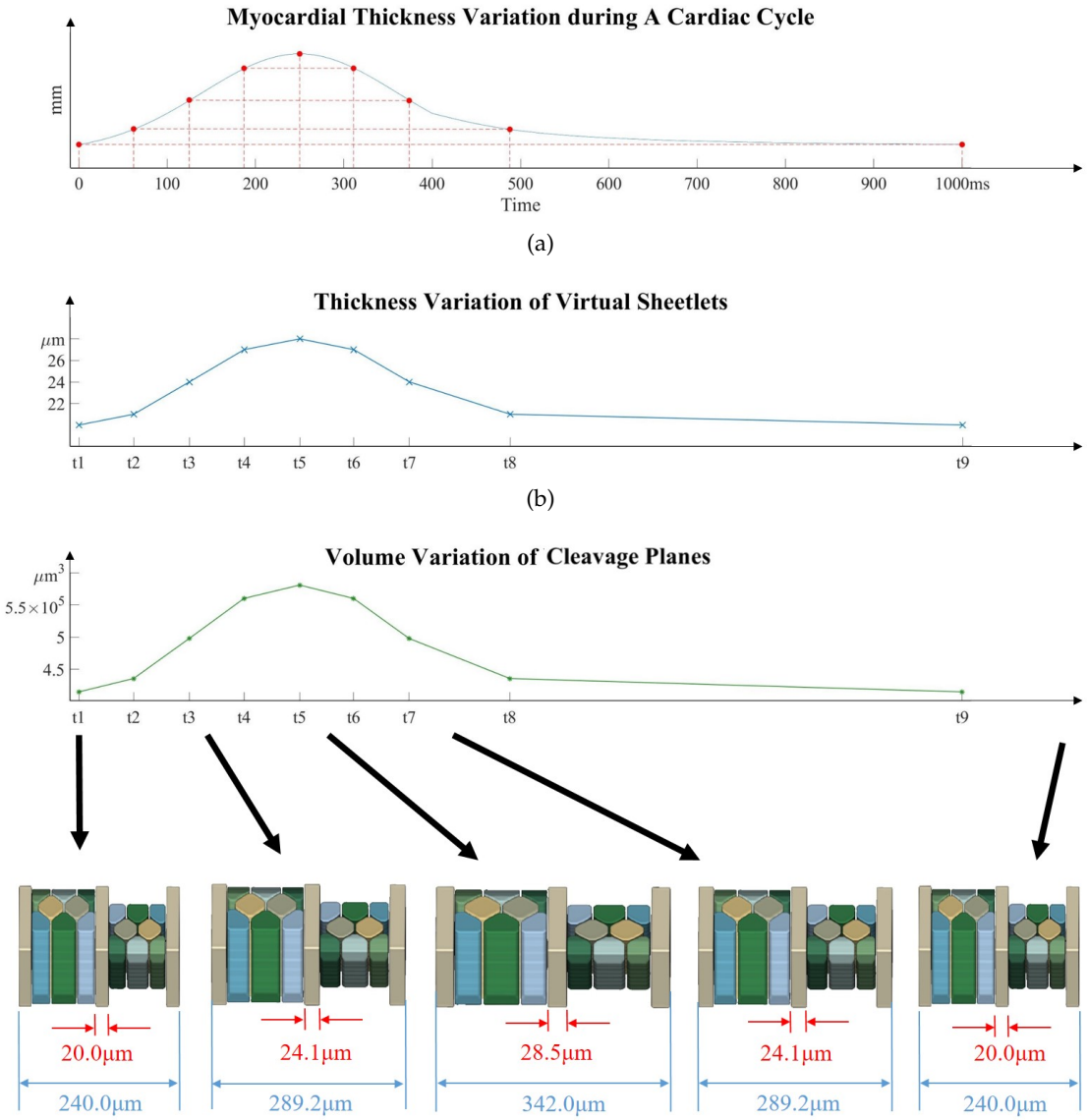

Figure 4.10: *Dynamic sequences of sheetlets during the cardiac cycle. (a) Variation of the myocardial wall thickness inspired from [Ferreira et al., 2015]. (b) Variation of the thickness of the cleavage planes. (c) Variation of the volume of the cleavage planes and corresponding 3D rendering of virtual sheetlets.*

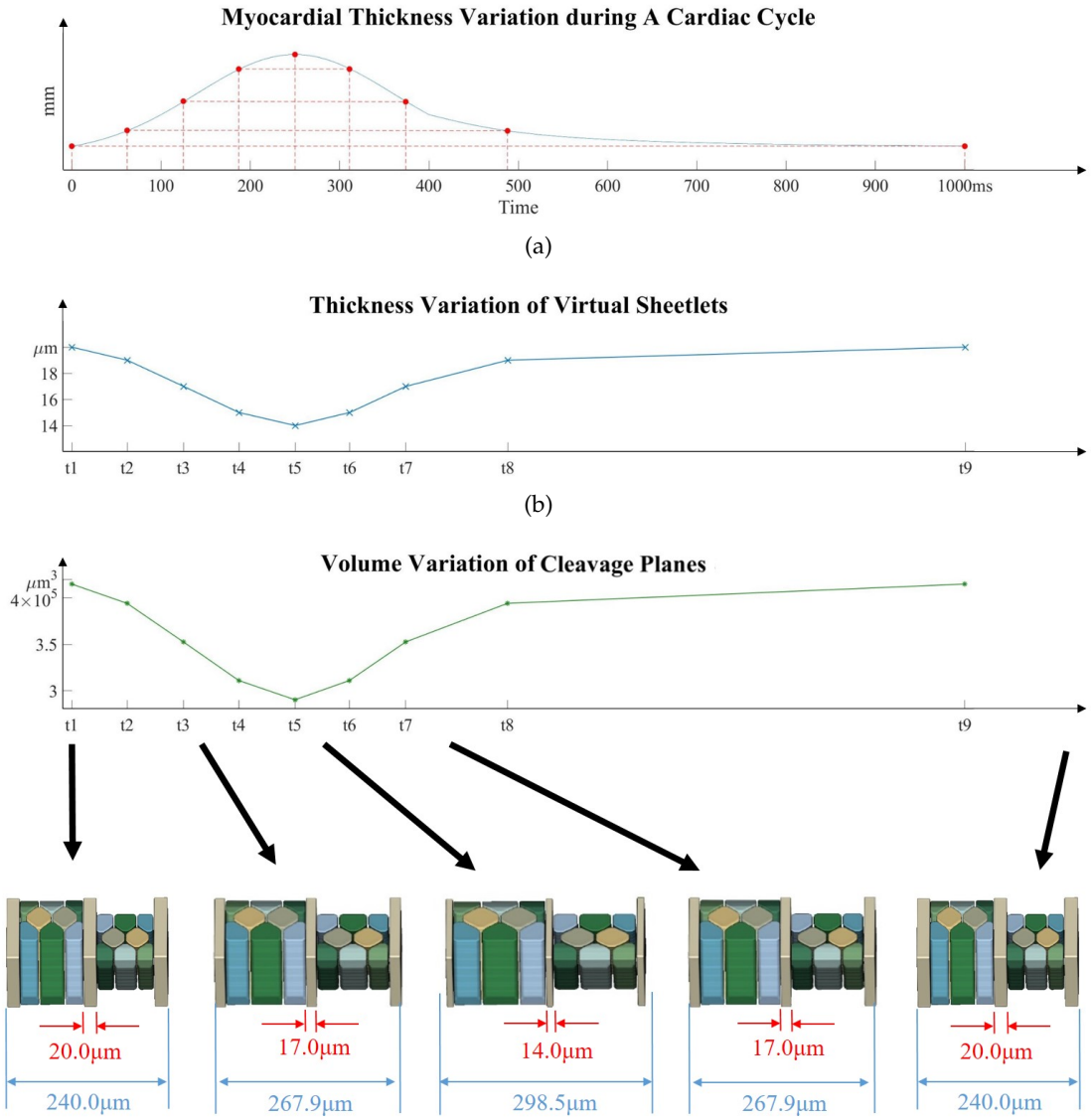

Figure 4.11: *Dynamic sequences of a cardiomyocyte bundle during the cardiac cycle. (a) Variation of the myocardial wall thickness inspired from [Ferreira et al., 2015]. (b) Variation of the thickness of the cleavage planes. (c) Variation of the volume of the cleavage planes and corresponding 3D rendering of virtual sheetlets.*

The thickness from t_1 to t_9 are assumed to 20 μm, 19 μm, 17 μm, 15 μm, 14 μm, 15 μm, 17 μm, 19 μm and 20 μm, respectively. The volume variation of the cleavage planes is presented in Fig 4.11 (c), as well as the generated virtual sheetlets.

4.5 Conclusion

In this chapter, the high-resolution part of the multiscale model has been developed. The simulation started with the basic functional unit of the heart, the cardiomyocyte module, at Level 4. A cardiomyocyte module is composed of a cardiomyocyte, an endomysium surrounding it and an intercalated disc connecting the cardiomyocytes end-to-end along the long side. According to the histological observations, the cardiomyocyte's shape is simulated as a long cylinder with a section of an ellipse, while the endomysium's shape is simulated as the side surface of the cylinder and the intercalated disc's shape is simulated as the undersurface. Inside a cardiomyocyte module, each part can be processed separately and combined afterwards to compose a complete basic functional unit, which can be embedded inside the cardiomyocyte bundle module and sheetlet module.

Then, a cardiomyocyte bundle module was built including six cardiomyocytes, a capillary and a layer of perimysium around them. The whole module's shape is also simulated as a cylinder with the capillary being a small cylinder in the centre and the cardiomyocytes being small cylinders around the capillary. The simulation requires designing the compact arrangement of the capillary and six cardiomyocytes in the section of the cardiomyocyte bundle. I employed a distance transform and the watershed algorithm to design it. After building the basic shape of the cardiomyocyte bundle module, I use FFD to refine the shape from a cylinder to a noisy truncated twisted ellipsoid to simulate the real shape in the biological tissues. For simulating various states in the cardiac cycle, I generated dynamic sequences of a cardiomyocyte bundle. Inspired from [Ferreira et al., 2015] and [Wojciech et al., 2016], I drew a curve of myocardial thickness variation and the curves of radius, length and volume variations. Simulations of a cardiomyocyte bundle are operated to show a qualitative shape variation at nine states during the cardiac cycle.

After that, a sheetlet module is built to simulate the laminar structure. The sheetlet module is composed of three parallel cleavage planes and two groups of cardiomyocyte bundles in between. The cardiomyocyte bundles between the same pair of cleavage planes have the same orientations while the two groups have crossing orientations. For a more realistic simulation, I use FFD to deform the shape of the sheetlet module to a curved shape. For more convincing evidence and demonstration of the interest in our

object-oriented multiscale model, I embedded several cardiomyocytes inside each cardiomyocyte bundle. The virtual dynamic sheetlets are also generated according to the curve of myocardial thickness variation and two simple assumptions.

The simulations of the shapes validate that our high-resolution model can generate virtual data at Levels 2, 3 and 4. Through FFD, the virtual data can simulate the real tissue and various states during the cardiac cycle.

Chapter 5

Virtual imaging simulation from real data

Contents

5.1 Introduction

After building the low-resolution and high-resolution models, it is validated that our multiscale model has the capability of generating basic virtual shapes of the heart's objects at various scales. Thus, it is necessary to involve real data and use their information to generate virtual volumes.

In this chapter, using the two sets of synchrotron data, I estimated their geometric parameters. They were used to simulate some specific detailed structures in the myocardium, such as the parallel-like laminar structure and bifurcated laminar structure.

For evaluation of the generated virtual volumes, virtual CT imaging simulation is implemented on the generated virtual volumes with a parallel-like structure. A brief introduction of the Reconstruction ToolKit (RTK) for virtual CT imaging is given, followed by the projection geometry of our simulation. For a more robust validation, Virtual imaging under various noisy situations is implemented. The generated virtual volumes and the reconstructed volumes from them are estimated qualitatively and quantitatively to validate the model.

Ultrasound imaging simulation is also implemented using the FieldII software [Jensen and Svendsen, 1992]. The results are also evaluated by calculating the orientations of the tissues inside.

5.2 Real data estimation

5.2.1 Synchrotron data

Benefiting from the previous work in CREATIS lab [Varray et al., 2013, Mirea et al., 2015], two sets of synchrotron phase-contrast data of two human heart samples were obtained. These human heart samples were supplied by the Medico-Legal Institute of Lyon IML HCL (n° DC - 2012 - 1588), extracted from two healthy adult hearts aged 32 and 35 years. They are projected with the synchrotron beam at the ESRF in Grenoble. For better absorption contrast, phase contrast is applied during the imaging [Cloetens et al., 1999]. 2499 projections were obtained to accomplish the 3D reconstruction of the tis-

sue [Weitkamp et al., 2011]. Each sample is reconstructed in 3D with an isotropic voxel size of $3.5 \times 3.5 \times 3.5$ μm^3. More details can be found in [Varray et al., 2013, Mirea et al., 2015].

5.2.1.1 Reconstructed data 1

The first set of synchrotron data is from the tissue sample situated in the posterior area of the LV with a size of $1753 \times 5600 \times 1050$ μm^3. It is shown in Fig. 5.1a with the blue box showing the borders. The cleavage planes inside exhibit a similar orientation but with subtle and smooth differences, which forms a parallel-like structure.

A ROI, corresponding to the solid red rectangular in Fig. 5.1c, is extracted from the sample for simulation with a size of $444.5 \times 5600 \times 444.5$ μm^3. One frame from the ROI is taken with a bunch of cleavage planes in it, as shown in the black rectangle inside. It is used to calculate the orientation of the tissues between the cleavage planes.

For calculating the thickness of cleavage planes and the interval distance in between, only the cleavage planes are extracted from synchrotron reconstructed data 1 and made to a binary volume as Fig. 5.1b shows. The corresponding ROI and frame in binary data are shown in Fig. 5.1d and Fig. 5.1f. The binary frame in Fig. 5.1f is also used to calculate the orientations of cleavage planes.

5.2.1.2 Reconstructed data 2

The second set of synchrotron data is from a tissue sample located in the anterior area of the LV, shown in Fig. 5.2a. This data is situated in the middle part along the radial direction, where the laminar structure has some branching cleavage planes. These arrangements play roles in the slippage of the sheetlets during the cardiac cycle.

The ROI showing a distinct branching structure is shown in Fig. 5.2c, corresponding to the red box in Fig. 5.2a. For more intuitive observation, the extracted binary data and ROI are shown in Fig. 5.2b and Fig. 5.2d, where the branching structure can be observed clearly.

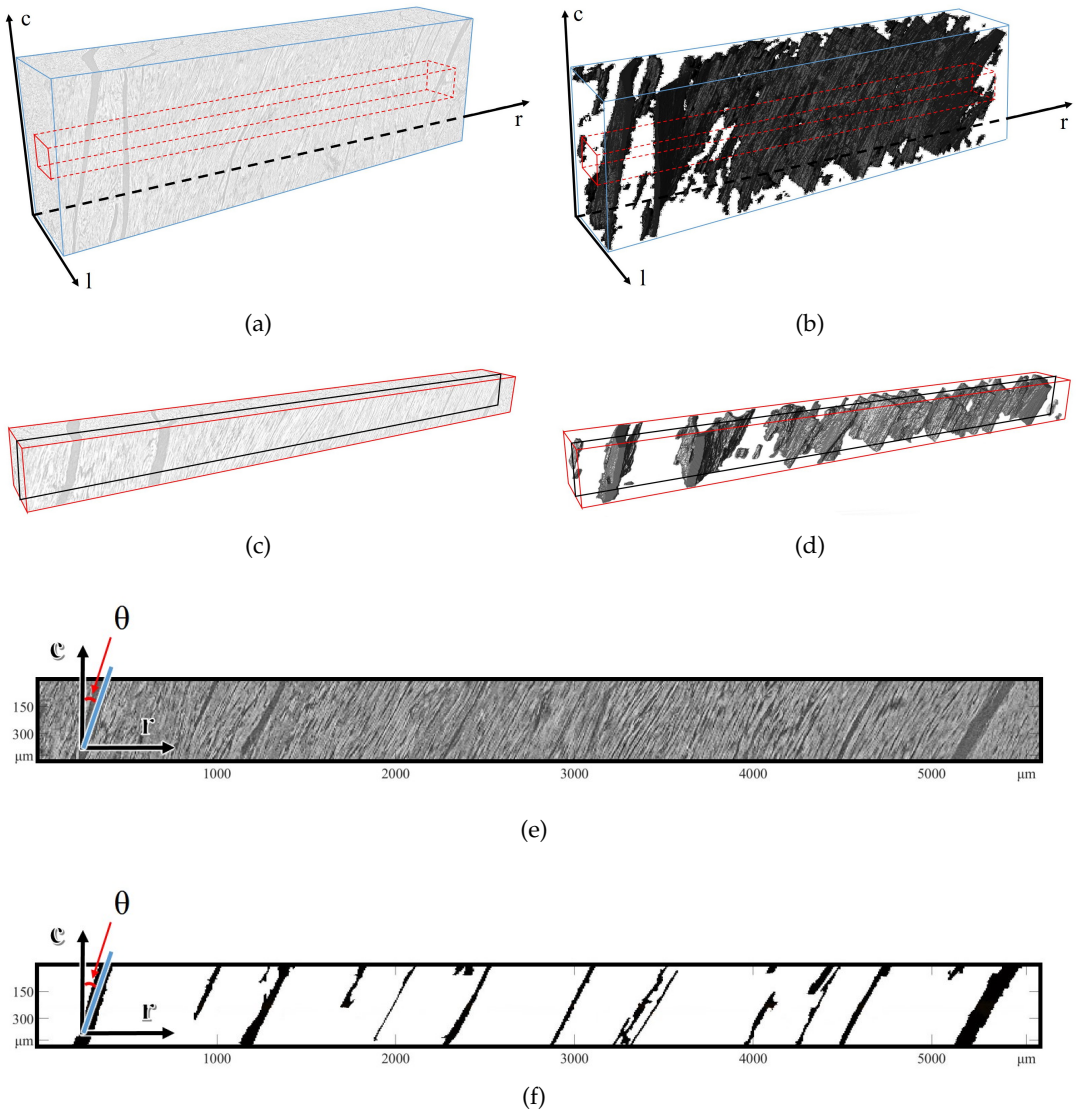

Figure 5.1: *Synchrontron with parallel-like structure. (a) Raw data. (b) Binary data. (c) ROI extracted from (a). (d) ROI extracted from (b). (e) Section extracted from (c). (f) Section extracted from (d).*

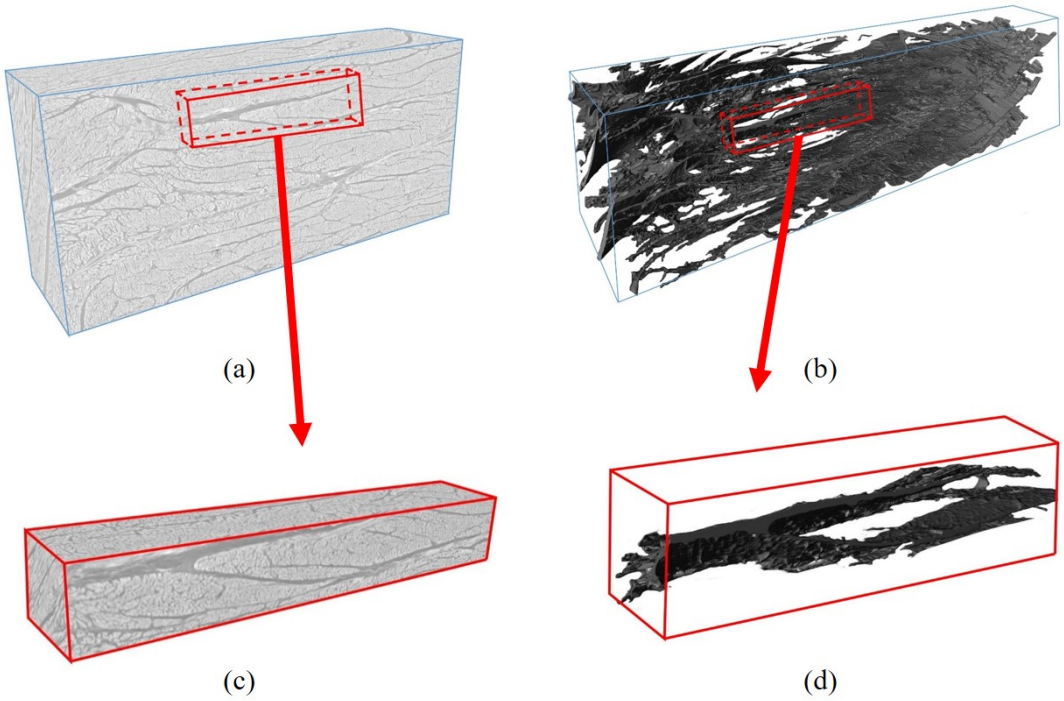

Figure 5.2: *Synchrotron data with a branching structure. (a) Raw data. (b) Binary data. (c) ROI extracted from (a). (d) ROI extracted from (b).*

5.2.2 Estimation of synchrotron data

On the basis of the ROI of the synchrotron data presented in Fig. 5.1c, I wanted to generate a virtual volume with a similar parallel-like structure in terms of the dimension, density, and orientations of cleavage planes and the orientations of the cardiomyocyte bundles between them. The orientations include helix and transverse angles (Φ and θ) defined in [Varray et al., 2017], as shown in Fig. 5.3. Thus, it is necessary to estimate these geometric parameters in the ROI. In the synchrotron data section related to the ROI in Fig. 5.1c, as shown in Fig. 5.4a, it is easy to observe the clear cleavage planes in the dark grey areas. So I extracted the binary data section only including the cleavage planes related to the ROI in Fig. 5.1d, as shown in Fig. 5.4b.

A blue line along the radial axis is first drawn in Fig. 5.4b for estimating the parameters. 12 pairs of intersection points between the blue line and the cleavage planes are obtained. At each pair of intersection points, the thickness of the cleavage planes is calculated and displayed in Fig. 5.4c. Then, using the first points of every adjacent pair of

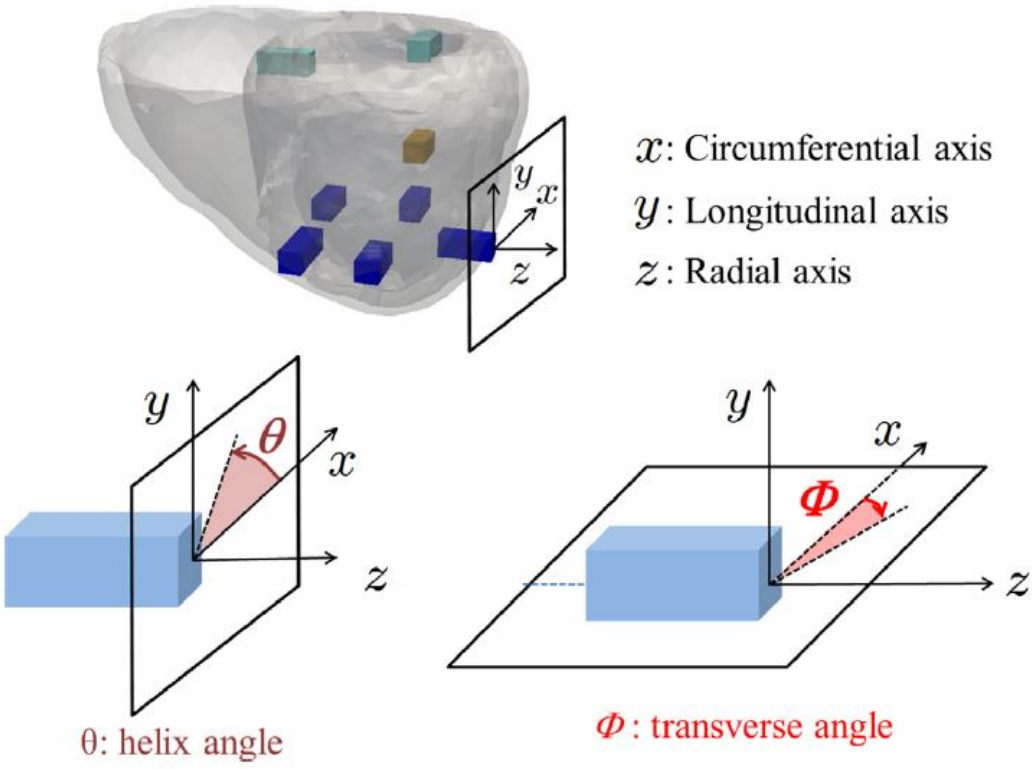

Figure 5.3: *Definition of angle θ and Φ. Angle θ is the angle between tissue and $x-y$ plane and angle Φ is the angle between tissue and $x-z$ plane, as helix and transverse angle defined in [Varray et al., 2017]. This figure is adapted from [Varray et al., 2017].*

intersection points, the interval distance of each pair of cleavage planes is also calculated and displayed in Fig. 5.4d.

In [Varray et al., 2017], a methodology is proposed to extract the orientations of cardiomyocytes in 3D phase-contrast synchrotron data using 3D Fourier Transform. The Fourier spectrum of a cardiomyocyte exhibits an ellipsoidal shape, while the low-frequency direction represents the direction along the length of the cardiomyocyte. Through principal component analysis, the orientation of a cardiomyocyte can be obtained. Thus, by means of this method, the orientations of each cleavage plane can be estimated in the binary frame in Fig. 5.4b. After knowing the positions of the intersection points, I introduced them to Fig. 5.4a. I used the same method to calculate the orientations of cardiomyocyte bundles between each pair of adjacent cleavage planes. The orientation results are shown in Fig. 5.4e and Fig. 5.4f.

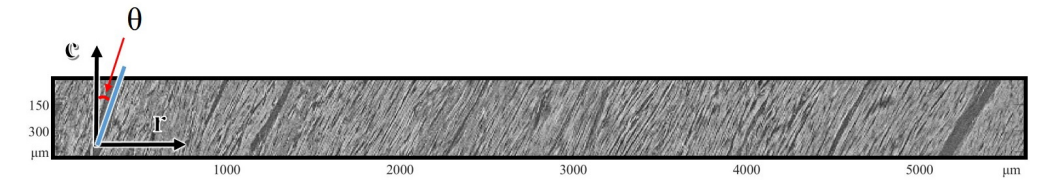

(a)

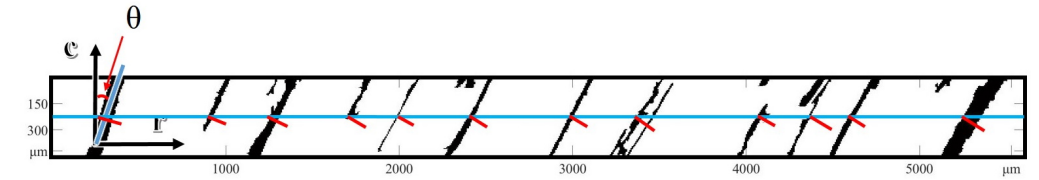

(b)

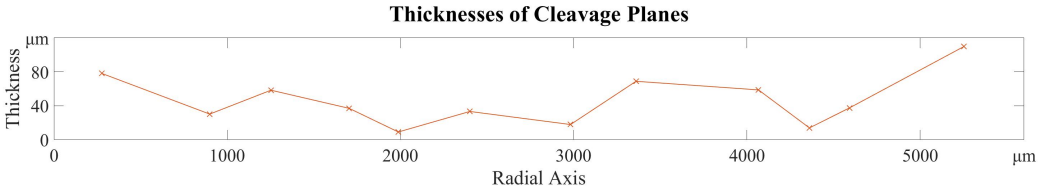

(c)

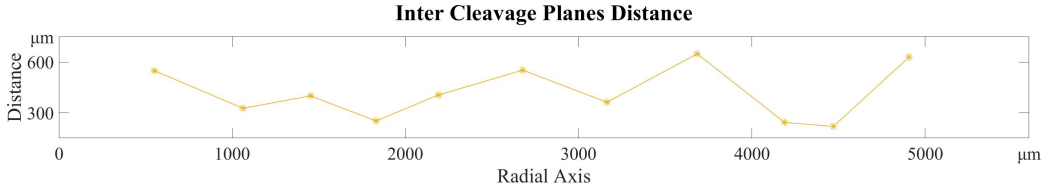

(d)

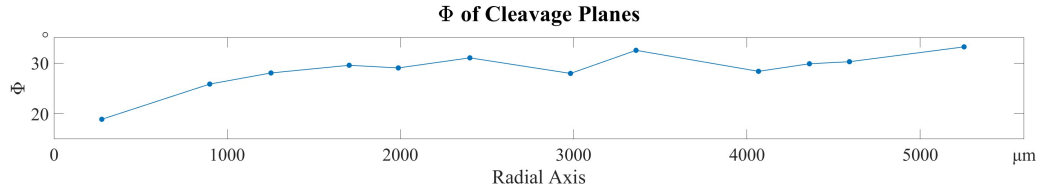

(e)

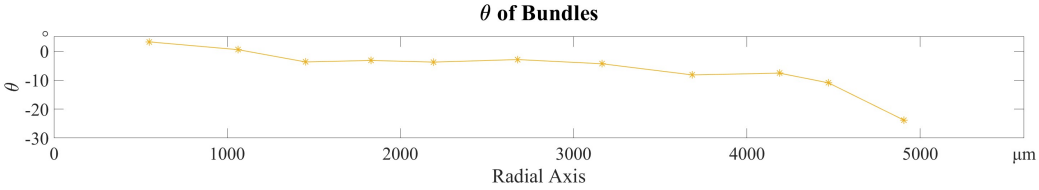

(f)

Figure 5.4: *Estimations of geometric parameters in synchrotron data. Sections of (a) synchrotron data and (b) binary data. The curves are the estimations of (c) thickness of cleavage planes, (d) interval distance between each pair of adjacent cleavage planes, (e) Φ angle of cleavage planes and (f) θ angle of cardiomyocyte bundles between each pair of adjacent cleavage planes, respectively.*

5.3 Real data simulation

Using the strategy presented in Section 4.4, ideal virtual volumes are generated with parallel-like and branching cleavage planes.

5.3.1 Simulation of data with parallel-like laminar structure

As Fig. 5.1 shows, there are some parallel-like structures inside the real synchrotron data. For simulation of the synchrotron data1, taking advantage of the estimations of thickness and inter cleavage plane distances in Fig. 5.4, a set of virtual parallel cleavage planes is first generated, as shown in Fig. 5.5a. Then, using the estimations of the θ angle, the cardiomyocyte bundles are generated, while the θ angle of each cardiomyocyte bundle is the same between the same pair of cleavage planes and varies among different pairs, as shown in Fig. 5.5b. After that, using the estimations of the Φ angle and FFD, the whole virtual volume in Fig. 5.5b is deformed so that the Φ angles are applied in the cleavage planes and the cardiomyocyte bundles inside, as shown in Fig. 5.5c. As in the synchrotron data, the cleavage planes seem parallel but have a subtle difference. The amplitudes of cleavage planes, background, and bundles are set as 100, 180, and 200, respectively.

5.3.2 Simulation of data with branching laminar structure

As Fig. 5.2 shows, there are also branching structures in the real data. A virtual volume with a branching structure is generated for the simulation of the synchrotron data 2. I utilized the sheetlets with paralleled cleavage planes to simulate the branching structure with FFD, which can make the cleavage planes merge. As the results in Fig. 5.6 show, the cleavage planes merge and the tissue inside remains separated after the deformation. However, because the branching structure in the virtual volume is generated using FFD, at the merging part, the cardiomyocyte bundles join together. I will continue to refine this in the future.

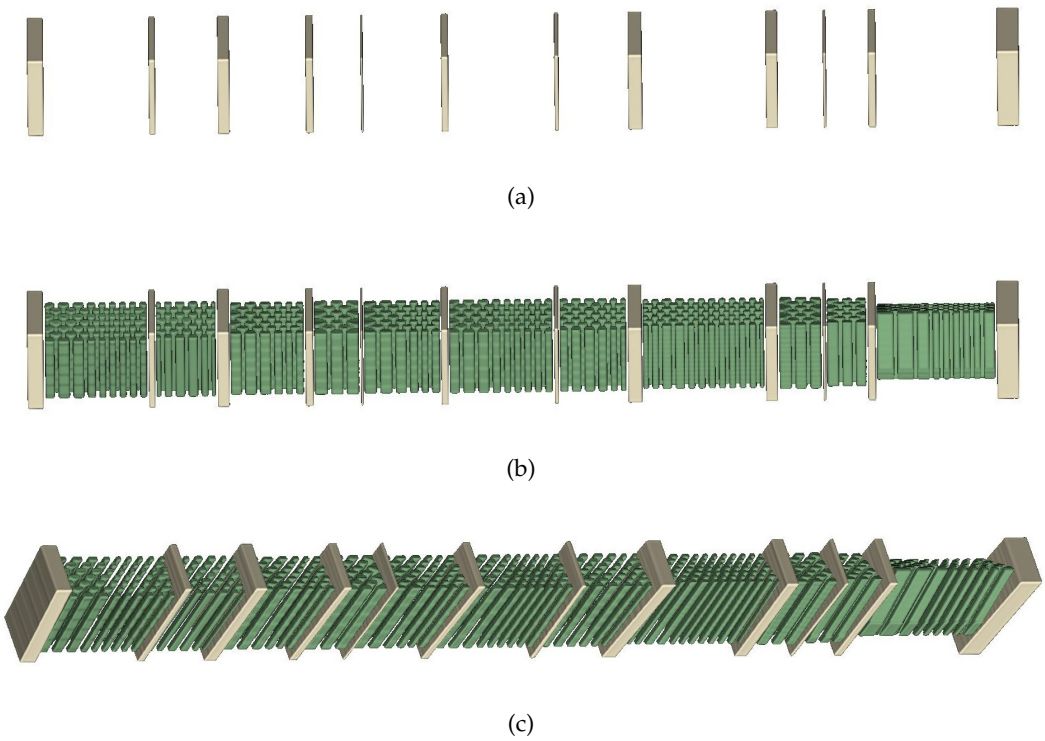

(a)

(b)

(c)

Figure 5.5: *Ideal virtual volume generation. (a) Virtual parallel cleavage planes. (b) Vvirtual volume with cardiomyocyte bundles oriented according to θ angle. (c) Ideal virtual volume with orientations according to real synchrotron data.*

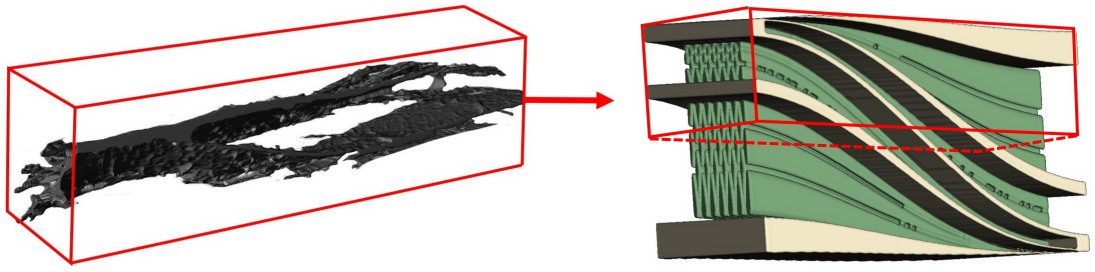

(a) (b)

Figure 5.6: *Simulation of the branching laminar structure. (a) Binary data same as Fig. 5.2d . (b) Virtual volume generated by our model coarsely simulating the branching laminar structure.*

5.4 Virtual X-Rays imaging

The synchrotron data used to get the structure of the tissue come from X-ray phase-contrast imaging acquisitions carried out at the ESRF. For validation of the generated virtual volume, in terms of structure and orientation, virtual X-Rays imaging of our synthetic model is performed, but for simplicity, I omitted the phase information and focused on the absorption information only and us the ideal virtual volume with parallel-like structures.

5.4.1 Principle of virtual X-Ray imaging

The Reconstruction ToolKit (RTK) [Rit et al., 2014] is used to simulate the cone-beam CT imaging procedure and to get the reconstructed volume of the virtual volume using the Feldkamp-David-Kress (FDK) algorithm [Feldkamp et al., 1984]. The illustration of the projection geometry used in RTK is highlighted in Fig. 5.7. In the geometry of this simulation, all sources during the rotation (indicated by red spots) are located in the same plane. The blue curve arrow, at the centre, demonstrates that the data rotates in the anticlockwise direction. Meanwhile, the distance from the source to the isocenter (SID) is fixed at 10 meters, and the distance from the source to the detector (SDD) is fixed at 10.3 meters, which means that the distance from the isocenter to the detector is set at 0.3 meters to simulate a quasi-parallel light beam close to that of the ESRF and to create projections similar to the acquired data. The data are placed as in Fig. 5.7d, where the transmural direction of the data is perpendicular to the horizontal plane. The central line is passed from source to isocenter and then to the detector origin. In the RTK tool, 256 projections are generated before the reconstruction of the volume.

5.4.2 Virtual imaging

The virtual imaging is performed on the generated ideal virtual volume in Fig. 5.5c. The ideal virtual volume is put into RTK to simulate the cone-beam CT imaging procedure where the virtual volume projections are obtained, and then, as well as the reconstructed volume from the projections of the virtual volume, by the FDK algorithm. 256 projections

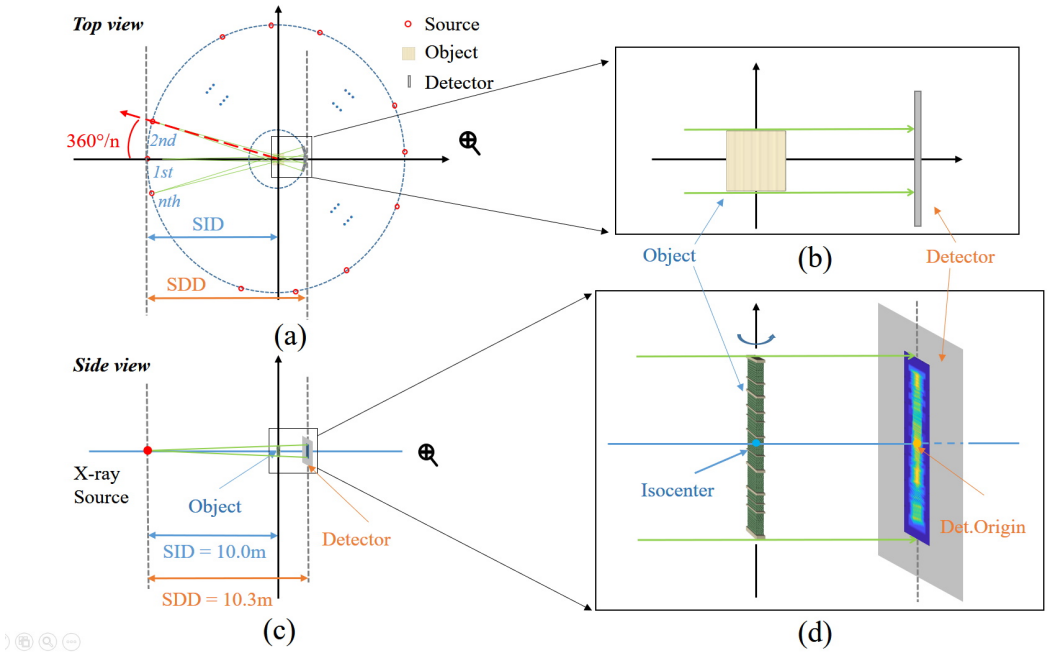

Figure 5.7: *RTK 3D projection geometry. (a) Top view of the system. (b) Zoomed-in view around the detector part in (a). (c) Side view of the system. (d) Zoomed-in view around the detector part in (c). The green arrow lines denote the ray. Det.Origin: Detector Origin. SID: source to isocenter distance. SDD: source to detector distance.*

are generated in each simulation, and three projections are displayed in Fig. 5.8 during the virtual imaging from three distinct source positions.

For a 3D viewing of the reconstruction result, Fig. 5.9a demonstrates the ideal virtual volume generated from our model, while the cleavage planes and the cardiomyocyte bundles are oriented according to the parameters estimated. The cardiomyocyte bundles are separated clearly. Fig. 5.9d shows the reconstructed volume from the ideal volume after virtual imaging in RTK. The reconstructed volume has some blurring, which is tolerable, but justifies that our model can be used to simulate the synchrotron data. Moreover, after the virtual imaging process, the reconstructed result exhibits a similar geometric shape with a tolerable blurring.

After this first virtual imaging, the cardiomyocytes are embedded inside the cardiomyocyte bundles in a partial section of cleavage planes, and virtual imaging is also operated on them. The results shown in Fig. 5.9b and Fig. 5.9e demonstrate that after the RTK tool, the volume keeps an ideal geometric shape and the gaps between cardiomy-

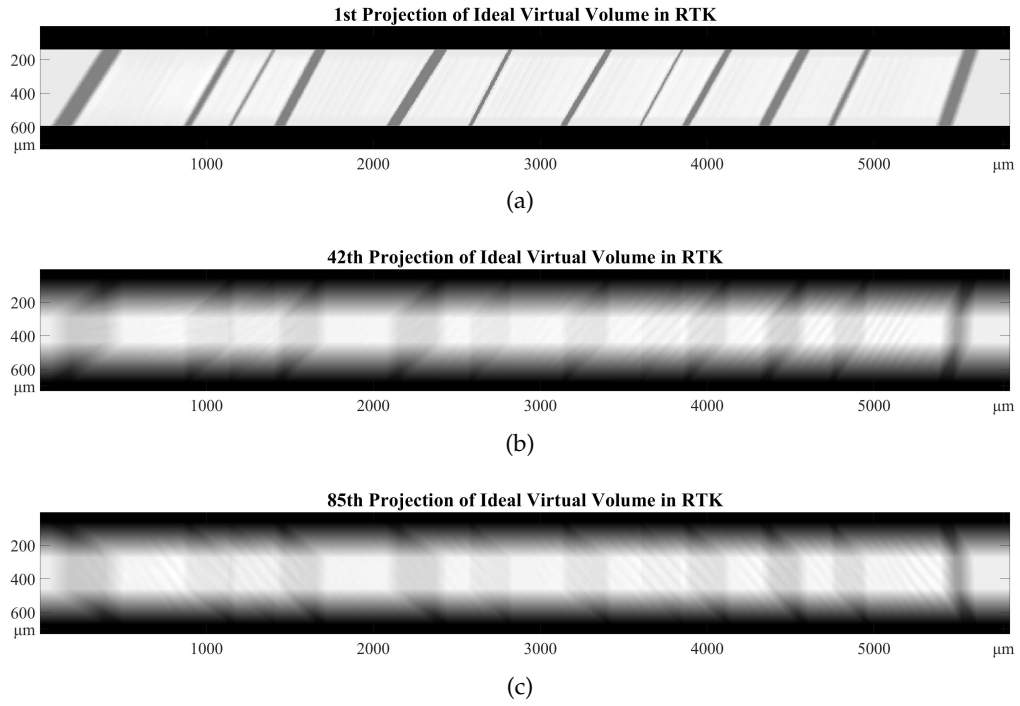

Figure 5.8: *Synthetic projections of the ideal virtual volume calculated by the virtual X-rays imaging device. (a) Projection n°1: projection angle equals* 0°. *(b) Projection n°42: projection angle equals* 42°. *(c) Projection n°85: projection angle equals* 119.5°.

ocytes remain. The results shown in Fig. 5.9c and Fig. 5.9f demonstrate that the orientations of the tissues vary as expected, which is correct according to the real situation, and after the reconstruction, the variation of orientations remains.

5.4.3 Virtual imaging under noisy situations

For the comprehensiveness of validation, the virtual imaging simulations under noisy situations are also performed at various noise levels. Different Gaussian noise levels are imposed onto the 3D ideal virtual volumes and the virtual X-ray image simulations are performed. I compared the data generated from our model with/without noise.

The probability density function p_G of the Gaussian noise $G(\mu,\sigma)$ is given by Eq. (4.8) in section 4.3.2 (Page 62). Signal-to-Noise Ratio (SNR) is adopted to represent the noise level according to:

$$SNR_{dB} = 10\log_{10}\left(\frac{\sum_{i,j,k} S^2(i,j,k)}{\sum_{i,j,k} N^2(i,j,k)}\right) \tag{5.1}$$

where $S(i,j,k)$ and $N(i,j,k)$ are the values of voxels at (i,j,k) position in the ideal virtual volume and the noisy one, respectively.

Centered Gaussian noises $G(0,\sigma)$ are imposed to the ideal virtual volume where σ equal to 5 and 10, while the SNR equal to 31.03 dB and 25.01 dB, respectively. After the simulations under noisy situations at various noise levels, the reconstructed volumes are obtained, and the 2D partial sections of them are displayed in Fig. 5.10. The blurry effect of reconstructed volumes increases along with the increment of the level of noise.

The results in these figures validate that our model can generate experimental data which can be used as input for a virtual imaging system and get the expected visual result with an appropriate arrangement of tissues.

5.4.4 Quantitative evaluation

To quantitatively evaluate the results, Maximum Local Error (MLE), Root Mean Square Error (RMSE) and Bhattacharyya distance [Bhattacharyya, 1946] are used. To estimate the reconstruction effect, RMSE is calculated on the amplitudes of the voxels and the orientations of the tissues, which is defined as:

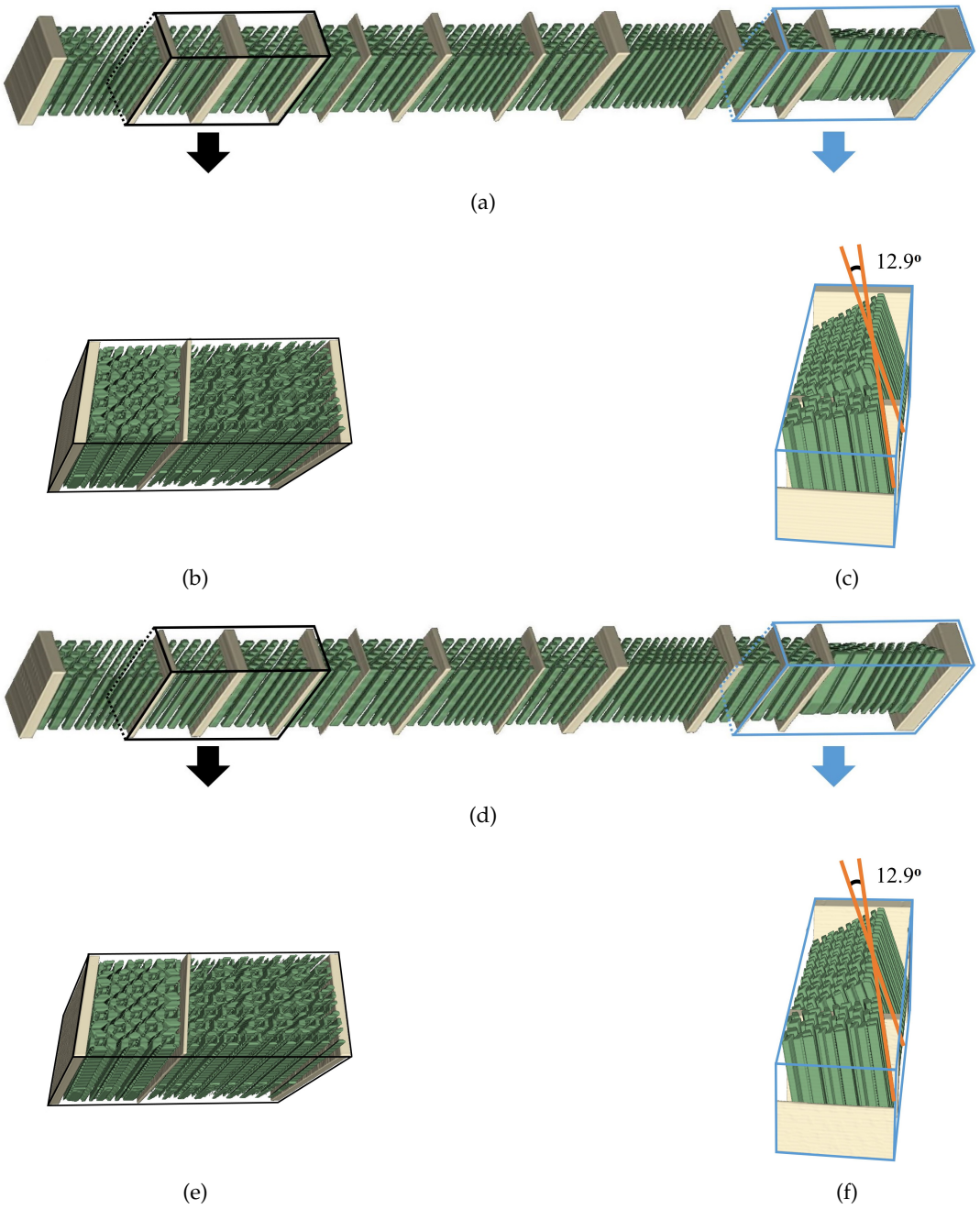

Figure 5.9: *Reconstruction of the ideal virtual volume and detailed structure comparisons. (a) Ideal virtual volume. Sub-volumes of ideal volume embedded with cardiomyocytes are shown in (b) with ROI in the black box and (c) ROI in the blue box. (d) Reconstructed volume from (a) after RTK. Sub-volumes of reconstructed volume embedded with cardiomyocytes are shown in (e) with ROI in the black box and (f) ROI in the blue box. The cardiomyocyte bundles are separated after virtual imaging as well as the cardiomyocytes embedded.*

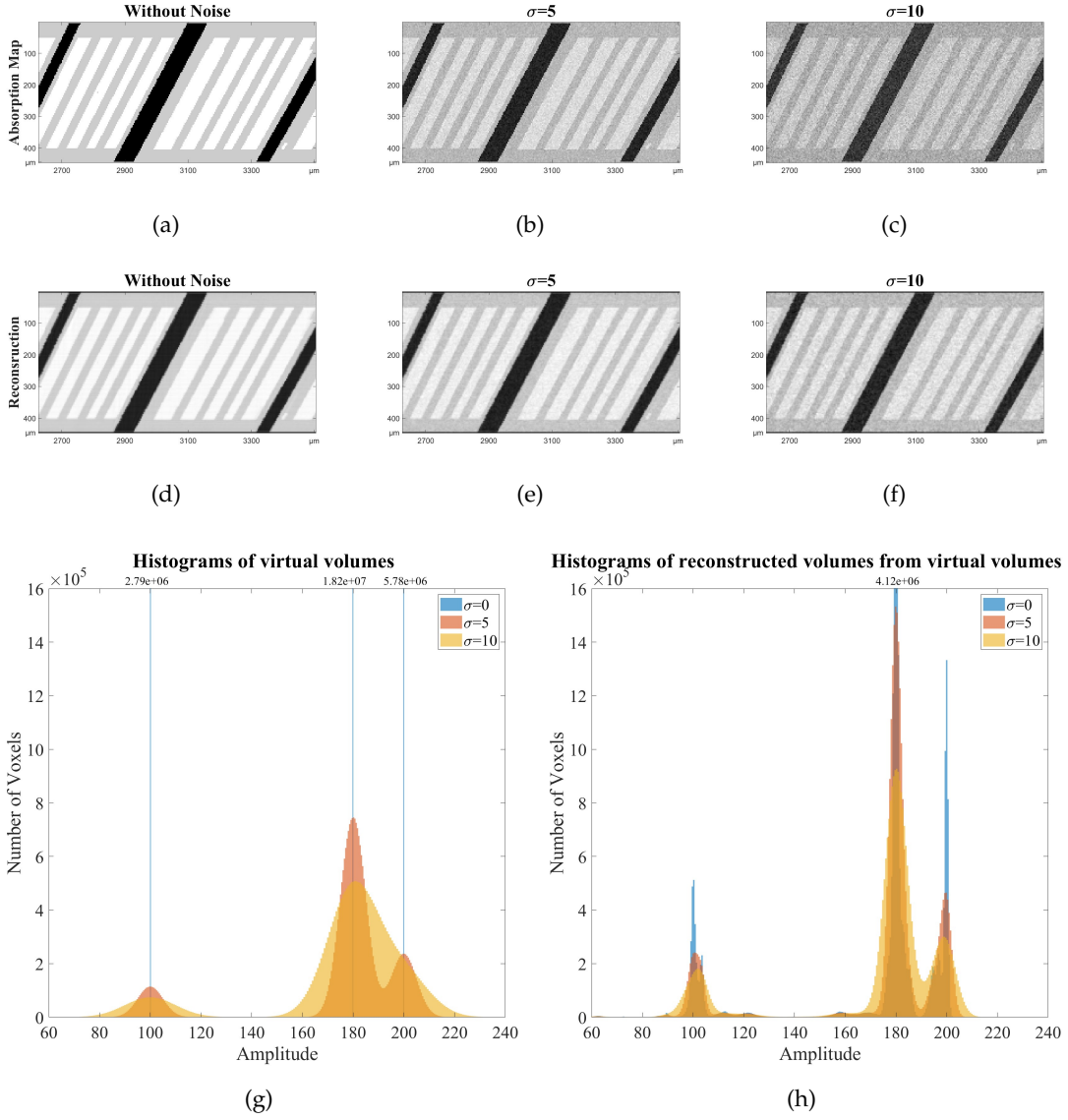

Figure 5.10: *Illustration of the contrast evolution under different noisy situations. For the ROI shown by the black box in Fig. 5.9, various sections are extracted from (a) ideal virtual volume, and noisy virtual volumes (b) $\sigma = 5$, (c) $\sigma = 10$. Sections of the reconstructed volumes: (d) from (a), (e) from (b) and (f) from (c). (g) Histograms of the virtual volumes under different noise situations. (h) Histogram of reconstructed virtual volumes. The blurry effect in reconstructed volumes increases along with the noise level. The peaks in the histograms become larger with the noise level.*

$$RMSE = \sqrt{\frac{\sum_{i=1}^{N}(y_i - \hat{y})^2}{N}}, \tag{5.2}$$

where y_i is the i^{th} element of the sample to be evaluated and $\hat{y}$ is the set real value.

I also used Bhattacharyya distance, which is usually used in statistics to measure the similarity of two probability distributions, in order to evaluate the similarity between the volumes generated by our model and the reconstructed volumes from them. For two probability distributions p and q over the same domain $\boldsymbol{D}_{DB}$, the Bhattacharyya distance D_B is defined as

$$D_B = -\ln\left(\sum_{x \in \boldsymbol{D}_{DB}} \sqrt{p(x)q(x)}\right), \tag{5.3}$$

with $D_B \in \mathbb{R}$ and $0 < D_B < \infty$. The increase of D_B means a decrease in the similarity between the two distributions.

To globally and quantitatively evaluate the generated volumes, RMSE and Bhattacharyya distance (D_B) are calculated. I calculated the RMSE of the reconstructed volumes from the virtual volumes at various noise levels to estimate the reconstruction effect. To evaluate the similarity between the virtual volumes and the reconstructed volumes from them as well as the influence of the noise, I calculated D_B, which is between the normalized histogram of a virtual volume and the reconstructed volume from it. The domain $\boldsymbol{D}_{DB}$ in Eq. (5.3) is set as $[60,240]$ according to the maximum range of the amplitude of the volumes. The global RMSE and the Bhattacharyya distances are summarized in Tab. 5.1.

Table 5.1: *Global evaluation - RMSE and Bhattacharyya distance*

σ	SNR (dB)	RMSE	D_B
0	∞	3.84	0.48
5	31.03	6.62	0.08
10	25.01	11.45	0.07

To locally and quantitatively evaluate the results, the RMSE and MLE are calculated in two parts in the volume: cleavage planes and cardiomyocyte bundles. The MLE is defined as the maximum value of the absolute error on a restricted volume, here the cleavage planes or cardiomyocyte bundles. The RMSE and MLE at various noise levels are summarized in Tab. 5.2.

Table 5.2: *Local evaluation - RMSE and MLE*

σ	Cleavage planes		Cardiomyocyte bundles	
	RMSE	MLE	RMSE	MLE
0	0.28	6.77 (6.77%)	0.19	5.88 (2.94%)
5	1.52	12.80 (12.80%)	1.76	11.19 (5.60%)
10	3.01	24.02 (24.02%)	3.51	20.72 (10.36%)

Then I calculated the orientation of the tissue in the ideal virtual volume with the method introduced in [Varray et al., 2017] and evaluated the RMSE of θ and Φ angle at various noise levels compared to the set angle. The results are given in Tab. 5.3.

Table 5.3: *RMSE of the angle θ and Φ at different noise levels*

σ	SNR (dB)	RMSE θ (°)	RMSE Φ (°)
0	∞	0.50	0.47
5	31.03	0.52	0.46
10	25.01	1.03	0.88

For the global evaluations, the RMSE on the volumes increases along with the noise level. Concerning the interpretation of the Bhattacharyya distance, the case without noise has to be carefully studied. Indeed, the amplitudes of the ideal volume are only composed of the three values set, leading to a histogram with only these three peaks. Thus D_B, in the situation without noise is much larger than in the noisy situations, while it decreases in the noisy situations along with the increase of the noise level. For the local evaluations, the local RMSE and MLE showed an increasing trend along with the noise level. These trends caused by the various noise are logical and realistic.

The RMSE of the angles θ and Φ have very subtle changes along with increasing noise and keep a low value for each noise level, which validates that noise level does not have much influence on estimating the orientation and the volume remains the orientation of the tissue after virtual imaging.

In general, the computed quantitative evaluations demonstrate a logical behaviour with the noise level in the virtual imaging, as what occurs in the realistic situation. These results validate that the proposed model has the ability to generate volumes simulating realistic data, that can be set as the input of the virtual imaging. The measure parameters after the virtual imaging remain coherent with their initial values.

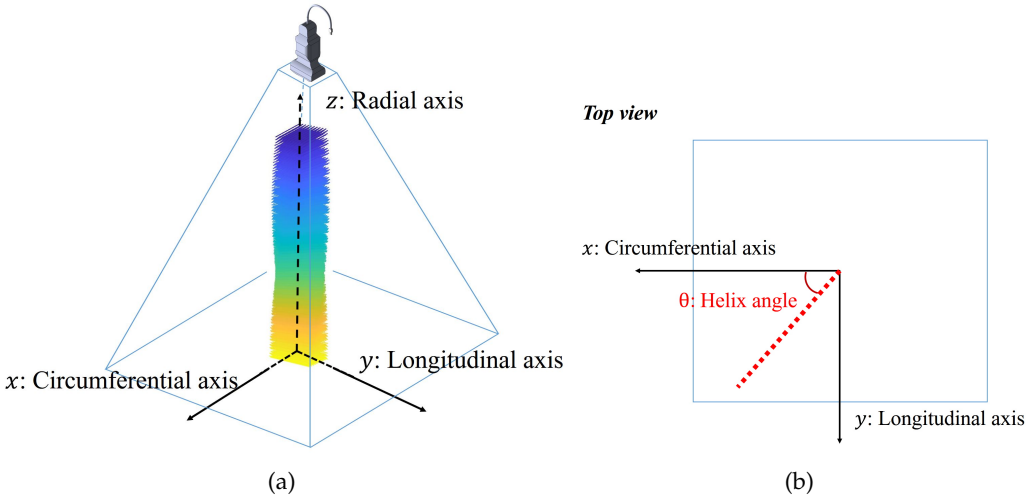

Figure 5.11: *Schematic 3D geometry of virtual US imaging. (a) 3d view. (b) Top view with the cardiomyocyte bundle and the illustration of helix angle.*

5.5 Virtual ultrasound imaging

For the ultrasound (US) imaging simulation, the standard approach is to use the FieldII software which computes the ultrasound field depending on the initial probe parameters and the transmitted signal [Jensen and Svendsen, 1992]. Then, while scatters are added to the medium, the backscattered signal is generated and recorded by the probe. The 3D geometry of the virtual US imaging is displayed in Fig. 5.11. The first step is to use the initial virtual model to generate scatters consistent with the bundle and the cleavage planes. For the US simulation, I define a 2D array composed of 32 by 32 elements (1024 in total). 3 steering angles (-10°, 0°, 10°) are set in transmission for each direction leading to a total of 9 steered 2D plane waves. Using the generated scatters of the model, I get 9 raw signal volumes from FieldII. First, the volumes are beamformed. Then, the local coherence is evaluated in order to extract the local orientation of the bundle, using the method previously validated [Turquin et al., 2019].

To test the proposed model, 3 sets of simulations are performed. Three sets of virtual volume scatters are generated at first with cardiomyocyte bundles simplified as lines inside, as the model flexibility allows to define it.

In the first set of simulations, 18 virtual volumes are generated in each of which the

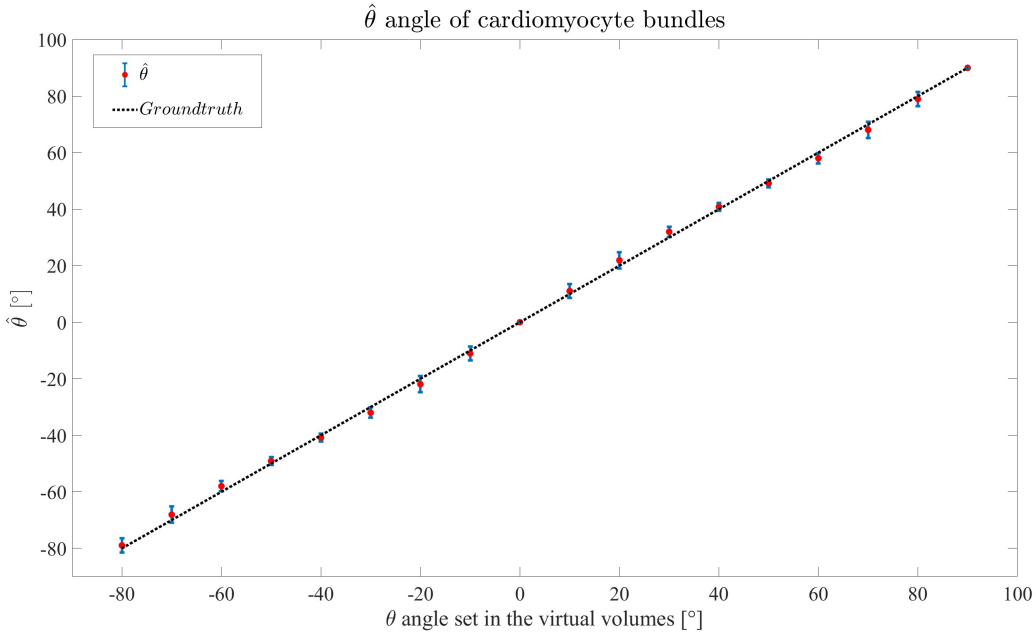

Figure 5.12: *Estimations of θ angle of cardiomyocyte bundles after virtual US imaging.*

θ angle of the cardiomyocyte bundles is mono-oriented. The θ angle in each simulation is set from $-80°$ to $90°$ with an interval of $10°$. After the procedure aforementioned, $\hat{\theta}$, estimations of the θ angle, in each volume are obtained at several depths (radial direction). The mean value and standard deviation of each volume after virtual US imaging are calculated and summarized in Fig. 5.12. The mean value of the $\hat{\theta}$ angles in each simulation is very close to the set θ values while the standard deviation remains low, which validates that the mono-oriented virtual volume can be used as the input data of virtual US imaging. The RMSE of $\hat{\theta}$ is $2.51°$ which remains low.

In the second simulation, after validation of the mono-oriented situation, I generate 2 groups of cardiomyocyte bundles in the same virtual volume with θ angles set as $-40°$ and $50°$, respectively. The estimations, $\hat{\theta}$, in the volume along its transmural direction are summarized in Fig. 5.13. From the result, the estimated $\hat{\theta}$ angle is mostly according to the set of θ values, except that at the joining part of 2 groups of cardiomyocyte bundles. It can be explained by the way of computing the local anisotropy that investigates signals at several wavelengths in the radial direction. In one simulation, the wavelength is around

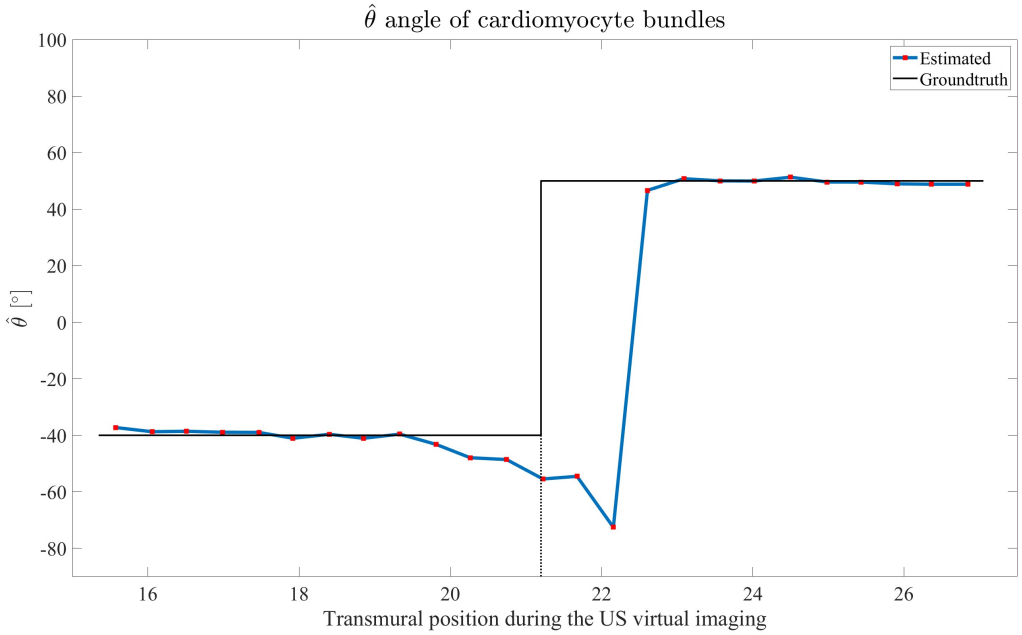

Figure 5.13: *Estimations of θ angle of cardiomyocyte bundles in the volume with 2 groups of cardiomyocyte bundles after virtual US imaging.*

0.5 mm and the coherence integrate the information on 4 wavelength (2 mm) . It also explains that the RMSE is 37.34° which is quite high, although the RMSE before the 9^{th} test point is only 0.95° and that after the 13^{th} test point is only 0.79°

In the third simulation, limited by the resolution of the US, it is not possible to use the geometric parameters estimated from synchrotron data as in Fig. 5.4f. According to the estimations in Fig. 5.4, the interval distances between cleavage planes are around 200 µm to 600 µm, so I set the interval distance to 400 µm. Then, 25 groups of cardiomyocyte bundles are generated in the same virtual volume with θ angles set from $-60°$ to 36° with an average interval of 4°, which makes the dimension along the transmural direction equivalent to 1 cm. Using the same strategy, the results are summarized in Fig. 5.14. The estimated angles at different transmural positions have the same trend with the set θ angles with tolerable errors. The RMSE of $\hat{\theta}$ angle is 5.29° which is tolerable inside the same volume because the wavelength influences the estimated angle.

In general, the results showed that the virtual volumes generated by our model have similar characteristics to the real data during the virtual US imaging, using the same

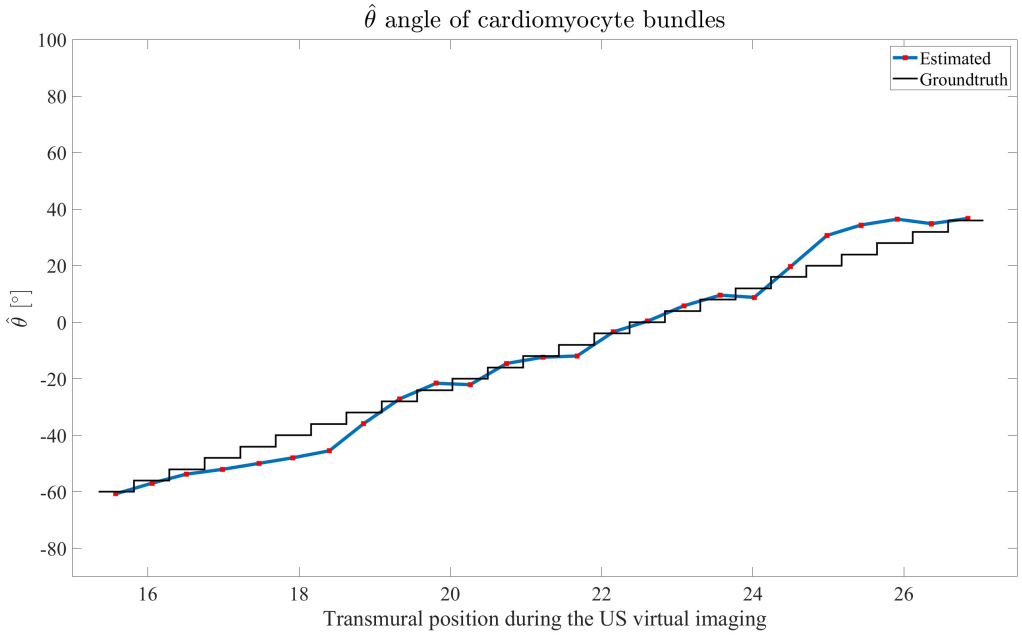

Figure 5.14: *Estimations of θ angle of cardiomyocyte bundles in the volume with 10 groups of cardiomyocyte bundles after virtual US imaging.*

general mathematical multiscale model I developed during my PhD.

5.6 Conclusion

In this chapter, validation of the proposed multiscale deformable model is performed by way of virtual imaging while using the real data to generate the virtual tissues.

Synchrotron data imaged at ESRF has been used as the real data in this chapter because of its high reconstruction resolution compared to other common imaging modalities. Two sets of synchrotron data are demonstrated to display the parallel-like and branching laminar structures of the different positions in the myocardium. Estimations of the synchrotron data with the parallel-like structure are performed to get the geometric parameters, including cleavage plane thickness, inter cleavage plane distance, as well as the orientations of cleavage planes and cardiomyocyte bundles.

Real data simulations have been operated to generate 3D virtual volumes with parallel-like and branching structures. An ideal virtual volume with a parallel-like structure is

generated according to the estimations of the real synchrotron data 1. Another virtual volume is generated to quantitatively simulate the branching laminar structure.

Then, virtual X-ray imaging is performed on the ideal virtual volume with a parallel-like structure. Through visual comparisons, it is validated that, after virtual imaging, the general structure and the gaps among tissues remain. For more robust evidence, virtual imaging under various noisy simulations is operated. Quantitative evaluations are employed on the virtual volumes and the reconstructed volumes from them. The results demonstrated the reconstruction effects decreased along with the increase in the noise level, as what occurs in the realistic situation.

Three sets of virtual US imaging simulations were also been performed in virtual volumes with mono-oriented cardiomyocyte bundles, 2 groups of cardiomyocyte bundles and 10 twisted-arranged cardiomyocyte bundles, respectively. Estimations of the θ angle are also accomplished for more robust validation of the model. From the results, the estimations can basically accord to the ground truth except for some errors caused by the signal length (several wavelengths) that is used for local orientation estimation using the method previously published [Turquin et al., 2019].

All the results in this chapter validated that the virtual volumes generated by my model have a similar effect to the real data both in visual observation and virtual imaging.

Conclusions and Perspectives

Conclusion

The aim of this thesis is to build a 3D multiscale deformable model for generating a virtual synthetic heart that can be used in research and virtual imaging.

The model has been proposed with five levels and a hierarchical structure at various scales, from the macro- to the micro-scale. The proposed model has two parts: the low-resolution model and the high-resolution model. It is a voxel-based model because voxels are the basic units of our model and the voxel-based model is more flexible to scale in size and deform. It has an object-oriented description, designed to describe each object at different scales. For each object in the model, a geometric model was built to describe the shape by observing the images of realistic tissue while a feature vector is designed to save the parameters for describing the object's features. I presented the FFD technique and the procedure of deforming each object to improve the similarity between the model and the realistic tissue, as well as being able to mimic the heart deformation along a cardiac cycle.

In the low-resolution model, on the basis of PLI data observation, surface models of epicardium and endocardium were built using the superellipsoid as a coarse data-fitting and FFD as a fine data-fitting. The results showed that the low-resolution model has the ability to reasonably simulate the surfaces, the partial epicardium and LV endocardium and the volume, ventricular myocardium at Level 1, with acceptable low errors. Through the inverse procedure of FFD, volume registrations are carried out, transferring the information of real data into a uniform model volume that qualitatively describes the data. The results show that the uniform model can quantitatively describe the azimuth and elevation angle information from the PLI data. Therefore, comparisons of myocardial

information from various individuals may be accomplished on this uniform volume.

In the high-resolution model, on the basis of synchrotron data, the virtual cardiomyocyte module at Level 4, the virtual cardiomyocyte bundle module at Level 3 and the virtual sheetlet module at Level 2 were illustrated. The shapes for these basic objects generated by our model and their shapes after FFD were demonstrated, which shows that FFD is suited for our multiscale model. Inspired by some references to the cardiac cycle, dynamic sequences of a cardiomyocyte bundle and sheetlets were generated to qualitatively simulate the shape change during the cardiac cycle.

To validate the interest of our model, the virtual volumes with parallel-like and branching laminar structures were generated using FFD, which shows the capability of the proposed model to generate specifically shaped structures in the heart. At last, virtual imagings were operated to obtain a more robust validation. Virtual CT on the parallel-like volumes generated by our model was performed under different noise levels and evaluated the results visually and quantitatively. Virtual US imaging was also performed on 3 virtual volumes with different arrangements of cardiomyocyte bundles. The trends in these evaluations were following our expectations and the geometric characteristic remained after virtual imaging, which validated that the volumes generated by our model have a similar effect to the realistic tissue during the imaging.

Perspectives

In the future, more efforts will be focused on more precise simulations of the tissue, simulation of the dynamic tissue during the cardiac cycle, simulations of more virtual imaging modalities and functional simulations.

The simulations were performed on the basis of two sets of synchrotron data. The tissues were selected in the middle part of the free wall along the radial direction because it exhibits a relatively describable arrangement, such as a parallel or branching structure, while the tissue located near the endocardium and epicardium is more difficult to describe. Thus, the simulations on these parts will be a focus. Besides, the virtual volume with a branching laminar structure was generated but not ideal. The deformation was achieved by displacing the control points, where each control point influences the whole

volume. Designing an adequate strategy for moving the control points will be extremely important to update the volume correctly during its deformation.

I used FFD to simulate the different states of tissue during the cardiac cycle. However, the states of the tissues in the heart depend on the phase during the cardiac cycle and the position they belong to inside the myocardium. Therefore, there are no precise assessments of the size of a cardiomyocyte bundle, which leads to only qualitative simulations. In the future, if the parameters of the variation of different parts of the myocardium can be precisely quantitatively assessed, it will be possible to use the proposed model to simulate the geometric shapes of various states during the cardiac cycle. Especially at Levels 2 and 3, a precise quantitative estimation of the geometry of the laminar structure makes it possible to build a 4D mathematical model describing the geometric variation in the 3D structure of the myocardium and one temporal dimension. Using these models and our proposed model, virtual volumes can be generated precisely at any moment during the cardiac cycle to investigate the relationships between the forces inside the tissue and structural variation.

For virtual US imaging, limited by the resolution of the US which is much lower than the μ-CT, the simulation can't be accomplished at a scale of the cardiomyocyte bundle. Thus, I can only perform the simulations above the scale of the sheetlet. In the future, more imaging modalities will be performed on our models, such as MRI. Similarly, functional simulations such as water diffusion simulations could be performed inside the generated volume and cardiomyocytes.

Author's publications

- **Wang, Z.**, Varray F, Magnin IE. A deformable heart model: multiscale description and virtual imaging simulation. *Computer methods and programs in biomedicine. Under review. 2022.*
- **Wang, Z.**, Varray F, Clarysse P, Magnin IE. Towards a multi-scale virtual heart model. *In 2020 15th IEEE International Conference on Signal Processing (ICSP) 2020 Dec 6 (Vol. 1, pp. 521-526). IEEE.*

Appendix

Appendix A

Class diagrams of objects in our model

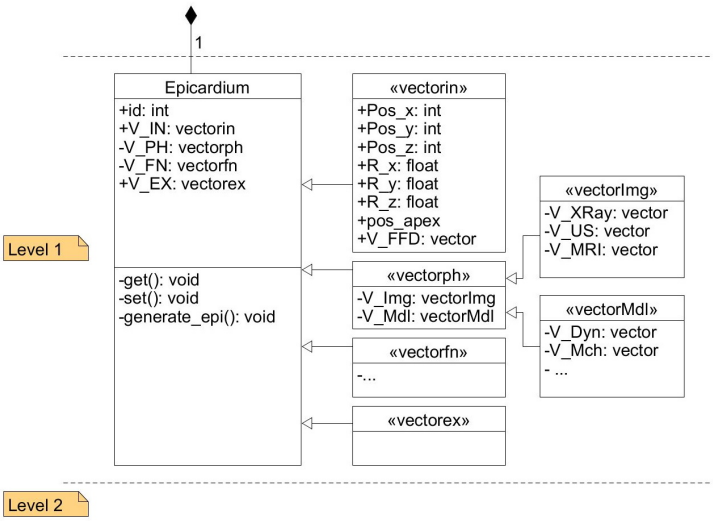

Figure A.1: *Class diagram of object "epicardium".*

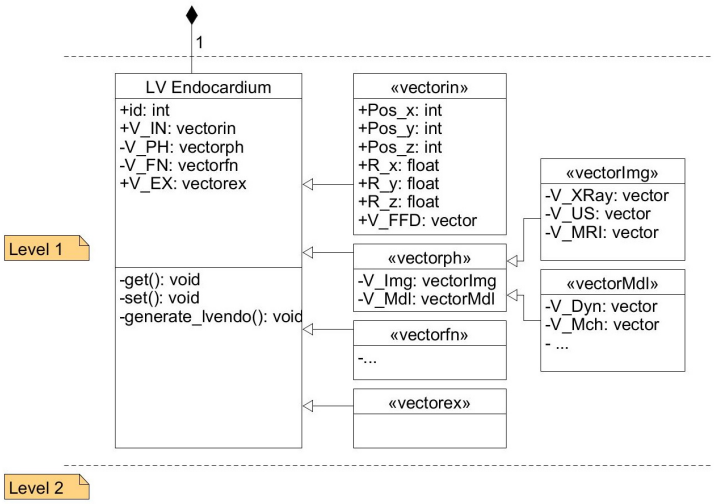

Figure A.2: *Class diagram of object "LV endocardium".*

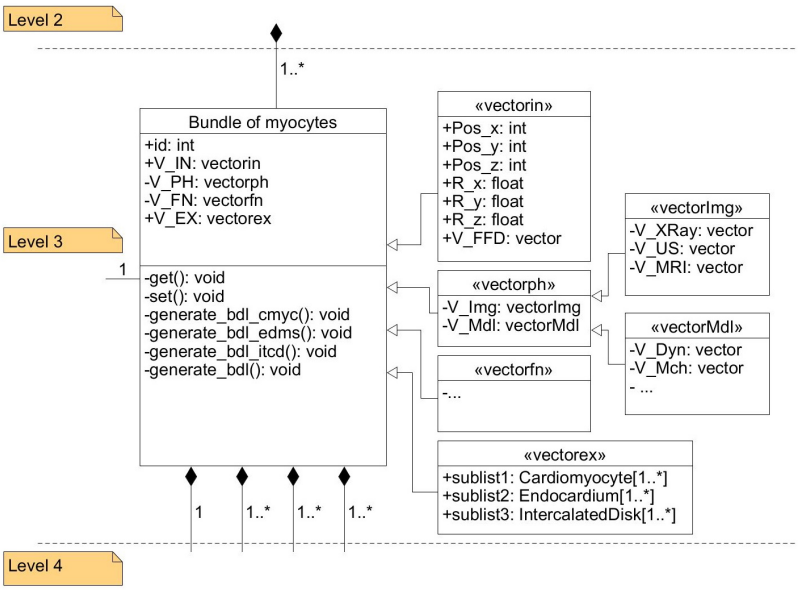

Figure A.3: *Class diagram of object "ventricular septum".*

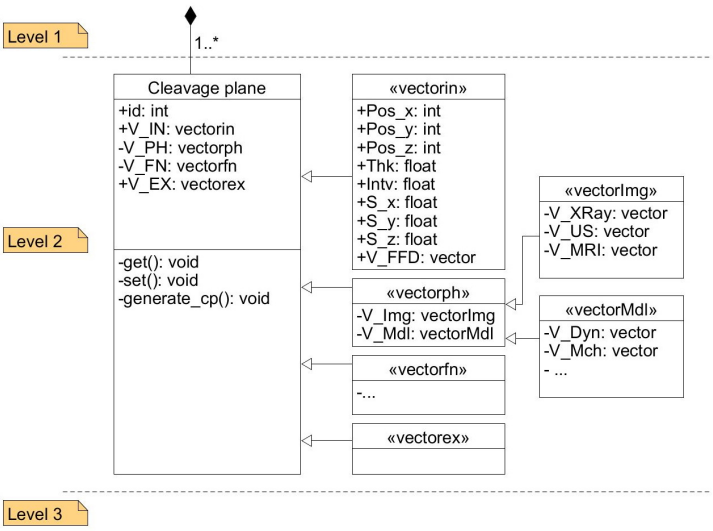

Figure A.4: *Class diagram of object "cleavage plane".*

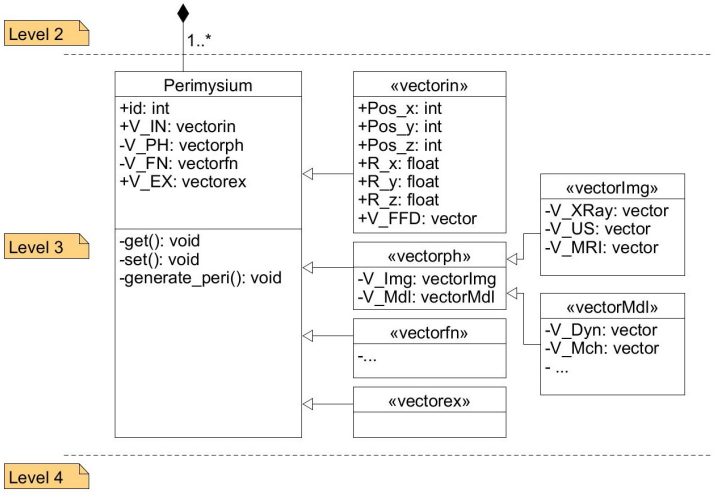

Figure A.5: *Class diagram of object "perimysium".*

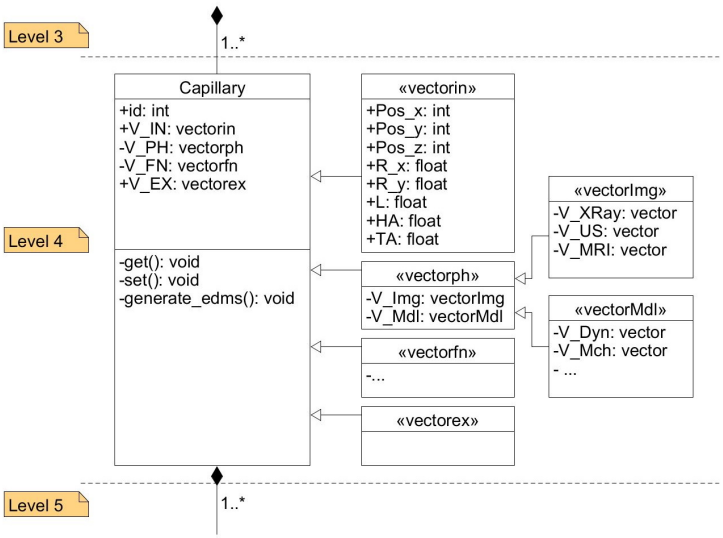

Figure A.6: *Class diagram of object "capillary".*

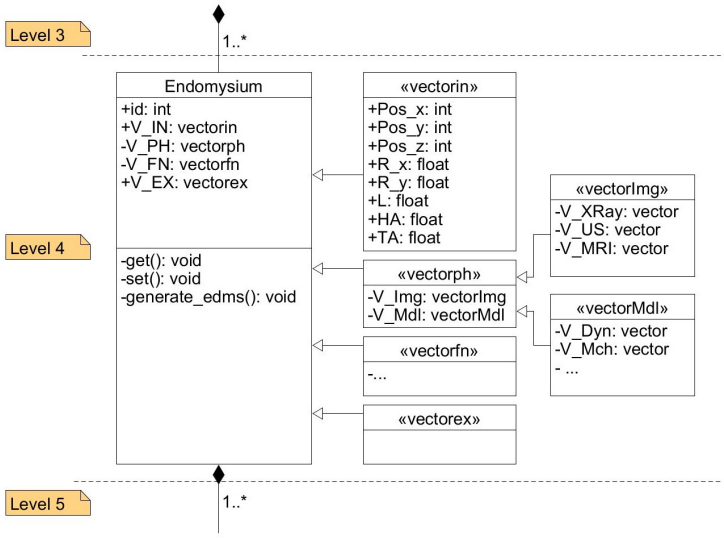

Figure A.7: *Class diagram of object "endomysium".*

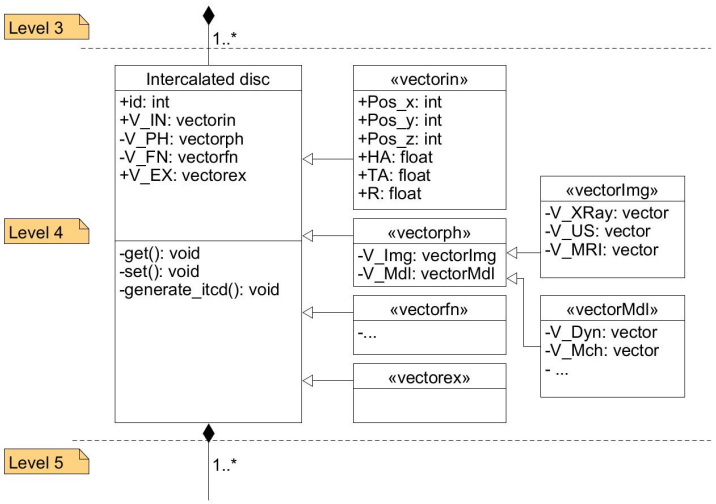

Figure A.8: *Class diagram of object "intercalated disc".*

Bibliography

[Abdi et al., 2007] Abdi, H. et al. (2007). The method of least squares. *Encyclopedia of measurement and statistics*, 1:530–532.

[Anderson et al., 2005] Anderson, R. H., Ho, S. Y., Redmann, K., Sanchez-Quintana, D., and Lunkenheimer, P. P. (2005). The anatomical arrangement of the myocardial cells making up the ventricular mass. *European journal of cardio-thoracic surgery*, 28(4):517–525.

[Anderson et al., 2004] Anderson, R. H., Razavi, R., and Taylor, A. M. (2004). Cardiac anatomy revisited. *Journal of anatomy*, 205(3):159–177.

[Ashikaga et al., 2008] Ashikaga, H., Coppola, B. A., Yamazaki, K. G., Villarreal, F. J., Omens, J. H., and Covell, J. W. (2008). Changes in regional myocardial volume during the cardiac cycle: implications for transmural blood flow and cardiac structure. *American Journal of Physiology-Heart and Circulatory Physiology*, 295(2):H610–H618.

[Aslanidi et al., 2012] Aslanidi, O. V., Nikolaidou, T., Zhao, J., Smaill, B. H., Gilbert, S. H., Holden, A. V., Lowe, T., Withers, P. J., Stephenson, R. S., Jarvis, J. C., et al. (2012). Application of micro-computed tomography with iodine staining to cardiac imaging, segmentation, and computational model development. *IEEE transactions on medical imaging*, 32(1):8–17.

[Axel et al., 2014] Axel, L., Wedeen, V. J., and Ennis, D. B. (2014). Probing dynamic myocardial microstructure with cardiac magnetic resonance diffusion tensor imaging.

[Ayari et al., 2017] Ayari, R., Abdallah, A. B., Ghorbel, F., and Bedoui, M. H. (2017). Analysis of regional deformation of the heart left ventricle. *IRBM*, 38(2):90–97.

[Bardinet et al., 1996] Bardinet, E., Cohen, L. D., and Ayache, N. (1996). Tracking and motion analysis of the left ventricle with deformable superquadrics. *Medical image analysis*, 1(2):129–149.

[Bardinet et al., 1998] Bardinet, E., Cohen, L. D., and Ayache, N. (1998). A parametric deformable model to fit unstructured 3d data. *Computer vision and image understanding*, 71(1):39–54.

[Barr, 1981a] Barr, A. (1981a). Superquadricsandangle-preservingdeformations. *IEEE Computer Graphics and Applications*, 1(1).

[Barr, 1981b] Barr, A. H. (1981b). Superquadrics and angle-preserving transformations. *IEEE Computer graphics and Applications*, 1(1):11–23.

[Barr, 1987] Barr, A. H. (1987). Global and local deformations of solid primitives. In *Readings in Computer Vision*, pages 661–670. Elsevier.

[Barros, 2019] Barros, V. N. (2019). The heart cycle: review. *MOJ Womens Health*, 8(1):66–69.

[Bhattacharyya, 1946] Bhattacharyya, A. (1946). On a measure of divergence between two multinomial populations. *Sankhyā: the indian journal of statistics*, pages 401–406.

[Bieniek and Moga, 2000] Bieniek, A. and Moga, A. (2000). An efficient watershed algorithm based on connected components. *Pattern recognition*, 33(6):907–916.

[Bozkurt, 2019] Bozkurt, S. (2019). Mathematical modeling of cardiac function to evaluate clinical cases in adults and children. *PloS one*, 14(10):e0224663.

[Braibant et al., 1985] Braibant, V., Fleury, C., and Beckers, P. (1985). Shape optimal design-an approach matching cad and optimization concepts. In *Optimization in Computer Aided Design: proceedings of the IFIP WG 5.2 Working Conference on Optimization in Computer-Aided Design, Lyon, France, 24-26 October, 1983*, pages 231–269. Elsevier North Holland.

[Breu et al., 1995] Breu, H., Gil, J., Kirkpatrick, D., and Werman, M. (1995). Linear time euclidean distance transform algorithms. *IEEE Transactions on Pattern Analysis and Machine Intelligence*, 17(5):529–533.

[Brutsaert, 1989] Brutsaert, D. L. (1989). The endocardium. *Annual review of physiology*, 51(1):263–273.

[Burton et al., 2006] Burton, R. A., Plank, G., Schneider, J. E., Grau, V., Ahammer, H., Keeling, S. L., Lee, J., Smith, N. P., Gavaghan, D., Trayanova, N., et al. (2006). Three-dimensional models of individual cardiac histoanatomy: tools and challenges. *Annals of the New York Academy of Sciences*, 1080:301.

[Caon, 2004] Caon, M. (2004). Voxel-based computational models of real human anatomy: a review. *Radiation and environmental biophysics*, 42(4):229–235.

[Carlton, 2011] Carlton, R. A. (2011). Polarized light microscopy. In *Pharmaceutical microscopy*, pages 7–64. Springer.

[Caulfield and Borg, 1979] Caulfield, J. and Borg, T. (1979). The collagen network of the heart. *Laboratory investigation; a journal of technical methods and pathology*, 40(3):364–372.

[Chalopin et al., 2001] Chalopin, C., Finet, G., and Magnin, I. E. (2001). Modeling the 3d coronary tree for labeling purposes. *Medical image analysis*, 5(4):301–315.

[Chen et al., 1994] Chen, C. W., Huang, T. S., and Arrott, M. (1994). Modeling, analysis, and visualization of left ventricle shape and motion by hierarchical decomposition. *IEEE Transactions on Pattern Analysis and Machine Intelligence*, 16(4):342–356.

[Chen et al., 1995] Chen, C. W., Luo, J., Parker, K. J., and Huang, T. S. (1995). Ct volumetric data-based left ventricle motion estimation: an integrated approach. *Computerized medical imaging and graphics*, 19(1):85–100.

[Chen et al., 2007] Chen, J., Shapiro, V., Suresh, K., and Tsukanov, I. (2007). Shape optimization with topological changes and parametric control. *International journal for numerical methods in engineering*, 71(3):313–346.

[Cheng et al., 2005] Cheng, A., Langer, F., Rodriguez, F., Criscione, J. C., Daughters, G. T., Miller, D. C., and Ingels Jr, N. B. (2005). Transmural sheet strains in the lateral wall of the ovine left ventricle. *American Journal of Physiology-Heart and Circulatory Physiology*, 289(3):H1234–H1241.

[Chevalier et al., 2003] Chevalier, L., Jaillet, F., and Baskurt, A. (2003). Segmentation and superquadric modeling of 3d objects. *Journal of WSCG*, 11(1-3).

[Cloetens et al., 1999] Cloetens, P., Ludwig, W., Baruchel, J., Van Dyck, D., Van Landuyt, J., Guigay, J., and Schlenker, M. (1999). Holotomography: Quantitative phase tomography with micrometer resolution using hard synchrotron radiation x rays. *Applied physics letters*, 75(19):2912–2914.

[Cohen and Cohen, 1993] Cohen, L. D. and Cohen, I. (1993). Finite-element methods for active contour models and balloons for 2-d and 3-d images. *IEEE Transactions on Pattern Analysis and machine intelligence*, 15(11):1131–1147.

[Costa et al., 1999] Costa, K. D., Takayama, Y., McCulloch, A. D., and Covell, J. W. (1999). Laminar fiber architecture and three-dimensional systolic mechanics in canine ventricular myocardium. *American Journal of Physiology-Heart and Circulatory Physiology*, 276(2):H595–H607.

[Davidović et al., 2020] Davidović, A., Coudière, Y., and Bourgault, Y. (2020). Modelling the action potential propagation in a heart with structural heterogeneities: From high-resolution mri to numerical simulations. *International journal for numerical methods in biomedical engineering*, page e3322.

[Dejea et al., 2017] Dejea, H., Garcia-Canadilla, P., Stampanoni, M., Zamora, M., Crispi, F., Bijnens, B., and Bonnin, A. (2017). Microstructural analysis of cardiac endomyocardial biopsies with synchrotron radiation-based x-ray phase contrast imaging. In *International Conference on Functional Imaging and Modeling of the Heart*, pages 23–31. Springer.

[Deng et al., 2012] Deng, D., Jiao, P., Ye, X., and Xia, L. (2012). An image-based model of the whole human heart with detailed anatomical structure and fiber orientation. *Computational and Mathematical Methods in Medicine*, 2012.

[Dössel et al., 2012] Dössel, O., Krueger, M. W., Weber, F. M., Wilhelms, M., and Seemann, G. (2012). Computational modeling of the human atrial anatomy and electrophysiology. *Medical & biological engineering & computing*, 50(8):773–799.

[Ebrahimi Nejad et al., 2017] Ebrahimi Nejad, S., Carey, J. P., McMurtry, M. S., and Hahn, J.-O. (2017). Model-based cardiovascular disease diagnosis: a preliminary in-silico study. *Biomechanics and modeling in mechanobiology*, 16(2):549–560.

[Fastl et al., 2018] Fastl, T. E., Tobon-Gomez, C., Crozier, A., Whitaker, J., Rajani, R., McCarthy, K. P., Sanchez-Quintana, D., Ho, S. Y., O'Neill, M. D., Plank, G., et al. (2018). Personalized computational modeling of left atrial geometry and transmural myofiber architecture. *Medical image analysis*, 47:180–190.

[Feldkamp et al., 1984] Feldkamp, L. A., Davis, L. C., and Kress, J. W. (1984). Practical cone-beam algorithm. *Josa a*, 1(6):612–619.

[Fernandez-Teran and Hurle, 1982] Fernandez-Teran, M. and Hurle, J. (1982). Myocardial fiber architecture of the human heart ventricles. *The Anatomical Record*, 204(2):137–147.

[Ferreira et al., 2014] Ferreira, P. F., Kilner, P. J., McGill, L.-A., Nielles-Vallespin, S., Scott, A. D., Ho, S. Y., McCarthy, K. P., Haba, M. M., Ismail, T. F., Gatehouse, P. D., et al. (2014). In vivo cardiovascular magnetic resonance diffusion tensor imaging shows evidence of abnormal myocardial laminar orientations and mobility in hypertrophic cardiomyopathy. *Journal of Cardiovascular Magnetic Resonance*, 16(1):1–16.

[Ferreira et al., 2015] Ferreira, V. M., Wijesurendra, R. S., Liu, A., Greiser, A., Casadei, B., Robson, M. D., Neubauer, S., and Piechnik, S. K. (2015). Systolic shmolli myocardial t1-mapping for improved robustness to partial-volume effects and applications in tachyarrhythmias. *Journal of Cardiovascular Magnetic Resonance*, 17(1):1–11.

[Gilbert et al., 2007] Gilbert, S. H., Benson, A. P., Li, P., and Holden, A. V. (2007). Regional localisation of left ventricular sheet structure: integration with current models of cardiac fibre, sheet and band structure. *European journal of cardio-thoracic surgery*, 32(2):231–249.

[Goblot et al., 2016] Goblot, D., Pop, M., and Siddiqi, K. (2016). Cartan frame analysis of hearts with infarcts. In *International Workshop on Statistical Atlases and Computational Models of the Heart*, pages 87–95. Springer.

[Göktepe et al., 2010] Göktepe, S., Abilez, O. J., Parker, K. K., and Kuhl, E. (2010). A multiscale model for eccentric and concentric cardiac growth through sarcomerogenesis. *Journal of theoretical biology*, 265(3):433–442.

[Guccione et al., 1991] Guccione, J. M., McCulloch, A. D., and Waldman, L. (1991). Passive material properties of intact ventricular myocardium determined from a cylindrical model. *Journal of Biomechanical Engineering*, 113:42–55.

[Hakman and Groth, 1999] Hakman, M. and Groth, T. (1999). Object-oriented biomedical system modeling—the rationale. *Computer methods and programs in biomedicine*, 59(1):1–17.

[Harrild and Henriquez, 2000] Harrild, D. M. and Henriquez, C. S. (2000). A computer model of normal conduction in the human atria. *Circulation research*, 87(7):e25–e36.

[Harrington et al., 2005] Harrington, K. B., Rodriguez, F., Cheng, A., Langer, F., Ashikaga, H., Daughters, G. T., Criscione, J. C., Ingels, N. B., and Miller, D. C. (2005). Direct measurement of transmural laminar architecture in the anterolateral wall of the ovine left ventricle: new implications for wall thickening mechanics. *American Journal of Physiology-Heart and Circulatory Physiology*, 288(3):H1324–H1330.

[Hartwig, 1976] Hartwig, R. E. (1976). Singular value decomposition and the moore–penrose inverse of bordered matrices. *SIAM Journal on Applied Mathematics*, 31(1):31–41.

[Helm et al., 2005] Helm, P. A., Tseng, H.-J., Younes, L., McVeigh, E. R., and Winslow, R. L. (2005). Ex vivo 3d diffusion tensor imaging and quantification of cardiac laminar

structure. *Magnetic Resonance in Medicine: An Official Journal of the International Society for Magnetic Resonance in Medicine*, 54(4):850–859.

[Herrling et al., 2017] Herrling, M. P., Weisbrodt, J., Kirkland, C. M., Williamson, N. H., Lackner, S., Codd, S. L., Seymour, J. D., Guthausen, G., and Horn, H. (2017). Nmr investigation of water diffusion in different biofilm structures. *Biotechnology and bioengineering*, 114(12):2857–2867.

[Ho, 2009] Ho, S. Y. (2009). Anatomy and myoarchitecture of the left ventricular wall in normal and in disease. *European Journal of Echocardiography*, 10(8):iii3–iii7.

[Ho et al., 2002] Ho, S. Y., Anderson, R. H., and Sánchez-Quintana, D. (2002). Atrial structure and fibres: morphologic bases of atrial conduction. *Cardiovascular research*, 54(2):325–336.

[Hort, 1957a] Hort, W. (1957a). Mikrometrische untersuchungen an verschieden weiten meerschweinchenherzen. In *KLINISCHE WOCHENSCHRIFT*, volume 35, pages 698–698. SPRINGER VERLAG 175 FIFTH AVE, NEW YORK, NY 10010.

[Hort, 1957b] Hort, W. (1957b). Untersuchungen über die muskelfaserdehnung und das gefüge des myokards in der rechten herzkammerwand des meerschweinchens. *Virchows Archiv für pathologische Anatomie und Physiologie und für klinische Medizin*, 329(6):694–731.

[Iyer et al., 2004] Iyer, V., Mazhari, R., and Winslow, R. L. (2004). A computational model of the human left-ventricular epicardial myocyte. *Biophysical journal*, 87(3):1507–1525.

[Jaklic et al., 2000] Jaklic, A., Leonardis, A., Solina, F., and Solina, F. (2000). *Segmentation and recovery of superquadrics*, volume 20. Springer Science & Business Media.

[Jayadevappa et al., 2011] Jayadevappa, D., Srinivas Kumar, S., and Murty, D. (2011). Medical image segmentation algorithms using deformable models: a review. *IETE Technical review*, 28(3):248–255.

[Jensen and Svendsen, 1992] Jensen, J. and Svendsen, N. B. (1992). Calculation of pressure fields from arbitrarily shaped, apodized, and excited ultrasound transducers. *IEEE Trans. Ultrason., Ferroelec., Freq. Contr.*, pages 262–267.

[Jouk et al., 2018] Jouk, P.-S., Truong, B. L., Michalowicz, G., and Usson, Y. (2018). Postnatal myocardium remodelling generates inhomogeneity in the architecture of the ventricular mass. *Surgical and Radiologic Anatomy*, 40(1):75–83.

[Jouk et al., 2000] Jouk, P.-S., Usson, Y., Michalowicz, G., and Grossi, L. (2000). Three-dimensional cartography of the pattern of the myofibres in the second trimester fetal human heart. *Anatomy and embryology*, 202(2):103–118.

[Kanzaki et al., 2010] Kanzaki, Y., Terasaki, F., Okabe, M., Fujita, S., Katashima, T., Otsuka, K., and Ishizaka, N. (2010). Three-dimensional architecture of cardiomyocytes and connective tissue in human heart revealed by scanning electron microscopy.

[Kass et al., 1988] Kass, M., Witkin, A., and Terzopoulos, D. (1988). Snakes: Active contour models. *International journal of computer vision*, 1(4):321–331.

[Ko et al., 2019] Ko, S. M., Hwang, S. H., and Lee, H.-J. (2019). Role of cardiac computed tomography in the diagnosis of left ventricular myocardial diseases. *Journal of Cardiovascular Imaging*, 27(2):73–92.

[Kocica et al., 2006] Kocica, M. J., Corno, A. F., Carreras-Costa, F., Ballester-Rodes, M., Moghbel, M. C., Cueva, C. N., Lackovic, V., Kanjuh, V. I., and Torrent-Guasp, F. (2006). The helical ventricular myocardial band: global, three-dimensional, functional architecture of the ventricular myocardium. *European journal of cardio-thoracic surgery*, 29(Supplement_1):S21–S40.

[Kosta et al., 2017] Kosta, S., Negroni, J., Lascano, E., and Dauby, P. (2017). Multiscale model of the human cardiovascular system: Description of heart failure and comparison of contractility indices. *Mathematical biosciences*, 284:71–79.

[Kostas et al., 2015] Kostas, K., Ginnis, A., Politis, C., and Kaklis, P. (2015). Ship-hull shape optimization with a t-spline based bem–isogeometric solver. *Computer Methods in Applied Mechanics and Engineering*, 284:611–622.

[Lamata et al., 2014] Lamata, P., Casero, R., Carapella, V., Niederer, S. A., Bishop, M. J., Schneider, J. E., Kohl, P., and Grau, V. (2014). Images as drivers of progress in cardiac

computational modelling. *Progress in Biophysics and Molecular Biology*, 115(2-3):198–212.

[Lang et al., 2012] Lang, R. M., Badano, L. P., Tsang, W., Adams, D. H., Agricola, E., Buck, T., Faletra, F. F., Franke, A., Hung, J., de Isla, L. P., et al. (2012). Eae/ase recommendations for image acquisition and display using three-dimensional echocardiography. *European Heart Journal–Cardiovascular Imaging*, 13(1):1–46.

[LeGrice et al., 2001] LeGrice, I., Hunter, P., Young, A., and Smaill, B. (2001). The architecture of the heart: a data–based model. *Philosophical Transactions of the Royal Society of London. Series A: Mathematical, Physical and Engineering Sciences*, 359(1783):1217–1232.

[LeGrice et al., 2005] LeGrice, I., Pope, A., and Smaill, B. (2005). The architecture of the heart: myocyte organization and the cardiac extracellular matrix. In *Interstitial Fibrosis in Heart Failure*, pages 3–21. Springer.

[LeGrice et al., 1995a] LeGrice, I., Takayama, Y., and Covell, J. (1995a). Transverse shear along myocardial cleavage planes provides a mechanism for normal systolic wall thickening. *Circulation research*, 77(1):182–193.

[LeGrice et al., 1997] LeGrice, I. J., Hunter, P. J., and Smaill, B. (1997). Laminar structure of the heart: a mathematical model. *American Journal of Physiology-Heart and Circulatory Physiology*, 272(5):H2466–H2476.

[LeGrice et al., 1995b] LeGrice, I. J., Smaill, B., Chai, L., Edgar, S., Gavin, J., and Hunter, P. J. (1995b). Laminar structure of the heart: ventricular myocyte arrangement and connective tissue architecture in the dog. *American Journal of Physiology-Heart and Circulatory Physiology*, 269(2):H571–H582.

[Lin and Alessio, 2009] Lin, E. and Alessio, A. (2009). What are the basic concepts of temporal, contrast, and spatial resolution in cardiac CT. *Journal of cardiovascular computed tomography*, 3(6):403–408.

[Lopez-Perez et al., 2015] Lopez-Perez, A., Sebastian, R., and Ferrero, J. M. (2015). Three-dimensional cardiac computational modelling: methods, features and applications. *Biomedical engineering online*, 14(1):1–31.

[Lorenz and von Berg, 2006] Lorenz, C. and von Berg, J. (2006). A comprehensive shape model of the heart. *Medical image analysis*, 10(4):657–670.

[Lötjönen et al., 2005] Lötjönen, J., Pollari, M., Kivistö, S., and Lauerma, K. (2005). Correction of motion artifacts from cardiac cine magnetic resonance images1. *Academic radiology*, 12(10):1273–1284.

[Männer et al., 2001] Männer, J., Perez-Pomares, J., Macias, D., and Munoz-Chapuli, R. (2001). The origin, formation and developmental significance of the epicardium: a review. *Cells Tissues Organs*, 169(2):89–103.

[McInerney and Terzopoulos, 1995] McInerney, T. and Terzopoulos, D. (1995). A dynamic finite element surface model for segmentation and tracking in multidimensional medical images with application to cardiac 4d image analysis. *Computerized medical imaging and graphics*, 19(1):69–83.

[McInerney and Terzopoulos, 1996] McInerney, T. and Terzopoulos, D. (1996). Deformable models in medical image analysis: a survey. *Medical image analysis*, 1(2):91–108.

[Mendis et al., 2011] Mendis, S., Puska, P., Norrving, B., Organization, W. H., et al. (2011). *Global atlas on cardiovascular disease prevention and control*. World Health Organization.

[Miller et al., 1991] Miller, J. V., Breen, D. E., Lorensen, W. E., O'Bara, R. M., and Wozny, M. J. (1991). Geometrically deformed models: a method for extracting closed geometric models form volume data. *ACM SIGGRAPH Computer Graphics*, 25(4):217–226.

[Mirea, 2017] Mirea, I. (2017). *Analyse de la microstructure 3D du tissu cardiaque humain à l'aide de la micro-tomographie à rayons X par contraste de phase*. PhD thesis, Lyon.

[Mirea et al., 2015] Mirea, I., Varray, F., Zhu, Y. M., Fanton, L., Langer, M., Jouk, P.-S., Michalowicz, G., Usson, Y., and Magnin, I. E. (2015). Very high-resolution imaging of post-mortem human cardiac tissue using x-ray phase contrast tomography. In *International Conference on Functional Imaging and Modeling of the Heart*, pages 172–179. Springer.

[Mirea et al., 2016] Mirea, I., Wang, L., Varray, F., Zhu, Y.-M., Serrano, E. D., and Magnin, I. E. (2016). Statistical analysis of transmural laminar microarchitecture of the human left ventricle. In *2016 IEEE 13th International Conference on Signal Processing (ICSP)*, pages 53–56. IEEE.

[Moës et al., 1999] Moës, N., Dolbow, J., and Belytschko, T. (1999). A finite element method for crack growth without remeshing. *International journal for numerical methods in engineering*, 46(1):131–150.

[Molléro et al., 2016] Molléro, R., Pennec, X., Delingette, H., Ayache, N., and Sermesant, M. (2016). A multiscale cardiac model for fast personalisation and exploitation. In *International conference on medical image computing and computer-assisted intervention*, pages 174–182. Springer.

[Mondillo et al., 2011] Mondillo, S., Galderisi, M., Mele, D., Cameli, M., Lomoriello, V. S., Zacà, V., Ballo, P., D'Andrea, A., Muraru, D., Losi, M., et al. (2011). Speckle-tracking echocardiography: a new technique for assessing myocardial function. *Journal of Ultrasound in Medicine*, 30(1):71–83.

[Nerlekar et al., 2018] Nerlekar, N., Ha, F. J., Cheshire, C., Rashid, H., Cameron, J. D., Wong, D. T., Seneviratne, S., and Brown, A. J. (2018). Computed tomographic coronary angiography–derived plaque characteristics predict major adverse cardiovascular events: a systematic review and meta-analysis. *Circulation: Cardiovascular Imaging*, 11(1):e006973.

[Niederer et al., 2009] Niederer, S., Rhode, K., Razavi, R., and Smith, N. (2009). The importance of model parameters and boundary conditions in whole organ models of cardiac contraction. In *International Conference on Functional Imaging and Modeling of the Heart*, pages 348–356. Springer.

[Nielles-Vallespin et al., 2017] Nielles-Vallespin, S., Khalique, Z., Ferreira, P. F., de Silva, R., Scott, A. D., Kilner, P., McGill, L.-A., Giannakidis, A., Gatehouse, P. D., Ennis, D., et al. (2017). Assessment of myocardial microstructural dynamics by in vivo diffusion tensor cardiac magnetic resonance. *Journal of the American College of Cardiology*, 69(6):661–676.

[Nielsen et al., 1991] Nielsen, P., Le Grice, I., Smaill, B., and Hunter, P. (1991). Mathematical model of geometry and fibrous structure of the heart. *American Journal of Physiology-Heart and Circulatory Physiology*, 260(4):H1365–H1378.

[Paganin et al., 2002] Paganin, D., Mayo, S. C., Gureyev, T. E., Miller, P. R., and Wilkins, S. W. (2002). Simultaneous phase and amplitude extraction from a single defocused image of a homogeneous object. *Journal of microscopy*, 206(1):33–40.

[Palit et al., 2015] Palit, A., Bhudia, S. K., Arvanitis, T. N., Turley, G. A., and Williams, M. A. (2015). Computational modelling of left-ventricular diastolic mechanics: Effect of fibre orientation and right-ventricle topology. *Journal of biomechanics*, 48(4):604–612.

[Park et al., 1996] Park, J., Metaxas, D., and Axel, L. (1996). Analysis of left ventricular wall motion based on volumetric deformable models and mri-spamm. *Center for Human Modeling and Simulation*, page 99.

[Park et al., 2002] Park, K., Metaxas, D. N., and Axel, L. (2002). Lv-rv shape modeling based on a blended parameterized model. In *International Conference on Medical Image Computing and Computer-Assisted Intervention*, pages 753–761. Springer.

[Parvizian et al., 2007] Parvizian, J., Düster, A., and Rank, E. (2007). Finite cell method. *Computational Mechanics*, 41(1):121–133.

[Peate, 2021] Peate, I. (2021). The heart: an amazing organ. *British Journal of Healthcare Assistants*, 15(2):72–77.

[Peebles, 2013] Peebles, C. (2013). The year in cardiology 2012: imaging, computed tomography, and cardiovascular magnetic resonance. *European heart journal*, 34(4):310–313.

[Plotkowiak et al., 2008] Plotkowiak, M., Rodriguez, B., Plank, G., Schneider, J. E., Gavaghan, D., Kohl, P., and Grau, V. (2008). High performance computer simulations of cardiac electrical function based on high resolution MRI datasets. In *International Conference on Computational Science*, pages 571–580. Springer.

[Pope et al., 2008] Pope, A. J., Sands, G. B., Smaill, B. H., and LeGrice, I. J. (2008). Three-dimensional transmural organization of perimysial collagen in the heart. *American Journal of Physiology-Heart and Circulatory Physiology*, 295(3):H1243–H1252.

[Quarteroni et al., 2017] Quarteroni, A., Lassila, T., Rossi, S., and Ruiz-Baier, R. (2017). Integrated heart—coupling multiscale and multiphysics models for the simulation of the cardiac function. *Computer Methods in Applied Mechanics and Engineering*, 314:345–407.

[Rich and Khan, 2021] Rich, N. L. and Khan, Y. S. (2021). Anatomy, thorax, heart papillary muscles. In *StatPearls [Internet]*. StatPearls Publishing.

[Rit et al., 2014] Rit, S., Oliva, M. V., Brousmiche, S., Labarbe, R., Sarrut, D., and Sharp, G. C. (2014). The Reconstruction Toolkit (RTK), an open-source cone-beam CT reconstruction toolkit based on the Insight Toolkit (ITK). In *Journal of Physics: Conference Series*, volume 489, page 012079. IOP Publishing.

[Robb and Robb, 1942] Robb, J. S. and Robb, R. C. (1942). The normal heart: anatomy and physiology of the structural units. *American Heart Journal*, 23(4):455–467.

[Robinson et al., 1988] Robinson, T. F., Geraci, M. A., Sonnenblick, E. H., and Factor, S. M. (1988). Coiled perimysial fibers of papillary muscle in rat heart: morphology, distribution, and changes in configuration. *Circulation research*, 63(3):577–592.

[Sederberg and Parry, 1986] Sederberg, T. W. and Parry, S. R. (1986). Free-form deformation of solid geometric models. In *Proceedings of the 13th annual conference on Computer graphics and interactive techniques*, pages 151–160.

[Sermesant et al., 2007] Sermesant, M., Konukoglu, E., Delingette, H., Coudiere, Y., Chinchapatnam, P., Rhode, K. S., Razavi, R., and Ayache, N. (2007). An anisotropic multi-front fast marching method for real-time simulation of cardiac electrophysiology. In *International Conference on Functional Imaging and Modeling of the Heart*, pages 160–169. Springer.

[Shaaban et al., 2020] Shaaban, A. M., Anitescu, C., Atroshchenko, E., and Rabczuk, T. (2020). Shape optimization by conventional and extended isogeometric boundary ele-

ment method with pso for two-dimensional helmholtz acoustic problems. *Engineering Analysis with Boundary Elements*, 113:156–169.

[Simões and Riley, 2018] Simões, F. C. and Riley, P. R. (2018). The ontogeny, activation and function of the epicardium during heart development and regeneration. *Development*, 145(7):dev155994.

[Smerup et al., 2009] Smerup, M., Nielsen, E., Agger, P., Frandsen, J., Vestergaard-Poulsen, P., Andersen, J., Nyengaard, J., Pedersen, M., Ringgaard, S., Hjortdal, V., et al. (2009). The three-dimensional arrangement of the myocytes aggregated together within the mammalian ventricular myocardium. *The Anatomical Record: Advances in Integrative Anatomy and Evolutionary Biology: Advances in Integrative Anatomy and Evolutionary Biology*, 292(1):1–11.

[Smith et al., 2004] Smith, N., Nickerson, D., Crampin, E., and Hunter, P. (2004). Multi-scale computational modelling of the heart. *Acta Numerica*, 13:371.

[Soghrati et al., 2012] Soghrati, S., Aragón, A. M., Armando Duarte, C., and Geubelle, P. H. (2012). An interface-enriched generalized fem for problems with discontinuous gradient fields. *International Journal for Numerical Methods in Engineering*, 89(8):991–1008.

[Staib and Duncan, 1992] Staib, L. H. and Duncan, J. S. (1992). Boundary finding with parametrically deformable models. *IEEE transactions on pattern analysis and machine intelligence*, 14(11):1061–1075.

[Štern et al., 2011] Štern, D., Likar, B., Pernuš, F., and Vrtovec, T. (2011). Parametric modelling and segmentation of vertebral bodies in 3d ct and mr spine images. *Physics in Medicine & Biology*, 56(23):7505.

[Streeter Jr, 2005] Streeter Jr, D. (2005). Gross morphology and fiber geometry of the heart. *Handbook of Physiology. Section*, 2:617112.

[Suzuki and Kikuchi, 1991] Suzuki, K. and Kikuchi, N. (1991). A homogenization method for shape and topology optimization. *Computer methods in applied mechanics and engineering*, 93(3):291–318.

[Sylva et al., 2014] Sylva, M., van den Hoff, M. J., and Moorman, A. F. (2014). Development of the human heart. *American Journal of Medical Genetics Part A*, 164(6):1347–1371.

[Tay et al., 2009] Tay, P. C., Li, B., Garson, C. D., Acton, S. T., and Hossack, J. A. (2009). Left ventricle segmentation using model fitting and active surfaces. *Journal of signal processing systems*, 55(1):139–156.

[Ten Tusscher et al., 2007] Ten Tusscher, K. H., Hren, R., and Panfilov, A. V. (2007). Organization of ventricular fibrillation in the human heart. *Circulation research*, 100(12):e87–e101.

[Terzopoulos et al., 1987] Terzopoulos, D. et al. (1987). On matching deformable models to images. In *Topical Meeting on Machine Vision Tech. Digest Series*, volume 12, pages 160–167.

[Torrent-Guasp, 1975] Torrent-Guasp, F. (1975). Organizacion de la musculatura cardiaca ventricular. *Zarco P., Perez J.(eds) El Fallo Mecanico del Corazon*, pages 3–36.

[Torrent-Guasp et al., 2005] Torrent-Guasp, F., Kocica, M. J., Corno, A. F., Komeda, M., Carreras-Costa, F., Flotats, A., Cosin-Aguillar, J., and Wen, H. (2005). Towards new understanding of the heart structure and function. *European journal of cardio-thoracic surgery*, 27(2):191–201.

[Treuting et al., 2017] Treuting, P. M., Dintzis, S., and Montine, K. S. (2017). *Comparative anatomy and histology: a mouse, rat, and human atlas*. Academic Press.

[Turquin et al., 2019] Turquin, E., Petrusca, L., Viallon, M., Liebgott, H., and Varray, F. (2019). Full 3D anisotropic estimation of tissue in ultrasound imaging. In *2019 IEEE International Ultrasonics Symposium (IUS)*, pages 56–59.

[Upadhyay et al., 2021] Upadhyay, B. D., Sonigra, S. S., and Daxini, S. D. (2021). Numerical analysis perspective in structural shape optimization: A review post 2000. *Advances in Engineering Software*, 155:102992.

[Vadakkumpadan et al., 2010] Vadakkumpadan, F., Arevalo, H., Prassl, A. J., Chen, J., Kickinger, F., Kohl, P., Plank, G., and Trayanova, N. (2010). Image-based models of

cardiac structure in health and disease. *Wiley Interdisciplinary Reviews: Systems Biology and Medicine*, 2(4):489–506.

[Van den Broek and Van den Broek, 1980] Van den Broek, J. and Van den Broek, M. (1980). Application of an ellipsoidal heart model in studying left ventricular contractions. *Journal of Biomechanics*, 13(6):493–503.

[Van Loan, 1976] Van Loan, C. F. (1976). Generalizing the singular value decomposition. *SIAM Journal on numerical Analysis*, 13(1):76–83.

[Varray et al., 2017] Varray, F., Mirea, I., Langer, M., Peyrin, F., Fanton, L., and Magnin, I. E. (2017). Extraction of the 3D local orientation of myocytes in human cardiac tissue using X-ray phase-contrast micro-tomography and multi-scale analysis. *Medical image analysis*, 38:117–132.

[Varray et al., 2013] Varray, F., Wang, L., Fanton, L., Zhu, Y.-M., and Magnin, I. E. (2013). High resolution extraction of local human cardiac fibre orientations. In *International Conference on Functional Imaging and Modeling of the Heart*, pages 150–157. Springer.

[Vedaldi and Fulkerson, 2010] Vedaldi, A. and Fulkerson, B. (2010). Vlfeat: An open and portable library of computer vision algorithms. In *Proceedings of the 18th ACM international conference on Multimedia*, pages 1469–1472.

[Vedula et al., 2016] Vedula, V., Seo, J.-H., Lardo, A. C., and Mittal, R. (2016). Effect of trabeculae and papillary muscles on the hemodynamics of the left ventricle. *Theoretical and Computational Fluid Dynamics*, 30(1):3–21.

[Vetter and McCulloch, 1998] Vetter, F. J. and McCulloch, A. D. (1998). Three-dimensional analysis of regional cardiac function: a model of rabbit ventricular anatomy. *Progress in biophysics and molecular biology*, 69(2-3):157–183.

[Vigmond et al., 2001] Vigmond, E. J., Ruckdeschel, R., and Trayanova, N. (2001). Reentry in a morphologically realistic atrial model. *Journal of cardiovascular electrophysiology*, 12(9):1046–1054.

[Wall et al., 2008] Wall, W. A., Frenzel, M. A., and Cyron, C. (2008). Isogeometric structural shape optimization. *Computer methods in applied mechanics and engineering*, 197(33-40):2976–2988.

[Wang et al., 1995] Wang, K., Ho, S. Y., Gibson, D. G., and Anderson, R. H. (1995). Architecture of atrial musculature in humans. *Heart*, 73(6):559–565.

[Wang et al., 2019] Wang, S., Mirea, I., Varray, F., Liu, W.-Y., and Magnin, I. E. (2019). Investigating the 3d local myocytes arrangement in the human lv mid-wall with the transverse angle. In *International Conference on Functional Imaging and Modeling of the Heart*, pages 208–216. Springer.

[Wang et al., 2020] Wang, Z., Varray, F., Clarysse, P., and Magnin, I. E. (2020). Towards a multi-scale virtual heart model. In *2020 15th IEEE International Conference on Signal Processing (ICSP)*, volume 1, pages 521–526. IEEE.

[Weinhaus and Roberts, 2005] Weinhaus, A. J. and Roberts, K. P. (2005). Anatomy of the human heart. In *Handbook of cardiac anatomy, physiology, and devices*, pages 51–79. Springer.

[Weitkamp et al., 2011] Weitkamp, T., Haas, D., Wegrzynek, D., and Rack, A. (2011). Ankaphase: software for single-distance phase retrieval from inline x-ray phase-contrast radiographs. *Journal of synchrotron radiation*, 18(4):617–629.

[Whiteman et al., 2021] Whiteman, S., Alimi, Y., Carrasco, M., Gielecki, J., Zurada, A., and Loukas, M. (2021). Anatomy of the cardiac chambers: A review of the left ventricle. *Translational Research in Anatomy*, 23:100095.

[Winslow et al., 2012] Winslow, R. L., Trayanova, N., Geman, D., and Miller, M. I. (2012). Computational medicine: translating models to clinical care. *Science translational medicine*, 4(158):158rv11–158rv11.

[with superquadrics: an overview, 1994] with superquadrics: an overview, M. (1994). Modeling with superquadrics: an overview. In *Conference on software in telecommunications and computer networks*, pages 239–248.

[Wojciech et al., 2016] Wojciech, M., Karolczak, M. A., et al. (2016). Physiological basis in the assessment of myocardial mechanics using speckle-tracking echocardiography 2d. part i. *Journal of Ultrasonography*, 16(65):135–144.

[Xiao et al., 2014] Xiao, Y., Zhang, B., Liu, H., Miklas, J. W., Gagliardi, M., Pahnke, A., Thavandiran, N., Sun, Y., Simmons, C., Keller, G., et al. (2014). Microfabricated perfusable cardiac biowire: a platform that mimics native cardiac bundle. *Lab on a Chip*, 14(5):869–882.

[Yang et al., 2017] Yang, D., Wu, P., Tan, C., Pohl, K. M., Axel, L., and Metaxas, D. (2017). 3d motion modeling and reconstruction of left ventricle wall in cardiac mri. In *International Conference on Functional Imaging and Modeling of the Heart*, pages 481–492. Springer.

[Yang et al., 2006] Yang, G., Toumoulin, C., Coatrieux, J.-L., Shu, H., Luo, L., and Boulmier, D. (2006). A 3D static heart model from a MSCT data set. In *2005 IEEE Engineering in Medicine and Biology 27th Annual Conference*, pages 5499–5502. IEEE.

[Zhao et al., 2012] Zhao, J., Butters, T. D., Zhang, H., Pullan, A. J., LeGrice, I. J., Sands, G. B., and Smaill, B. H. (2012). An image-based model of atrial muscular architecture: effects of structural anisotropy on electrical activation. *Circulation: Arrhythmia and Electrophysiology*, 5(2):361–370.

[Zhao et al., 2017] Zhao, J., Hansen, B. J., Wang, Y., Csepe, T. A., Sul, L. V., Tang, A., Yuan, Y., Li, N., Bratasz, A., Powell, K. A., et al. (2017). Three-dimensional integrated functional, structural, and computational mapping to define the structural "fingerprints" of heart-specific atrial fibrillation drivers in human heart ex vivo. *Journal of the American Heart Association*, 6(8):e005922.

[Zhu et al., 2005] Zhu, J., Zhao, S., Ye, Y., and Wang, G. (2005). Computed tomography simulation with superquadrics. *Medical physics*, 32(10):3136–3143.

FOLIO ADMINISTRATIF

THESE DE L'INSA LYON, MEMBRE DE L'UNIVERSITE DE LYON

NOM: WANG

DATE de SOUTENANCE : 12/12/2022

Prénoms: Zexian

TITRE: A 3D multiscale synthetic model of biological tissue for virtual imaging

NATURE: Doctorat

Numéro d'ordre : 2022ISAL0114

Ecole doctorale: MÉCANIQUE, ÉNERGÉTIQUE, GÉNIE CIVIL, ACOUSTIQUE(MEGA) – EDA 162

Spécialité : Acoustique / Traitement du Signal et de l'Image

RESUME : Cette thèse a pour objectif de présenter un modèle déformable tridimensionnel multi-échelle afin de générer un cœur synthétique qui sera utilisé en recherche médicale et en particulier, en imagerie virtuelle. Le modèle décrit les formes géométriques et les caractéristiques des objets élémentaires du cœur à différentes échelles. Sa structure hiérarchique comprend cinq niveaux pour passant de la macro- à la micro-échelle. Chaque élément constitutif du cœur virtuel a une description orientée objet ou tous les paramètres spécifiques de chaque objet sont enregistrés dans un vecteur de caractéristiques. Le modèle est divisé en 2 parties : le modèle basse résolution (niveau 1) et le modèle haute résolution (niveaux 2, 3 et 4). En observant divers types d'imagerie expérimental de tissus cardiaques, des modèles de formes géométriques de base sont construits pour décrire les objets de chaque niveau. De plus, pour obtenir une simulation plus précise, la technique Déformation Libre (Free-Form Deformation, FFD) est utilisée pour déformer chaque objet afin d'améliorer le réalisme de notre modèle.
Dans le modèle basse résolution, basé sur les données de l'imagerie par lumière polarisée, des modèles de surface de l'endocarde, de l'épicarde et de l'épicarde partiels du ventricule gauche sont construits à l'aide du modèle de superellipsoïde, modifié par la FFD. Pour le modèle haute résolution, les formes de base des cardiomyocytes, des groupes de cardiomyocytes et des feuillet lamellaires de cardiomyocytes sont d'abord construites. En utilisant la FFD, il a été possible d'obtenir des formes plus réalistes ainsi que de générer la déformation du tissu à l'échelle microscopique durant un cycle cardiaque. Pour valider le modèle, des données synchrotron sont utilisées pour évaluer les paramètres géométriques du tissu myocardique avec une structure laminaire parallèle. En utilisant ces paramètres issus de données réelle, des volumes virtuels de tissu myocardique sont générés suivi d'une imagerie virtuelle. En comparant les orientations du tissu dans le volume virtuel et le volume reconstruit à partir de celui-ci dans diverses situations de bruit, cette stratégie montre que les volumes générés par notre modèle ont des caractéristiques similaires à celui du tissu initial, ce qui valide notre modèle.

MOTS-CLÉS : Modélisation multi-échelle, tissu cardiaque, modèle géométrique, modèle déformable, imagerie virtuelle

Laboratoire (s) de recherche : CREATIS

Directeur de thèse: François VARRAY

Président de jury :

Composition du jury : RAMALLI Alessandro (rapporteur de thèse), ZULUAGA Maria A. (rapporteure de thèse), KACHENOURA Nadjia (examinatrice), MERIAUDEAU Fabrice (examinateur), CLARYSSE Patrick (examinateur), VARRAY François (directeur de thèse), MAGNIN Isabelle (invitée)